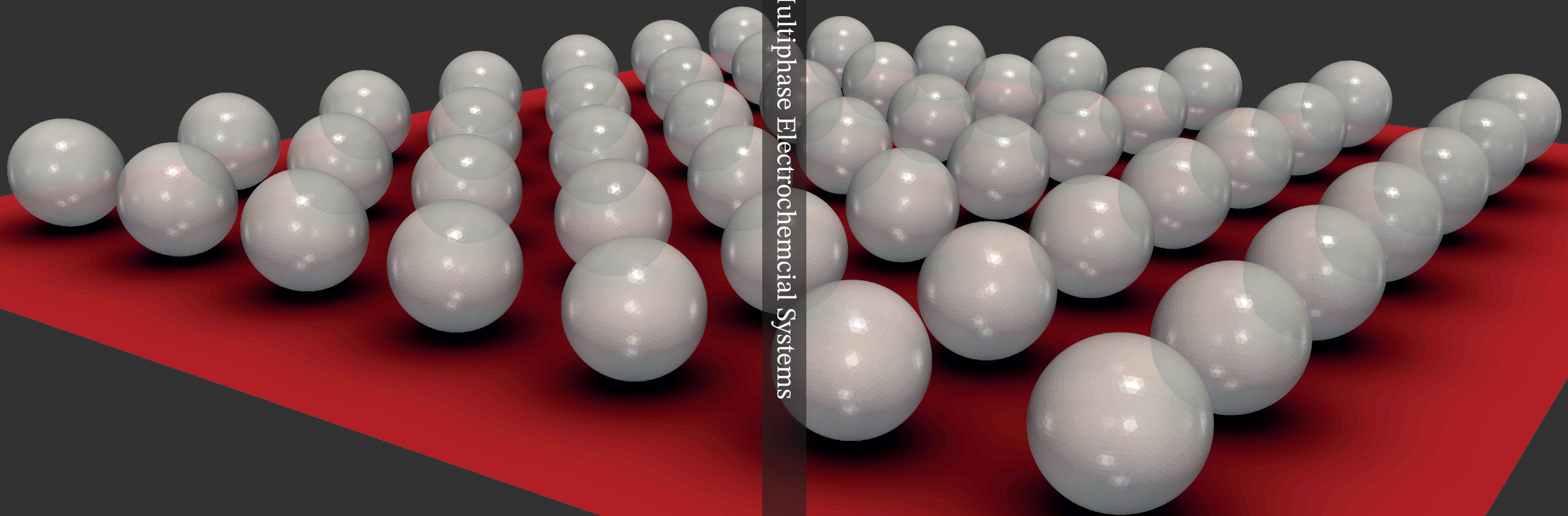


MASS TRANSPORT

in

MULTIPHASE ELECTROCHEMICAL SYSTEMS



Mass Transport in Multiphase Electrochemical Systems

Farzan Sepahi

Farzan Sepahi

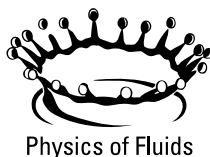
# Mass Transport in Multiphase Electrochemical Systems

Farzan Sepahi

**Graduation Committee:**

Prof. Dr. J. L. Herek (Dean)	University of Twente
Prof. Dr. rer. nat. D. Lohse (Promotor)	University of Twente
Prof. Dr. R. Verzicco (Co-promotor)	University of Twente & Tor Vergata
Dr. D. J. Krug (Co-promotor)	University of Twente
Dr. Ir. S. J. A. de Beer	University of Twente
Prof. Dr. R. M. van der Meer	University of Twente
Prof. Dr. G. Mul	University of Twente
Prof. Dr. Ir. J. T. Padding	Delft University of Technology
Prof. Dr. Ir. A. W. Vreman	Eindhoven University of Technology

**UNIVERSITY  
OF TWENTE.**



The work in this thesis was carried out at the Physics of Fluids group of the Faculty of Science and Technology of the University of Twente. This work was supported by the Netherlands Center for Multiscale Catalytic Energy Conversion (MCEC), an NWO Gravitation programme funded by the Ministry of Education, Culture and Science of the government of the Netherlands.

Dutch title:

*Massatransport in multiphase elektrochemische systemen*

Publisher:

Farzan Sepahi, Physics of Fluids, University of Twente,  
P.O. Box 217, 7500 AE Enschede, The Netherlands

Copyright © Farzan Sepahi, Enschede, The Netherlands 2023.

All rights reserved. No part of this work may be reproduced or transmitted for commercial purposes, in any form or by any means, electronic or mechanical, including photocopying and recording, or by any information storage or retrieval system, except as expressly permitted by the publisher.

ISBN (Digital): 978-90-365-5688-7

DOI: 10.3990/1.9789036556897

# MASS TRANSPORT IN MULTIPHASE ELECTROCHEMICAL SYSTEMS

DISSERTATION

to obtain  
the degree of doctor at the University of Twente,  
on the authority of the rector magnificus,  
prof. dr. ir. A. Veldkamp,  
on account of the decision of the Doctorate Board,  
to be publicly defended  
on Wednesday, July 5<sup>th</sup>, 2023 at 12:45

by

Farzan Sepahi  
Born on May 16<sup>th</sup>, 1990  
in Fasa, Iran

This dissertation has been approved by the promotor:

Prof. Dr. rer. nat. Detlef Lohse

and co-promotors:

Prof. Dr. Roberto Verzicco  
Assoc. Prof. Dr. Dominik Krug

*To my parents*



# Contents

<b>Introduction</b>	<b>1</b>
<b>1 The effect of buoyancy driven convection on the growth and dissolution of bubbles on electrodes</b>	<b>11</b>
1.1 Introduction . . . . .	13
1.2 Experimental and numerical details . . . . .	14
1.3 Results and discussion . . . . .	17
1.4 Conclusion . . . . .	28
1.5 Appendix . . . . .	29
<b>2 Mass transport at gas-evolving electrodes</b>	<b>35</b>
2.1 Introduction . . . . .	37
2.2 Configuration and numerical methods . . . . .	39
2.3 Bubble dynamics and mass transfer at the electrode . . . . .	48
2.4 Mass transfer to the bubble . . . . .	67
2.5 Gas-evolution efficiency . . . . .	72
2.6 Discussion and conclusions . . . . .	73
2.7 Appendix . . . . .	77
<b>3 Diffusive and convective dissolution of carbon dioxide in a vertical cylindrical cell</b>	<b>81</b>
3.1 Introduction . . . . .	83
3.2 Experimental procedure . . . . .	84
3.3 Experimental observations . . . . .	87
3.4 Intensity and concentration profiles . . . . .	90
3.5 Front propagation dynamics . . . . .	94
3.6 Numerical model . . . . .	99
3.7 Conclusions . . . . .	109

3.8 Appendix . . . . .	111
<b>Conclusions</b>	<b>119</b>
<b>Summary</b>	<b>143</b>
<b>Samenvatting</b>	<b>145</b>
<b>Acknowledgments</b>	<b>147</b>
<b>About the author</b>	<b>153</b>

# Introduction

As the world faces unprecedented challenges related to climate change and energy sustainability, there is an increasing urgency to shift towards cleaner and more sustainable energy sources. One promising pathway to achieve this transition is through hydrogen production and carbon capture technologies, which offer the potential to decarbonize various sectors of the economy, reduce greenhouse gas emissions, and mitigate the adverse impacts of climate change.

Hydrogen, as a versatile and energy-dense fuel, has gained significant attention as a key element in the transition to a low-carbon future. It can be produced from a variety of sources, including renewable energy sources such as wind, solar, and hydroelectric power, as well as from fossil fuels with Carbon Capture and Storage (CCS) technologies. Hydrogen can be used as a clean fuel for transportation, power generation, and industrial processes, and can also be used as a valuable chemical feedstock in various industries [1–6].

## Water electrolysis

Water electrolysis has recently gained significant attention as a reliable method for hydrogen production. It offers several advantages for hydrogen production, including its ability to utilize the power output of renewable energy resources such as solar or wind power (figure 1), rendering it a potential tool for energy storage and grid balancing [7–10]. Furthermore, water as an abundantly available resource makes water electrolysis a sustainable and scalable method for hydrogen production. Yet, there are still challenges to be addressed. This mostly pertains to the efficiency of the electrolysis process, and the development of suitable catalysts and materials for electrodes.

Mass transfer in water electrolysis is also a key factor that massively influences the efficiency of the system. During water electrolysis, mass transfer refers to the

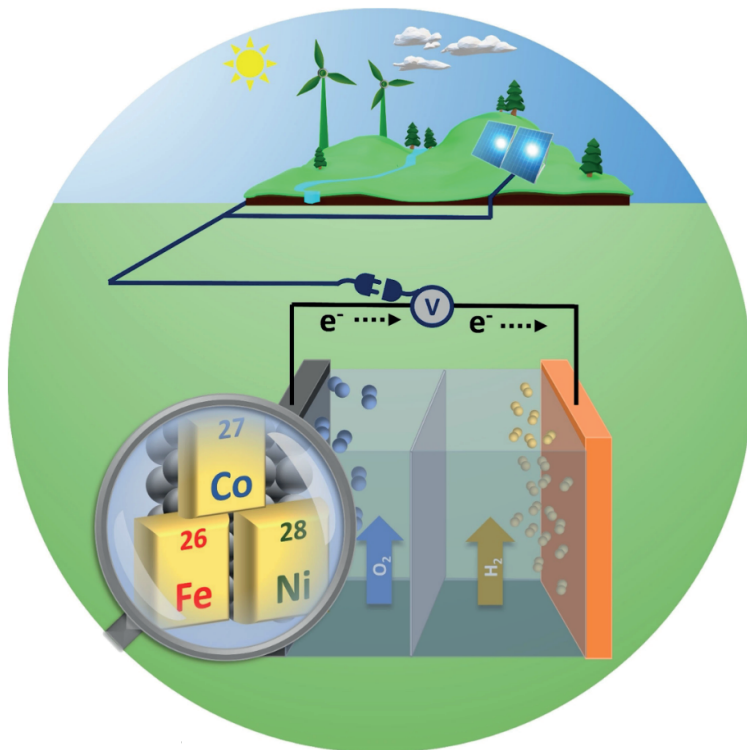


Figure 1: 'Green' hydrogen production through water electrolysis by harnessing the energy of renewable power sources. Image taken from [10].

movement of the reactants (water molecules and electrolyte) and products (hydrogen and oxygen gases) between the electrodes and at the electrodes interface. The rate of mass transfer in these systems controls the the reaction rate on the electrodes and ultimately the efficiency of the electrolyzer. Hence, it is crucial to maximize the mass transfer rate at which the reactants are supplied to the electrode and products are transported away, to enhance the efficiency and scalability. Efficient mass transfer can be achieved by utilization of various approaches such as optimizing the design and configuration of the electrolyzer (e.g, size and spacing of electrodes) the flow rate of electrolyte and operating conditions including temperature and pressure. Moreover, employing state-of-the-art methods to improve the surface properties of electrodes [11, 12] along with utilization of catalysts [13–15] can further improve the efficiency by increasing the active sites for the electrochemical reaction

to occur. Here, we briefly explain the electrochemistry involved in water electrolysis followed by mass transfer and hydrodynamics of the system which are strongly coupled.

## Electrochemistry

Transport of ions in the electrolyte solution occurs as a result of migration, diffusion and convection. These processes collectively determine the net flux ( $\dot{\mathbf{N}}_k$ ) of the species ( $k$ ) in the system given by Nernst-Planck equation as

$$\dot{\mathbf{N}}_k = -z_k \frac{F}{\mathcal{R}T} D_k C_k \nabla \phi - D_k \nabla C_k + C_k \mathbf{u}, \quad (1)$$

Where  $\phi$ ,  $\mathbf{u}$ ,  $C$  and  $T$  are the electric potential, velocity, concentration and temperature fields respectively,  $D$  is mass diffusivity,  $F$  is Faraday constant,  $z$  is ionic valence of the charged species, and  $\mathcal{R}$  is the gas universal constant. Migration refers to the transport of ions resulting from an electric field, represented by the first term on the right-hand side of Equation (1). Diffusion, on the other hand, describes the movement of species from regions of higher concentration to lower concentration, represented by the second term on the right-hand side of Equation (1). Lastly, convection refers to the movement of substances caused by fluid flow, which is represented by the last term of Equation (1). The current density ( $\mathbf{i}$ ) in the electrolyte solution is caused by the motion of the charged species and can be expressed as [16]

$$\mathbf{i} = F \sum_k z_k \dot{\mathbf{N}}_k, \quad (2)$$

which together with (1) yields

$$\mathbf{i} = -F^2 \nabla \phi \sum_k z_k^2 \frac{D_k}{\mathcal{R}T} C_k - F \sum_k z_k D_k \nabla C_k + F \mathbf{u} \sum_k z_k C_k. \quad (3)$$

Charge separation is not possible in electrolytic solutions and hence electroneutrality condition

$$\sum_k z_k C_k = 0, \quad (4)$$

holds throughout [17], leading the last term in (3) to be zero. Charge conservation always requires that

$$\nabla \cdot \mathbf{i} = 0, \quad (5)$$

which together with (3) gives an expression for electric potential,  $\phi$ , as [16, 18]

$$\nabla \cdot (\kappa \nabla \phi) + F \sum_k z_k \nabla \cdot (D_k \nabla C_k) = 0, \quad \text{with } \kappa = F^2 \sum_k \frac{z_k^2 D_k}{\mathcal{R}T} C_k, \quad (6)$$

where  $\kappa$  is the electric conductivity of the electrolyte solution and is dependant on local temperature and concentrations. Based on the electroneutrality condition (4) and in case of insignificant concentration gradients in the solution or equal diffusivity of the ions, the last term of (6) can be neglected [16].

## Mass transfer and hydrodynamics

The electrochemistry of the system (6) is coupled to the mass transfer problem and hydrodynamics. Applying mass conservation to Nernst-Planck equation (1),

$$\frac{\partial C_k}{\partial t} = -\nabla \cdot \dot{\mathbf{N}}_k, \quad (7)$$

yields the equation of transport for species as follows

$$\frac{\partial C_k}{\partial t} = z_k \frac{F}{\mathcal{R}T} \nabla \cdot (D_k C_k \nabla \phi) + \nabla \cdot (D_k \nabla C_k) - \mathbf{u} \cdot \nabla C_k, \quad (8)$$

where the velocity field  $\mathbf{u}$  is determined through the incompressible Navier-Stokes equations for a Newtonian fluid,

$$\frac{\partial \mathbf{u}}{\partial t} + \mathbf{u} \cdot \nabla \mathbf{u} = -\nabla P + \nu \nabla^2 \mathbf{u} + \mathbf{f}, \quad (9)$$

along with continuity equation

$$\nabla \cdot \mathbf{u} = 0. \quad (10)$$

Here,  $P$  and  $\nu$  are kinematic pressure and viscosity, and  $\mathbf{f}$  is the body force due to buoyancy caused by slight density gradients as a result of concentration variation in the electrolyte. Within the Buossinesq approximation it is then given by

$$\mathbf{f} = \sum_{\forall k} \beta_k (C_k - C_{k,0}) \mathbf{g}, \quad (11)$$

where  $\beta$  is solutal volume expansion coefficient,  $C_{k,0}$  is the initial concentration of the species and  $\mathbf{g}$  is gravitational acceleration.

## Bubble evolution

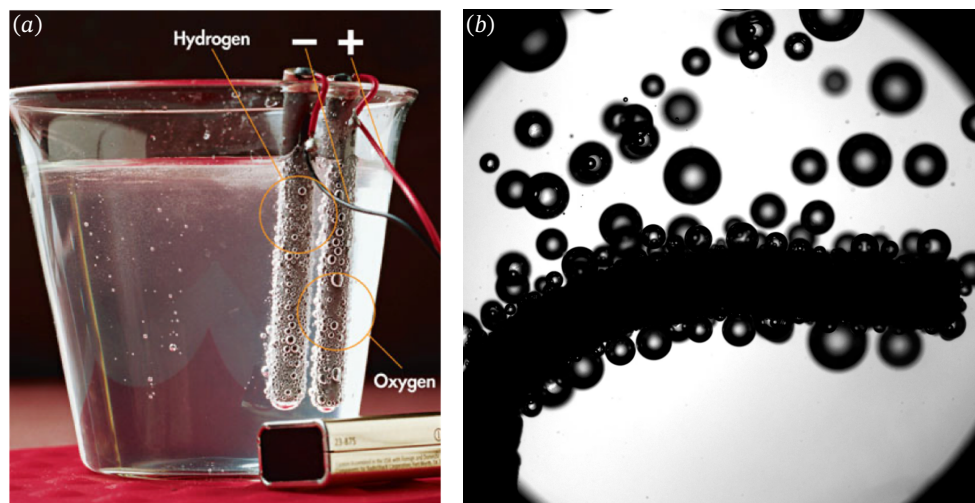


Figure 2: Bubble evolution during water electrolysis with wire electrodes. (a) Image credit to [www.tudelft.nl](http://www.tudelft.nl) (b) Image by Alexandr Bashkatov.

Gas-evolution on the electrodes in water electrolyzers adds to the complexities of different processes as these systems are prone to formation of gas bubbles (figure 2). Bubbles play a significant role in altering the system efficiency. First they reduce the effective surface area of the electrode by reducing the actual contact area between the electrode and electrolyte. This can lead to lower efficiency in the electrolysis process due to the reduced electroactive area which limits the reaction rate. In the other hand, bubble can also impact the cell overpotential, which is the extra energy required to drive the electrolysis reaction beyond its thermodynamic potential. The formation of gas bubbles increases the resistance to current flow (due to the nearly zero electric conductivity of the gas), leading to higher overpotential. This means that more energy may be required to continue the electrolysis which significantly decreases the overall efficiency of the system.

Bubble evolution comprises several processes in sequence; *nucleation*, *growth* and *detachment*. *Nucleation* happens as result of accumulation of the dissolved gas in the electrode boundary layer and when a certain number of the gas molecules cluster in nucleation spots such as crevices and cracks where the energy barrier is the lowest (figure 3(a)). Once a stable nuclei is formed, diffusion of the dissolved gas to the interface and its desorption to the gas phase will lead to bubble formation and its further growth (figure 3(b)). Balancing the rate of the change of the molar amount of gas inside the bubble with the diffusive flux of gas across the interface (determined

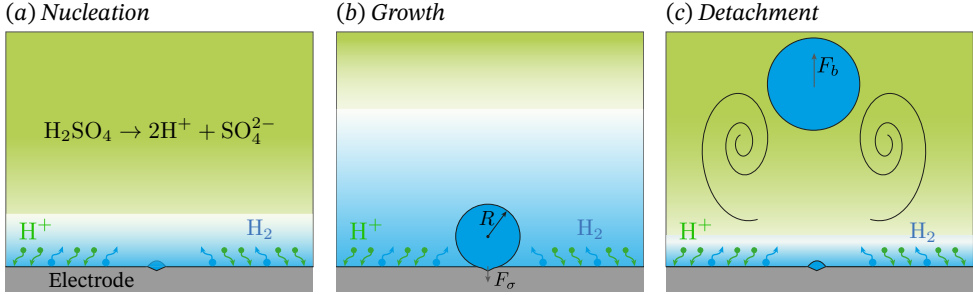


Figure 3: Different stages of bubble evolution on a gas-evolving electrode (cathode) with binary sulphuric acid solution as electrolyte. Hydrogen ion is reduced and hydrogen gas is produced in hydrogen evolution reaction on the electrode. Blue and green colors indicate the concentration of hydrogen and sulphuric acid in the electrolyte. As a result of diffusion, hydrogen concentration reduces from the electrode (dark blue) to the bulk electrolyte (light blue) and acid concentration increases from the electrode (light green) to the bulk electrolyte (dark green) (a) Heterogeneous bubble nucleation in a crevice on the electrode surface. (b) Bubble growth as a result of hydrogen diffusion to the gas-liquid interface and its desorption to the gas phase. During this stage bubble is attached to the surface with interfacial tension force,  $F_\sigma$ , and in the meantime electrode boundary layers diffusively grow into the bulk electrolyte. (c) Bubble detachment as a result of buoyancy force,  $F_b$ , dominating over surface tension. Generated convective flow, caused by bubble ascent, advects fresh electrolyte to the electrode and enhance the mass transport (lower thickness of electrode boundary layers).

by Fick's law) as

$$\dot{N}_b = \frac{\mathcal{R}T_0}{P_0} 4\pi R^2 \frac{dR}{dt} = \int_{\partial V} D_g \nabla C_g \cdot \hat{\mathbf{n}}_b dA, \quad (12)$$

yields the bubble growth rate

$$\frac{dR}{dt} = \frac{\mathcal{R}T_0}{P_0} \frac{1}{4\pi R^2} \int_{\partial V} D_g \nabla C_g \cdot \hat{\mathbf{n}}_b dA, \quad (13)$$

where  $T_0$  and  $P_0$  are ambient temperature and pressure respectively,  $R$  is the instantaneous radius of the bubble and  $\hat{\mathbf{n}}_b$  is the unit normal vector at the surface  $\partial V$  of the bubble. During this period the bubble is adhered to the electrode by surface tension forces and boundary layers on the electrode continuously grow (figure 3(b)). After growth of the bubble to a certain size (so-called Fritz radius) beyond which the forces assisting the detachment (buoyancy, pressure and inertial) predominates over the surface tension and drag forces [19–21], it departs from the electrode surface and rises in the solution (figure 3(c)).

## Governing mass transfer mechanisms

Understanding the mass transfer processes at gas-evolving electrodes has become increasingly important as it helps optimize the cell design and tune the operating condition to prevent undesirable effects of bubbles evolution and enhance the performance of the system. Convection due to the fluid flow is one of the governing mechanisms controlling the mass transfer in water electrolysis. Although bubbles will negatively impact the system performance by blocking the active area of the electrode, they also favorably influence the mass transfer at the electrode by inducing convective flow in the solution. During the bubble growth, expanding boundary of the bubble pushes the surrounding liquid away and induces micro-convection in its proximity. It also induces a large-scale flow pattern (macro-convection) after the departure from the electrode and rising in the electrolyte solution. The convective flows induced by bubble evolution enhance the solution mixing, and therefore mass transport, close to the electrode which ultimately favors the reaction rate (figure 3(c)). The macro-convection of rising bubbles in the electrolyte is also referred as two-phase buoyancy-driven convection and is generated owing to the inhomogeneous distribution of bubble in the gas-in-liquid dispersion.

In addition to two-phase free convection, single-phase free convection can also arise due to the density gradients in the electrolyte, which originates from temperature and concentration variation of species in the electrolyte owing to the ongoing reaction. Single-phase natural convection in electrolyzers had commonly been disregarded until evidenced by recent works in the literature [22–28]. Although single-phase natural convection has been identified in the electrochemical systems without the bubble formation and its impact on reaction kinetics on the electrode has been investigated, the role that it can indirectly have on mass transfer processes by changing the bubble dynamics at gas-evolving electrodes is unclear. In fact, single-phase convection can enhance the efficiency of the system by promoting the bubbles removal in addition to their positive effect on mass transport at the electrode.

Although, single-phase convection can control the rate of mass transfer under certain conditions, especially at low values of current density where bubble growth is slow and they adhere to the electrode surface for a long time, at high current densities the two-phase buoyancy-driven convection is very likely to prevail. This is corroborated by very high frequency of bubble generation and their detachment from the electrode surface which cause a strong flow in the electrolyte. Such effects, although known for several decades, have not been fully investigated and quantified yet. In addition, the question of "which mechanism primarily control the transport of chemical reagents and reaction products at the electrode" has not been clearly

answered and the findings in this regards in the literature seem contradictory.

Given the preceding discussion, it is our aim in this thesis to unravel the intricacies pertaining to the mass transfer at gas-evolving electrodes in which bubbles form frequently. Hence, we employ high-fidelity direct numerical simulations to mimic the most relevant physics governing the fluid flow and mass transfer in water electrolysis. Our findings offer broader perspective over different mechanisms concurrently playing a role in transport phenomena and hence help devise systems with higher efficiencies addressing the mass transfer limitations.

## Carbon capture and storage

Carbon capture involves the capture, utilization, or storage of carbon dioxide ( $\text{CO}_2$ ) emissions from industrial processes, power plants, and other sources, to prevent them from being released into the atmosphere. This technology can help to significantly reduce  $\text{CO}_2$  emissions, which are one of the primary contributors to climate change, and has the potential to play a critical role in the energy transition [29–35]. In large scales, storage of  $\text{CO}_2$  in geological formations such as deep saline aquifers is projected to be a promising technology to reduce the on-earth emissions (figure 4). However, a secure long-term dissolution of  $\text{CO}_2$  in the ambient brine has remained a major challenge compromising the reliability of the technology. Hence, a thorough understanding of the dissolution mechanism of  $\text{CO}_2$  is essential for designing secure carbon storage systems which enables the selection of suitable storage sites with sufficient capacity.

Once the carbon dioxide starts to dissolve into the water layer, a  $\text{CO}_2$ -rich water layer forms at the interface, which is denser in comparison to pure water. While initially stable, the continued dissolution of  $\text{CO}_2$  into the water layer results in the  $\text{CO}_2$ -rich fluid layer becoming gravitationally unstable, leading to the onset of buoyancy driven convection and the formation of a buoyant plume (figure 4(B)), which greatly enhances the mass transfer of  $\text{CO}_2$  in the water layer [36,37]. In literature, studies investigating the dissolution and density driven convection in the  $\text{CO}_2$ -water system have reported between two and four distinct transport regimes [38–40]. These regimes are vaguely defined by their assumed dominant driving mechanism and thus referred to as, for example, "purely diffusive", "early convective", or "late convective" [38]. Moreover, in the regimes where convection is contributing to the mass transport, apparent diffusive behaviour is observed, albeit with a much higher effective diffusion coefficient. However, little explanation has been given as to what drives the different observed regimes, the transitions between the regimes and why the system still appears to behave in a diffusive manner.

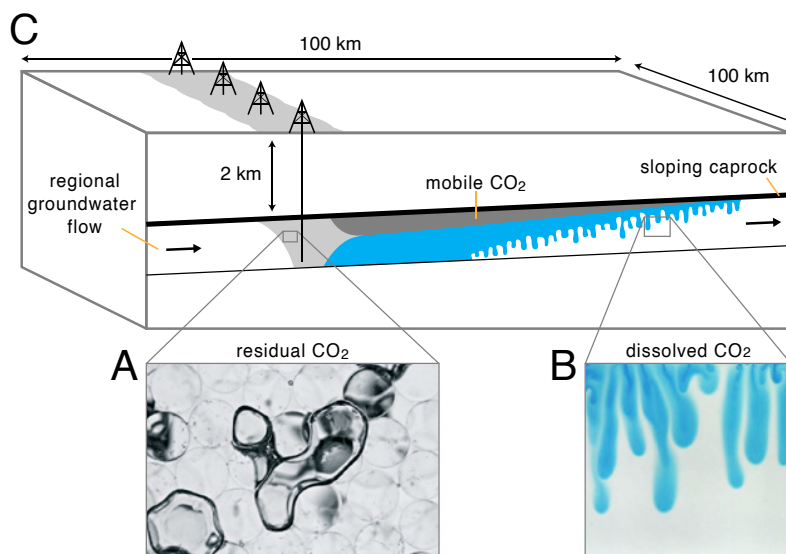


Figure 4: Schematic representation of CO<sub>2</sub> storage with capillary trapping in the pore space (A) and dissolution trapping (B) where the dense CO<sub>2</sub>-saturated brine sinks through the plume emissions. Image taken from [10].

Therefore, it is our aim in this thesis to investigate the mass transport mechanisms after the dissolution of CO<sub>2</sub> into a liquid barrier under well-defined and controlled condition to fully understand the governing mechanisms driving the dissolution of CO<sub>2</sub> into the liquids.

## A guide through this thesis

The thesis is structured as follows. In **chapter 1** we aim to investigate the effect of single-phase natural convection, caused by concentration gradients of the electrolyte and hydrogen gas, on the growth and dissolution of bubbles on electrodes. By comparing our results to in-situ experimental measurements, we untangle the effect of natural convection from pure diffusion and highlight its importance in the bubble growth and dissolution dynamics. Additionally we vary the bubble spacing and their arrangement in a clustered network on the electrode to investigate their impact on the induced instabilities in the electrolyte solution as a result of density gradients, the emerged convective pattern and the subsequent bubble dynamics.

In **chapter 2**, disregarding the single-phase natural convection we focus on bubble-induced convection on mass transfer processes. This includes the flow caused by

0

bubble growth (micro-convection) and more importantly by bubble motion after their break-off from the electrode surface (macro-convection). Taking advantage of numerical simulations, we independently vary our parameter space, which includes current density, bubble size and bubble spacing. This allows the quantification of mass transfer for the electrolyte as well as hydrogen gas at the electrode interface, and therefore identification of the rate-controlling mechanism of mass transfer. Subsequently, we aim to quantify the hydrogen transport to the bubble based on the simulations input parameters and find its connection to the hydrogen transport at the electrode. This further allows for establishment of a unique expression for gas-evolution efficiency which is key in determining the bubble dynamics and, therefore, the overall mass transport rate at gas-evolving electrodes.

In **chapter 3**, we use direct numerical simulations to unravel the peculiar dynamics of  $\text{CO}_2$  downward dissolution in a cylindrical water barrier observed from the experiments. The diffusive and convective dissolution of  $\text{CO}_2$  is first visualised in the experiments from which a diffusion-controlled dynamic of the front is observed even after transition to the convection. By replicating the results through the numerical simulations and performing a detailed analysis on the front dynamics (which cannot be achieved experimentally), the underlying physics governing the relevant dynamics of the  $\text{CO}_2$  front is elucidated. Our results offer insight into the capacity of the carbon storage systems.

# 1

## The effect of buoyancy driven convection on the growth and dissolution of bubbles on electrodes<sup>o</sup>

*Enhancing the efficiency of water electrolysis, which can be severely impacted by the nucleation and growth of bubbles, is key in the energy transition. In this combined experimental and numerical study, in-situ bubble evolution and dissolution processes are imaged and compared to numerical simulations employing the immersed boundary method. We find that it is crucial to include solutal driven natural convection in order to represent the experimentally observed bubble behaviour even though such effects have commonly been neglected in modelling efforts so far. We reveal how the convective patterns depend on current densities and bubble spacings, leading to distinctively different bubble growth and shrinkage dynamics. Bubbles are seen to promote the convective instability if their spacing is large ( $\geq 4\text{mm}$  for the present conditions), whereas the onset of convection is delayed if the inter-bubble distance is smaller. Our approach and our results can help devise efficient mass transfer solutions for gas evolving electrodes.*

---

<sup>o</sup>Published as: **Farzan Sepahi**, Nakul Pande, Kai Leong Chong, Guido Mul, Roberto Verzicco, Detlef Lohse, Bastian T. Mei, Dominik Krug, *The effect of buoyancy driven convection on the growth and dissolution of bubbles on electrodes*, *Electrochimica Acta* **403**, 139616 (2022).



## 1.1 Introduction

The process of bubble formation is of significant technological relevance [41]. This also holds in the context of industrial processes relevant for the energy transition such as water electrolysis or electrochemical CO<sub>2</sub> reduction [42–44]. Production of ‘green’ hydrogen from water splitting is envisioned to be a major contributor in the future energy mix [45]. However, current technologies suffer from limited cell efficiencies or high costs [45,46], rendering large scale operation uneconomical in many cases. It is well established that the presence of bubbles critically affects electrolyser efficiency [43,46,47], e.g. by reducing the active electrode area [48,49] or by raising the cell resistance [50,51]. This has sparked significant interest in concepts to manage the bubble nucleation and growth and the gas flow on gas-evolving electrodes [52–56]. For such approaches, it is crucial to understand the mass transport phenomena, as they determine the bubble nucleation, growth and detachment rates [20,57,58].

With the exception of recent work on local Marangoni convection [59–62], related studies are mostly performed assuming a stagnant electrolyte and focus on diffusive transport [52,55,57,58]. At the same time, the relevance of global convective instabilities in electrochemical systems is now well documented. These can originate from electric fields [63,64], but predominantly also from buoyancy forces resulting from the density gradients caused by electrode reactions and ion transport [25,28,65,66]. In particular, the simulations of Ngamchuea et al. [25] showed that such solute driven natural convection can significantly enhance mass transport during the oxidation of hexacyanoferrate, while later studies also accounted for thermal forcing [26,27]. The presence of natural convection in water electrolysis has also been demonstrated experimentally indirectly through pH-mapping [65] and directly through velocity measurements [66].

The presence of convection over a wide parameter range strongly suggests that this effect also plays a role in the bubble evolution. This is corroborated by the fact that e.g. van der Linde et al. [58] had to scale the actual current densities down by a factor of up to 10 in order to match experimentally measured electrolytic bubble growth rates, as models assuming pure diffusion strongly overpredicted the bubble growth. Given such inconsistencies, it is our goal here to systematically explore the role of convective effects on the bubble evolution in electrochemical water splitting. Moreover, this work provides insight into how the presence of bubbles in turn affects the hydrodynamic instability. Our approach combines experiments with direct numerical simulations (DNS) employing the immersed boundary method. Details on both will be provided in the next section before we will present and discuss the

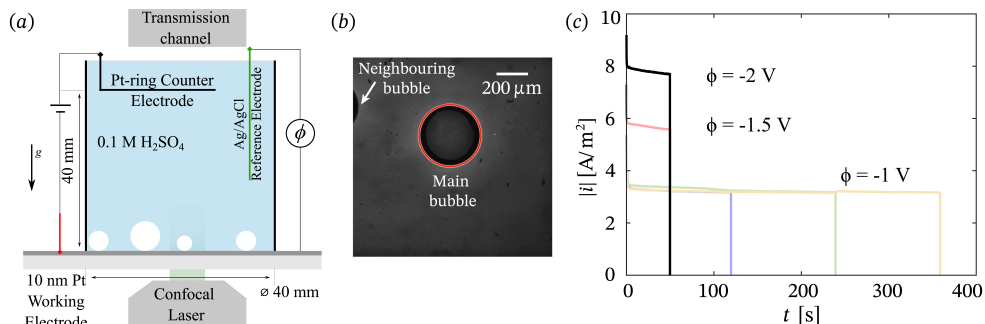


Figure 1.1: (a) Schematic of the experimental setup. (b) Sample transmission image with the red line indicating the extracted bubble size. (c) Measured current densities,  $i$ , for the different pulses at varying constant potentials ( $\phi = -1$  V,  $-1.5$  V,  $-2$  V) and pulse times  $\tau_p$  (evident from the drop to 0 in  $i$ ).

results and summarize our findings in the conclusion.

## 1.2 Experimental and numerical details

### 1.2.1 Experimental setup

The electrochemical cell (see figure 1.1(a)) is made of Teflon and houses a typical undivided 3-electrode configuration: A transparent platinum (Pt) working electrode, a Pt mesh counter electrode shaped as a ring and placed at a distance of  $\approx 4$  cm from the working electrode, and a Ag/AgCl (in 3M NaCl; BasiR) reference electrode. The setup was mounted on the stage of a Nikon A1R confocal microscope and illuminated from below with a 532 nm laser. Partial transparency of the working electrode was achieved by evaporating 10 nm Pt on glass, with a 3 nm Chromium underlayer (10 nm Pt roughly  $\approx 30\%$  transmittance [67]). In this way, bubbles appeared as shadows in the transmission images as shown in figure 1.1(b). The cell was operated using a VersaStat (PAR) potentiostat with a sampling rate of 100 Hz. Sulfuric acid (0.1 M H<sub>2</sub>SO<sub>4</sub>, Sigma Aldrich) was used as electrolyte.

Simultaneous electrochemical and optical measurements were performed with the following experimental protocol. First, a negative (reduction) potential pulse was applied for a short time (60 s – 360 s depending on the experiment). The pulse length and intensity was chosen such that a limited number of bubbles was nucleated and started to grow on the electrode while avoiding disturbances by bubble detachment. The current density was recorded (see figure 1.1(c)) and the micro-

scope stage was slowly moved (about the electrode center) until a growing bubble was encountered in the field of view of the camera ( $1.28 \times 1.28 \text{ mm}^2$ ). Hence, the bubble measurements typically only start some time after the start of the current pulse. We ensured that the measured bubble was the first bubble growing at that location to avoid history effects due to depletion of the gas concentration and bubble detachment [68,69]. The microscope imaging was continued for approximately 10 min after the potential pulse to capture the evolution of the bubble size. The open-circuit potential of the cell was measured simultaneously. Fresh electrolyte was used for each individual experiment. Note that the bubbles are not isolated as can be seen from figure 1.1(b) (here with center-to-center distance  $\approx 0.6 \text{ mm}$ ) and that we only track the size of the ‘main’ bubble in the field of view.

## 1.2.2 Simulations

The electrolyte consists of sulfuric acid which is assumed to fully dissociate in water to hydrogen and sulfate ions as



which greatly simplifies the numerical modelling. Additionally, it is assumed that proton reduction to hydrogen is the only cathodic reaction occurring, i.e.



Note that given the low current densities employed here, we have neglected the bulk water dissociation reaction for simplicity.

To obtain the fluid velocity  $\mathbf{u}$  field, we solve the Navier-Stokes equations

$$\frac{\partial \mathbf{u}}{\partial t} + (\mathbf{u} \cdot \nabla) \mathbf{u} = -\nabla p + \nu \nabla^2 \mathbf{u} + \mathbf{f}, \quad (1.3)$$

along with continuity,

$$\nabla \cdot \mathbf{u} = 0. \quad (1.4)$$

Here,  $p$  and  $\nu$  respectively denote the kinematic pressure and the kinematic viscosity, and  $\mathbf{f}$  is the body force due to buoyancy. Assuming electroneutrality in the bulk of the solution [17] allows us to eliminate the migration terms [70] (see Appendix 1.5.1 for derivation), such that the transport of all species  $C_j$  is governed by an effective advection diffusion equation

$$\frac{\partial C_j}{\partial t} + (\mathbf{u} \cdot \nabla) C_j = D_j \nabla^2 C_j. \quad (1.5)$$

where the subscript  $j = (s, \text{H}_2)$  refers to  $\text{H}_2\text{SO}_4$  and  $\text{H}_2$ , respectively. The diffusivity of  $\text{H}_2\text{SO}_4$  is related to the diffusivity of its ions and is calculated as [70]:

$$D_s = \frac{D_1 D_2 (z_1 - z_2)}{z_1 D_1 - z_2 D_2}, \quad (1.6)$$

where  $z_k$  is the ionic valence and subscript  $k = (1, 2)$  refers to  $\text{H}^+$  and  $\text{SO}_4^{2-}$  ions, respectively and the diffusion constants for the hydrogen and ionic species are given in table 1.1 in Appendix 1.5.2.

We employ no slip at the electrode surface and the set of boundary conditions for the scalar fields is (see Appendix 1.5.1 for the derivation of (1.7))

$$\frac{i}{(n_e/s_1)F} = 2D_1 \left(1 - \frac{z_1}{z_2}\right) \left(\frac{\partial C_s}{\partial z}\right)_{z=0}, \quad (1.7a)$$

$$\frac{i}{(n_e/s_{\text{H}_2})F} = D_{\text{H}_2} \left(\frac{\partial C_{\text{H}_2}}{\partial z}\right)_{z=0}, \quad (1.7b)$$

where  $s_j$  and  $n_e$  refer to stoichiometric coefficients and the number of transferred electrons in the cathodic reaction (1.2), respectively, and  $F = 96\,485 \text{ C mol}^{-1}$  is the Faraday constant.

Thermal effects are expected to be small in the current system [71] and we therefore only consider solutal changes to the density field. Within the Boussinesq approximation of small density changes relative to the initial electrolyte density, the buoyancy force in (1.3) is then given by

$$\mathbf{f} = \sum_{\forall j} \beta_j (C_j - C_{j,0}) \mathbf{g}, \quad (1.8)$$

where  $\beta_j$  is the (isothermal and isobaric) volume expansion coefficient of species  $j$ ,  $C_{j,0}$  denotes the initial concentration, and  $\mathbf{g}$  is the gravitational acceleration.

The shape of the bubbles is modelled using an immersed boundary method (IBM), for which specifics are provided in the Appendix 1.5.2 along with further details on the numerical method. By evaluating the flux  $D_{\text{H}_2} \int_{\Sigma} \nabla C_{\text{H}_2} \cdot \hat{\mathbf{n}} d\Sigma$  of  $\text{H}_2$  over the bubble surface  $\Sigma$  with normal  $\hat{\mathbf{n}}$  and using the ideal gas law, we find for the radius  $R$  of the (spherical) bubble

$$\frac{dR}{dt} = \frac{\mathcal{R}T_{\infty}}{P_0} \frac{1}{4\pi R^2} \int_{\Sigma} D_{\text{H}_2} \nabla C_{\text{H}_2} \cdot \hat{\mathbf{n}} d\Sigma, \quad (1.9)$$

with  $\mathcal{R}$ ,  $P_0$ , and  $T_{\infty}$  denoting the universal gas constant, ambient pressure, and temperature, respectively. Further, the Laplace pressure is neglected since it is insignificant ( $< 1440 \text{ Pa}$  while the ambient pressure  $p_0 = 10^5 \text{ Pa}$ ) for the relatively large bubble radii (simulations commence from  $R_0 = 0.1 \text{ mm}$ ) considered here.

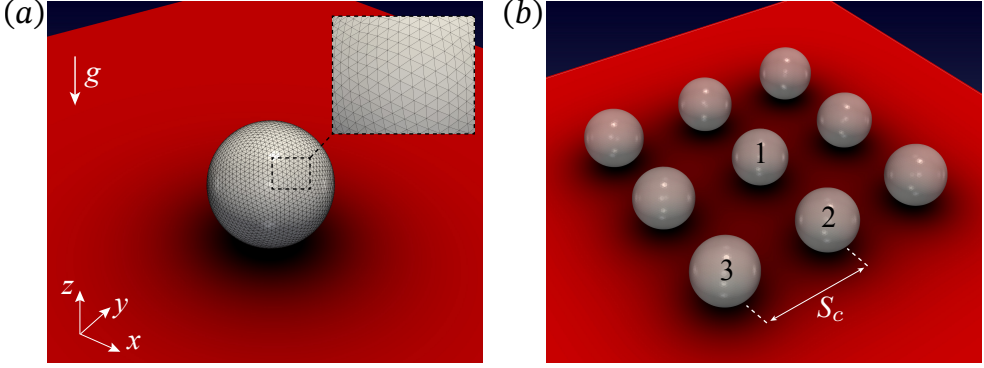


Figure 1.2: Rendering of (a) the basic simulation setup with a single bubble in the center of the domain and (b) a  $3 \times 3$  bubble cluster with spacing  $S_c$ .

A fixed saturation concentration  $C_{\text{H}_2, \text{sat}}$  is enforced for  $\text{H}_2$  at the bubble boundary, while a no flux condition is used for all other species. We further employ a no slip condition at the bubble surface to mimic a fully contaminated bubble [72].

We refrain from modelling the intricacies of the bubble nucleation [73,74], as this is beyond the scope of the present study. Instead, we initiate bubbles 28 s after the start of the potential pulse with an initial radius  $R_0 = 0.1$  mm, which is in accordance with the experiments (see section Experimental setup). Bubbles remain attached tangentially to the electrode surface (contact angle  $0^\circ$ ) throughout the simulations. This choice well approximates experimental results [49,75] and conforms with earlier modelling approaches [76,77]. In the basic configuration (see figure 1.2(a)), we consider a single bubble in the center of the domain and periodic boundary conditions to represent an idealized, regular bubble array with spacing  $S$  determined by the lateral dimension of the computational box. Additionally, we perform simulations in which the single bubble is replaced by a  $3 \times 3$  array of bubbles with interspacing  $S_c$  as shown in figure 1.2(b) in order to investigate collective effects.

### 1.3 Results and discussion

The inset of figure 1.3(a) shows the temporal evolution of the bubble radius  $R(t)$  for the different potential pulses displayed in figure 1.1(c) (with correspondences indicated by matching line colors). The same data is re-plotted in the main panel of figure 1.3(a). Shifting the time axis by the respective pulse duration  $\tau_p$  and nor-

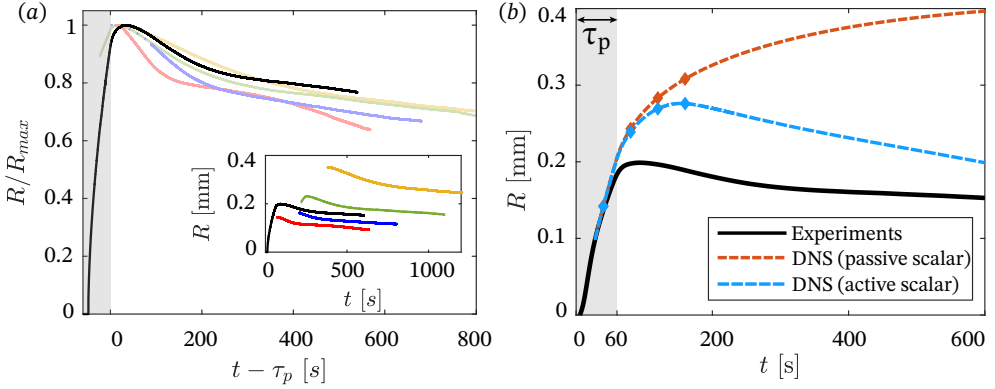


Figure 1.3: (a) Bubble radius as function of time as obtained from the experiments. The line colour indicates different shapes pulse lengths with the same colour code as in figure 1.1(c). (b) Comparison of experimentally measured bubble radius and those obtained from numerical simulations of a single bubble with (“active scalar”) and without (“passive scalar”) convection being considered.

normalizing with the maximum radius  $R_{max}$ , highlights the similarity of the bubble behaviors in all cases. The most salient feature of this behaviour is the fact that the initial fast bubble growth is followed by a dissolution phase already shortly after the end of the potential pulse. Dissolution is more rapid initially and then reduces to slightly lower rates of dissolution at later times.

In the following, we will focus on the experiment performed at  $\phi = -2V$  and  $\tau_p = 60$  s (black line in figures 1.1(c) and 1.3(a)). Here, a bubble happened to nucleate within the initial field of view such that both, the bubble growth and dissolution phases, were captured. In figure 1.3(b), we compare this bubble evolution to simulation results. In the DNS, we used the experimentally determined current density as an input and chose a box size of  $S = 4$  mm, which corresponds to a rough estimate of the typical bubble spacing in the experiments. The importance of convective phenomena is highlighted through a simulation with pure diffusive transport only (setting  $\mathbf{f} = 0$  in (1.3)). In that case, the bubble exhibits continued growth even at late times. In contrast, the simulation with active scalars captures the actual bubble behaviour much more faithfully as evidenced by a dissolution phase, i.e. a shrinking of the bubble radius, that sets in shortly ( $\approx 100$  s) after the current is stopped.

The mechanism behind the different behaviour is best illustrated by figure 1.4, where the hydrogen oversaturation ( $\zeta_{H_2} = C_{H_2}/C_{H_2,sat} - 1$ ) is depicted at several instances in time (indicated as markers in figure 1.3(b)). Initially, for  $t \lesssim 80$  s the production of  $H_2$  at the electrode leads to a significant local oversaturation, which

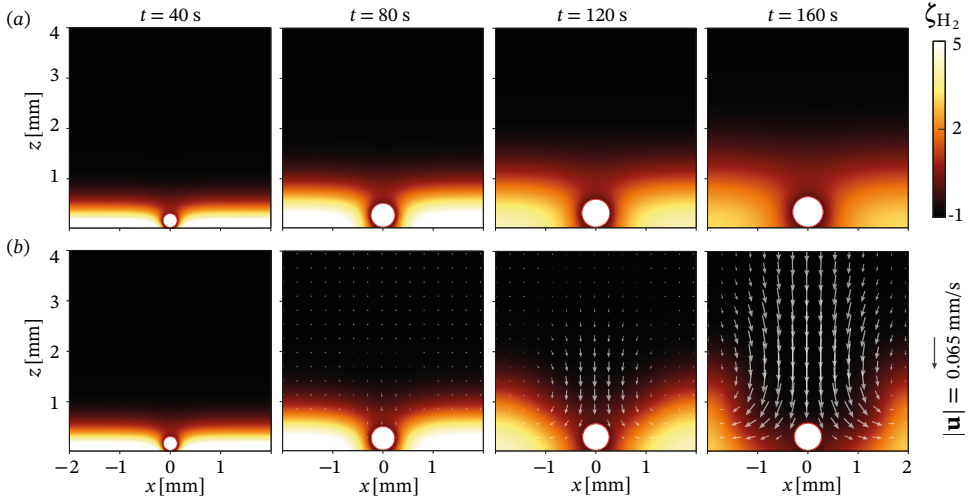


Figure 1.4: Snapshots of hydrogen supersaturation along with velocity vectors for simulations with passive (a) and active scalars (b). The reference vector applies to all panels in (b). The current density is taken from the experimentally measured values (black curve in figure 1.1(c)). The color code shows the hydrogen oversaturation  $\zeta_{\text{H}_2}$ .

spreads by pure diffusion. In the case without buoyancy (figure 1.4(a)), this also holds at later times. The bubble therefore remains in a boundary layer in which  $\zeta_{\text{H}_2} > 0$  even after the potential pulse and therefore continues to grow throughout the entire simulation. The case with buoyancy (figure 1.4(b)) starts to differ significantly from this scenario beyond  $t \approx 80$  s. This is due to the emergence of a downdraft onto the bubble, which is prominent at  $t = 120$  s and even more pronounced at  $t = 160$  s. The effect of this downflow is to displace the  $\text{H}_2$  layer locally, thereby exposing the bubble to undersaturated ( $\zeta_{\text{H}_2} < 0$ ) electrolyte and leading to its dissolution.

These observations lead to two relevant conclusions. Most importantly, they show that the experimental findings cannot be explained by considering pure diffusive transport, but are suitably described by including the effects of natural convection. A more subtle point is that the presence of the bubbles and in particular their spacing in turn seems to have an impact on the convective pattern. After all, the position of the plumes relative to the bubbles appears not to be random. The quick dissolution of all experimentally studied bubbles (figure 1.3(a)) suggests that their location in a downdraft with low gas content is a consistent feature. To investigate how this pinning of the convective pattern to the bubble comes about, we show the distribution of the density change  $\Delta\rho$  relative to the background density  $\rho_0$  in figure

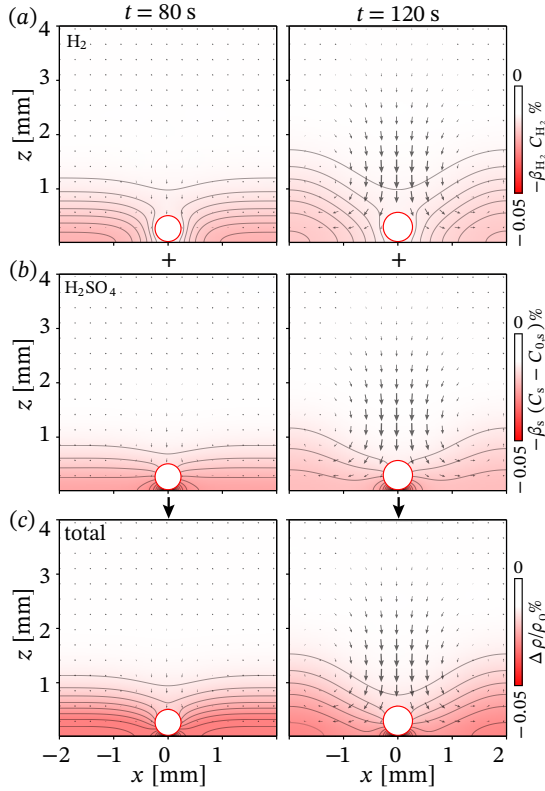


Figure 1.5: Contribution of local concentration variation of (a) hydrogen and (b) sulfuric acid to the (c) total density fluctuations inside the electrolyte at  $t = 80$  s (right panels) and  $t = 120$  s (left panels).

1.5. Variations in  $\Delta\rho$  result from the depletion of  $H_2SO_4$  as well as from the concentration of  $H_2$ . As figure 1.5 demonstrates, both of these effects act to decrease the local density close to the electrode as a consequence of the reaction there. Further, their contributions are of similar magnitudes for the present conditions. However, due to the mass transfer into the bubble, the concentration of  $H_2$  in the vicinity of the bubble is lower, such that the electrolyte density remains somewhat higher there.<sup>⊙</sup> The presence of the bubble further inhibits the diffusion of the sulfuric acid away from the electrode, which has the same effect on  $\Delta\rho$ . This results in a lateral density gradient within the concentration boundary layers. The relatively denser

<sup>⊙</sup>Note that the effect can be opposite for other dissolved gases, e.g.  $CO_2$ , for which  $\beta > 0$ , such that depletion causes the local density to decrease [78].

fluid around the bubble then favours a downdraft in this region and the emission of lighter electrolyte in the form of plumes in the space between bubbles.

It is remarkable that  $\Delta\rho/\rho_0$  remains below 0.05% in the simulations. Yet, consistent with earlier studies [25], this is enough to drive a significant convective flow. We further note that while there is qualitative agreement between experiment and DNS in figure 1.3(b), quantitative differences remain. We will analyse the reasons for these by exploring the parameter space of varying current densities  $i$  and bubble spacings  $S$  next.

### 1.3.1 Effect of current density and bubble spacing

In the following, the pulse duration is kept fixed at 60 s as in the experiment, while the current density and box size  $S$  are varied systematically. We start the considerations from base case with  $|i| = 20 \text{ A/m}^2$  and  $S = 6 \text{ mm}$  (*i20S6*), for which the bubble radius  $R(t)$  is shown as a green line in figure 1.6(a). Even though the parameters of this case differ from those in figure 1.3(b), the bubble behaviour appears qualitatively unchanged. However, at a slightly larger box size of  $S = 7 \text{ mm}$  (*i20S7*, orange line), significant differences arise in the bubble evolution at  $t \approx 150 \text{ s}$ , where a secondary growth phase sets in. The reason for this difference is illustrated by the flow patterns in figures 1.6(d,e). While the plumes rise at the edges of the domain (i.e. halfway between adjacent bubbles) for *i20S6* (figure 1.6(d)), the plumes merge on top of the bubble for *i20S7* (figure 1.6(e)). This implies that at later times, the bubble is no longer surrounded by under-saturated ‘fresh’ electrolyte, but gets exposed to a lateral influx of fluid with high oversaturation  $\zeta_{\text{H}_2}$ , which leads to the renewed growth phase after the initial dissolution. Given the transient driving, the bubble will also dissolve eventually in this case once the initial boundary layers are drained. Remarkably, also increasing the current from the base case to  $|i| = 24 \text{ A/m}^2$  (*i24S6*) can induce the same phenomenon as shown by the red line in figure 1.6(a). An overview over the full parameter space in the range  $8 \text{ A/m}^2 \leq |i| \leq 32 \text{ A/m}^2$  and  $1 \text{ mm} \leq S \leq 8 \text{ mm}$  is shown in figure 1.6(b), where open (full) symbols denote the mode where at later times the plumes merge in between (on top of) the bubbles. From this, it becomes clear that the upward flow is located at the bubble for large  $i$  and  $S$ . This behaviour is related to the lateral density gradient induced by the presence of the bubble: The denser fluid close to the bubble creates a disturbance in the boundary layer (figure 1.5) that travels outward and from which eventually the plumes detach. If the disturbance has travelled close enough to, or even reached the boundary at the onset of convection, the plumes will merge there and rise half-way between the bubbles. If, on the other hand, convection sets in

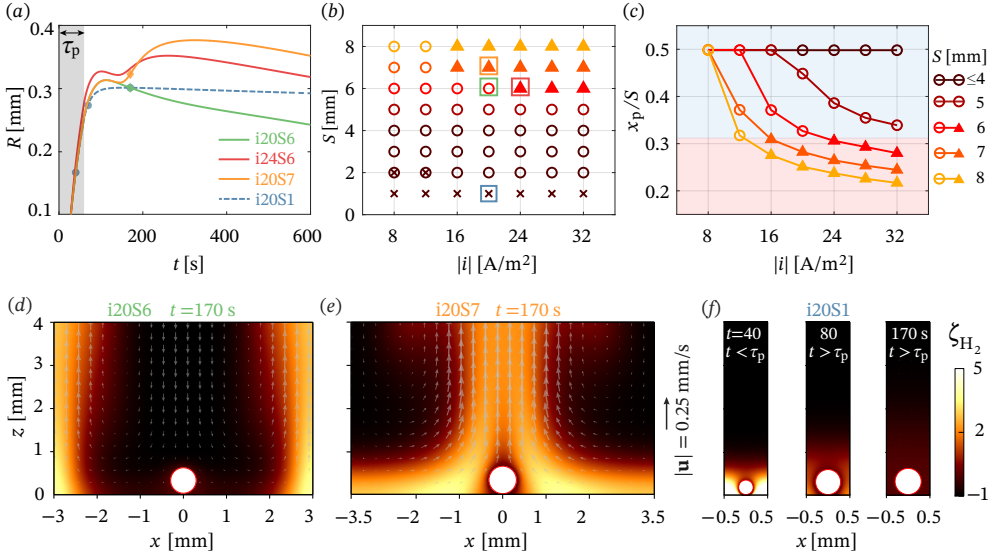


Figure 1.6: (a) Radius evolution for four parameter combinations of  $i$  and  $S$ . (b) Full phase map explored for a 60 s pulse with cases shown in (a) marked by squares. Circles (triangles) indicate plumes merging in between (on top of) the bubbles, crosses represent no convection. (Note that the two cases at  $S = 2$  mm underwent transitions for continuous currents but not with the 60 s pulse). (c) Plume detachment location ( $x_p/S$ ) as function of  $i$ . Symbols as in (b). (d – f) Snapshots of hydrogen contours and velocity vectors corresponding to cases shown in (a): plume between (d) and on top of bubbles (e) and no convection (f). The reference vector in (e) applies to both panels (d) and (e).

while the disturbance is still close to the bubble, the plumes will flap back and merge over the bubble as seen in figure 1.6(e). Increasing the bubble spacing  $S$  increases the distance the disturbance needs to travel before it can interact with the one coming from the adjacent bubble. In contrast, increasing the current density  $i$  shortens the time  $\tau_c$  before convection occurs and hence also the time during which the disturbance can travel before the plumes detach.

In order to confirm this picture, we determine  $\tau_c$  as the time when the convective transport first equals the diffusive flux. Further, we define the location  $x_p$  of the initial plume emission, based on the maximum in the vertical velocity at boundary layer height at time  $t = \tau_c$ . Details for this procedure are given in Appendix 1.5.3. In figure 1.6(c), we present the results in the form of  $x_p/S$  vs.  $i$ . These data show that  $x_p$  indeed tends to decrease with increasing current density. Most importantly, we also find that the plume location at later times depends on  $x_p/S$  as expected

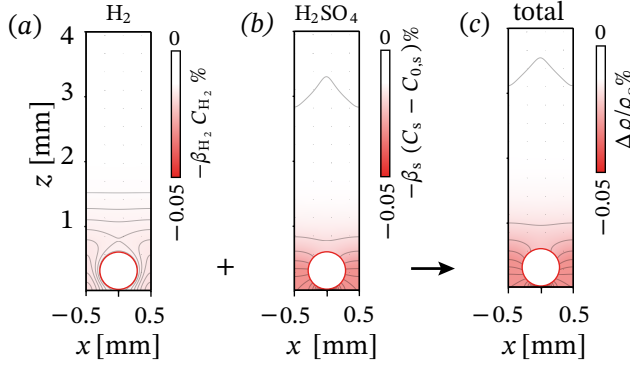


Figure 1.7: Contribution of local concentration variation of (a) hydrogen and (b) sulfuric acid to the (c) total density fluctuations in the electrolyte solution at  $t = 80$  s for the case  $i20S1$  shown in figure 1.6(f) in the main text.

from the above argument. In particular, the criterion for the plumes to merge over the bubbles is determined to be  $x_p/S \lesssim 0.31$  from figure 1.6(c).

Finally, when decreasing the bubble spacing drastically to  $S = 1$  mm ( $i20S1$ ), the bubble size is seen to remain approximately constant after the end of the pulse (blue line in figure 1.6(a)). As shown by the oversaturation contours in figure 1.6(f), the mass transfer to the bubble effectively balances the production of  $H_2$  in this case. This limits the growth of the hydrogen boundary layer and reduces the buoyancy force. Note that a density difference still arises from the depletion of  $H_2SO_4$  (figure 1.7), but the onset of convection is further suppressed by the no-slip condition on the bubble surface, reducing the effective length scale to the bubble spacing instead of the height of the diffusive layer. We therefore observe no convective motion for the cases marked with a cross in figure 1.6(b), which correspond to low  $S$  and low  $i$ .

### 1.3.2 The onset of convection

Next, we will examine the onset of convection and study how this is influenced by the presence of the bubbles. In order to render the considerations independent of the pulse duration  $\tau_p$ , a continuous current is applied in the simulations for this purpose. In figure 1.8, we present results for the time of convection onset  $\tau_c$  for different bubble spacings  $S$  as a function of  $i$ . In addition, the plot also contains data for a reference case without bubbles. Initially focusing on  $S \geq 4$  mm for which a largely undisturbed region exists in between the bubbles,  $\tau_c$  is seen to decrease

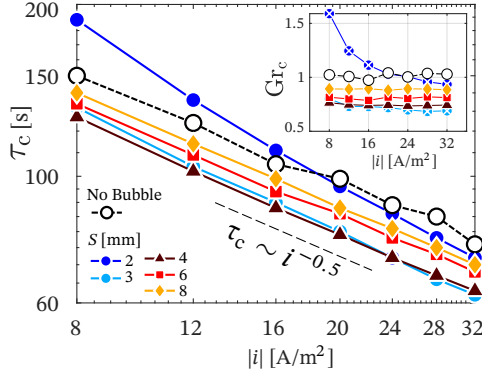


Figure 1.8: Transition time  $\tau_c$  as a function of the current density  $i$ . The inset shows  $Gr_c = Gr(\tau_c)$ ; note that for  $S \leq 2$  mm (marked by a cross),  $Gr_c$  was extrapolated from the  $Gr(t) = f(i, t)$  curve obtained at larger  $S$ .

with  $i$  according to roughly  $\tau_c \sim i^{-1/2}$ . Moreover,  $\tau_c$  at constant  $i$  is largest for the case without bubbles and decreases as the bubble spacing  $S$  is reduced. To gain a better insight into these trends, we define a Grashof number

$$Gr = \frac{g\delta^3}{\nu^2} \frac{-\Delta\rho(z=0)}{\rho_0}, \quad (1.10)$$

which compares buoyancy with viscous forces. Here, the height  $\delta$  of the initial diffusion boundary layer is defined based on the instantaneous density profile normal to the electrode (see Appendix 1.5.4). (2.23) therefore encompasses the full density difference, which originates to approximately equal parts from the distributions of  $H_2$  and  $H_2SO_4$  (see figure 1.5 and 1.13 in Supporting Information). The Grashof number is closely related to the Rayleigh number, which is also frequently used in this context [64, 79–82]. The use of  $Gr$  is preferred here since its definition is independent of the mass diffusivities, which differ for  $H_2$  and  $H_2SO_4$ . Generally speaking,  $Gr$  is an increasing function of time as both  $\delta$  and  $\Delta\rho$  increase with  $t$ . In the inset of figure 1.8, we have plotted  $Gr_c(t = \tau_c)$  at the onset of convection. For  $S \geq 4$  mm, the value of  $Gr_c$  is found to be independent of the current density  $i$ . Still, the value of the critical Grashof number beyond which convection sets in,  $Gr_c$ , depends on the precise bubble configuration and decreases from  $Gr_c \approx 1$  in the absence of bubbles<sup>Ⓢ</sup> to  $Gr_c \approx 0.75$  for  $S = 4$  mm. This gives evidence that the presence of the bubbles destabilizes the boundary layer such that buoyancy driven

<sup>Ⓢ</sup>Using the Schmidt number  $Sc = 404$  of  $H_2SO_4$ , this is consistent with the range of critical Rayleigh numbers  $320 \leq Ra_c = GrSc \leq 817$  reported for temperature [83] and gas diffusion [84] boundary layers.

convective motion sets in earlier. Having established that  $Gr_c = \text{const.}$  for large enough bubble spacings, we can also explain the scaling of  $\tau_c$ : From the solution of a constant flux diffusion problem [85], we get the scalings  $-\Delta\rho(z=0) \sim it^{1/2}$  and  $\delta \sim t^{1/2}$ , such that the Grashof number grows according to  $Gr \sim it^2$ . The latter results in  $t_c \sim i^{-1/2}$ , exactly as observed in figure 1.8.

When decreasing the bubble spacing below  $S = 4$  mm, we notice that  $\tau_c$  does not decrease further at  $S = 3$  mm and eventually increases again for  $S = 2$  mm. Again, this is a combined effect of the  $H_2$  transfer into the bubbles and suppression of flow by their presence. At lower  $i$ , the longer transition times render the mass transfer into the bubble more relevant, which leads to a deviation from the  $\tau_c \sim i^{-1/2}$  scaling, especially at  $S = 2$  mm. The same mechanism is also reflected in a significant increase of  $Gr_c$  with decreasing  $i$  in the inset for  $S = 3$  mm and even more prominently for  $S = 2$  mm. No convection was observed for the tightest spacing of  $S = 1$  mm even with continuous driving.

### 1.3.3 Effect of bubble clustering

The results so far present convincing evidence and insight into the role of convection in the evolution of the hydrogen bubbles on the electrode surface. Yet, single bubble simulations fail to reproduce the experimental results quantitatively (see figure 1.3(b)). Further, these results also did not feature the change in dissolution rate, which is evident to varying degrees for all of the experimental recordings in figure 1.3(a) at about 200 s after the end of the pulse. In the following, we will demonstrate that collective effects of multiple interacting bubbles can explain these differences.

For this purpose, we consider the  $3 \times 3$  cluster of bubbles as shown in figure 1.2(b). For all simulations with clusters, the box size is fixed to  $S = 4$  mm (in all three directions) and the experimentally measured current density during the 60 s pulse is used (see figure 1.1 (c)). Thus, the only parameter which is varied is the inter-bubble spacing  $S_c$ .

The time traces of  $R(t)$  in figure 1.9(a) display a behaviour that is consistent with the convective pattern of plumes rising in between bubbles observed earlier. As expected, there is no difference in the size of bubbles at different locations during the growth period. However, such differences do arise during the dissolution stage, where the central bubble starts dissolving the earliest and at the fastest rate. The transition from growth to dissolution (and to a lesser extent also the final dissolution rate) are progressively slower for the bubbles at the sides and in the corners. This overall picture continues to apply also if the cluster spacing is reduced to  $S_c = 0.6$  mm in figure 1.9(b). The decreased spacing does, however, lead to a fast onset of

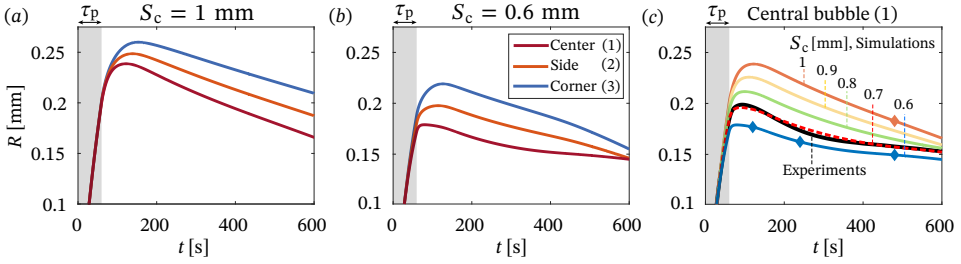


Figure 1.9: Bubble radius evolution in the cluster configuration (a) with  $S_c = 1$  mm and (b)  $S_c = 0.6$  mm. (c)  $R(t)$  for the central bubble only at varying  $S_c$ .

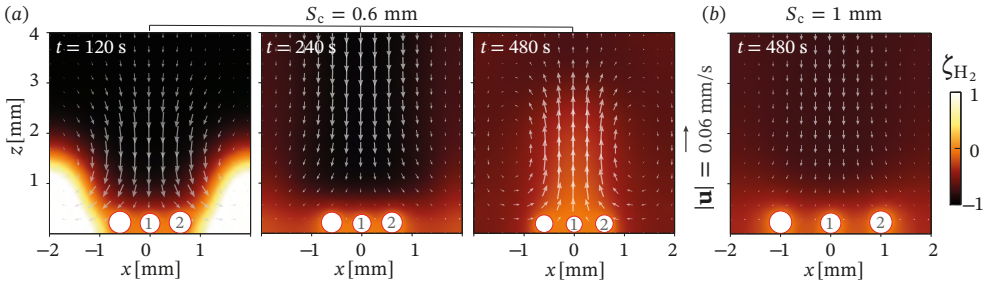


Figure 1.10: Snapshots of the  $H_2$  oversaturation along with velocity vectors for (a)  $S_c = 0.6$  mm and (b)  $S_c = 1$  mm. The reference vector applies to all panels.

dissolution for all bubbles. Moreover, the evolution of the bubble radius with time now also features the distinct change in slope at around  $t = 300$  s, similar to the experimental observations.

Contours plots of the hydrogen oversaturation  $\zeta_{H_2}$  along with the convective patterns in figure 1.10(a) help explain these findings. Since the plumes rise in between the clusters, the downward flow is consequently centered on the bubble in the middle (bubble 1 in figure 1.10), which is therefore most exposed to the undersaturated electrolyte compared to those further out (bubbles 2 and 3). This behaviour is similar for  $S_c = 0.6$  mm and  $S_c = 1$  mm. There are significant differences however at later times. At  $t = 480$  s, an upward flow forms over the dissolving bubble cluster with  $S_c = 0.6$  mm, whereas such a pattern is entirely absent in the case with  $S_c = 1$  mm in figure 1.10(b). An analysis of the corresponding density contours (figure 1.11) reveals that the upward flow is not predominantly driven by variations in the  $H_2$  field resulting from the bubble dissolution. A decisive factor is rather that the depletion of  $H_2SO_4$  caused by the reaction cannot be ‘washed out’ effectively due to the blockage by the tightly spaced bubbles. In this way, lower density electrolyte

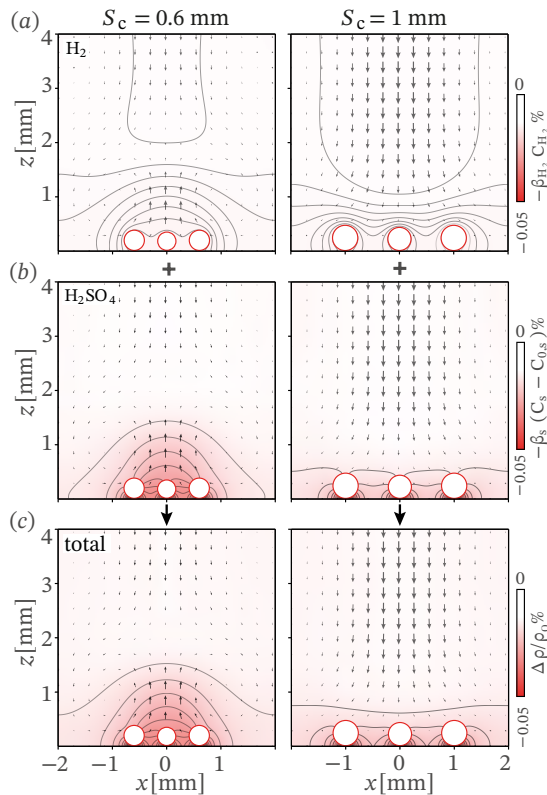


Figure 1.11: Contribution of local concentration variation of (a) hydrogen and (b) sulfuric acid to the (c) total density fluctuations in the electrolyte solution at  $t = 400$  s. The current density is taken from the experimentally measured values (black curve in figure 1.1(c)). The distance between the bubbles in the network is  $S_c = 0.6$  mm for left panels and  $S_c = 1$  mm for right panels.

persists within the cluster and helps drive the observed upward convection at late times. Once convection sets in, the well-known shielding effect [86–88] reduces the dissolution rate of central bubble, while slightly increasing the dissolution rate of the other bubbles (compare also figure 1.9(b) at later times).

The dependence of the general size of the central bubble on  $S_c$  is considerable, as the data in figure 1.9(c) prove. An excellent match between the experimental data and our modeling results is obtained for  $S_c = 0.7$  mm, which is indeed very close to the distance to the neighbouring bubble observed in figure 1.1(b). It therefore appears very likely that collective effects due to the inhomogeneous bubble distribution play an important role in the experiment. This remains true, even if

unaccounted effects, such as the presence of dissolved air, may alter the  $R(t)$  curves slightly.

## 1.4 Conclusion

Our combined experimental and numerical analysis firmly established the relevance of solutal convection for bubble evolution during water electrolysis. The experimentally observed bubble behaviour was shown to be inconsistent with pure diffusive transport, while experiments and simulations were in excellent agreement when natural convection due to buoyancy effects was considered. While appropriate for micro-electrodes [59,60,62], our results suggest that convective effects cannot be neglected when larger electrodes are considered [58,61,89]. For example, estimating based on the  $H_2$  concentration only, a critical value for the onset of convection of  $Gr \approx 1$  should be reached after about 100 s for the conditions reported in van der Linde et al. [58], while their experiments lasted for hours. Our results further show that the presence of bubbles can decrease the stability threshold of the diffusive boundary layers, rendering the system even more prone to convective effects. For the present conditions, this destabilization occurs if  $S \geq 4$  mm, while the onset of convection is delayed or even suppressed entirely if the distance between bubbles is smaller than  $S \leq 1$  mm. We further demonstrated that convective patterns and especially their impact on the bubble evolution vary significantly, depending on the design parameters. This may open up avenues to control flow features to achieve a desired bubble behaviour by providing nucleation sites with optimized spacings. However, there still remain open questions. These pertain e.g. to the potential effect of spatially varying current density due to the presence of the bubbles [51]. Further, a more complete treatment of the problem especially at high values of  $i$  and for tight bubble spacing should also include supporting electrolyte and the effect of Marangoni convection [61,90]. Finally, allowing for bubble detachment in the simulations will enable accessing stages after the initial transient.

## 1.5 Appendix

### 1.5.1 Electrolyte transport equation

Here the derivation of the advection-diffusion equation for  $\text{H}_2\text{SO}_4$  ( $j=s$  in (1.5)) will be presented. We start from the mass-transport equations for dissolved ions given by

$$\frac{\partial C_1}{\partial t} + (\mathbf{u} \cdot \nabla) C_1 = D_1 \nabla^2 C_1 + D_1 z_1 \frac{F}{RT} \nabla \cdot (C_1 \nabla \phi), \quad (1.11)$$

and

$$\frac{\partial C_2}{\partial t} + (\mathbf{u} \cdot \nabla) C_2 = D_2 \nabla^2 C_2 + D_2 z_2 \frac{F}{RT} \nabla \cdot (C_2 \nabla \phi), \quad (1.12)$$

where subscripts 1 and 2 denote  $\text{H}^+$  and  $\text{SO}_4^{2-}$  ions, respectively,  $\phi$  refers to the electric potential field and  $z_k$  denotes the ionic valence i.e.,  $z_1 = +1$  and  $z_2 = -2$ . Employing the electroneutrality condition

$$z_1 C_1 = -z_2 C_2, \quad (1.13)$$

(1.12) can be expressed in terms of  $C_1$  as

$$-\frac{z_1}{z_2} \frac{\partial C_1}{\partial t} - \frac{z_1}{z_2} (\mathbf{u} \cdot \nabla) C_1 = -\frac{z_1}{z_2} D_2 \nabla^2 C_1 - D_2 z_1 \frac{F}{RT} \nabla \cdot (C_1 \nabla \phi). \quad (1.14)$$

Multiplying (1.14) by  $D_1$  and subtracting it from (1.11) multiplied by  $D_2$  gives

$$\left( D_2 - D_1 \frac{z_1}{z_2} \right) \frac{\partial C_1}{\partial t} + \left( D_2 - D_1 \frac{z_1}{z_2} \right) (\mathbf{u} \cdot \nabla) C_1 = D_1 D_2 \left( 1 - \frac{z_1}{z_2} \right) \nabla^2 C_1. \quad (1.15)$$

Rearrangement of the terms in (1.15) by taking into account that  $C_{\text{H}_2\text{SO}_4} = C_{\text{H}^+}/2$  (according to the electroneutrality condition and full dissociation of sulfuric acid in water) yields

$$\frac{\partial C_s}{\partial t} + (\mathbf{u} \cdot \nabla) C_s = D_s \nabla^2 C_s, \quad (1.16)$$

where the electrolyte diffusivity  $D_s$  is defined as

$$D_s = \frac{D_1 D_2 (z_1 - z_2)}{z_1 D_1 - z_2 D_2}. \quad (1.17)$$

Accordingly, equations (1.11) and (1.12) are simplified to the single equation (1.16) thereby eliminating the migration terms.

The proton is reduced at the electrode surface. Using the same steps as above for (1.16), the associated flux of  $H^+$  at the boundary can be related to the current density by

$$\frac{i}{(n_e/s_1)F} = D_1 \left( \frac{\partial C_1}{\partial z} + z_1 C_1 \frac{F}{RT} \frac{\partial \phi}{\partial z} \right)_{z=0}. \quad (1.18)$$

Since the anion is not consumed in the electrochemical reaction on the electrode surface, its flux is zero there. Thus, we obtain

$$\left( \frac{\partial C_2}{\partial z} \right)_{z=0} = -z_2 C_2 \frac{F}{RT} \left( \frac{\partial \phi}{\partial z} \right)_{z=0}, \quad (1.19)$$

which along with electro-neutrality condition yields

$$\left( \frac{\partial C_2}{\partial z} \right)_{z=0} = -\frac{z_1}{z_2} \left( \frac{\partial C_1}{\partial z} \right)_{z=0} = z_1 C_1 \frac{F}{RT} \left( \frac{\partial \phi}{\partial z} \right)_{z=0}. \quad (1.20)$$

Again taking into account that  $C_{H_2SO_4} = C_{H^+}/2$ , (1.20) is used to eliminate the migration terms in (1.18) according to

$$\frac{i}{(n_e/s_1)F} = 2D_1 \left( 1 - \frac{z_1}{z_2} \right) \left( \frac{\partial C_s}{\partial z} \right)_{z=0}, \quad (1.21)$$

which is used as boundary condition for (1.16).

## 1.5.2 Numerical methods

Direct numerical simulations are used to solve the system of equations (1.3) and (1.4) in a three dimensional Cartesian domain as depicted in figure 1.2 in the main text. Spatial terms are discretized using a second-order accurate finite difference method on a staggered grid. A fractional-step third-order Runge-Kutta scheme, in combination with a Crank-Nicolson scheme for the viscous terms are employed to perform the time marching [91, 92]. Periodic boundary conditions for the velocity components and scalar fields are employed at side walls of the Cartesian domain in wall-parallel directions. An outflow boundary condition is applied at the top boundary, through which the diffusive and advective fluxes of both velocity and scalar fields are conserved. The solver is coupled with a versatile moving least squares (MLS) based immersed boundary method (IBM), [93, 94] which uses a triangulated grid network called Lagrangian markers (figure 1.2(a)) to enforce the gas-liquid interfacial boundary conditions, including saturation concentration for

hydrogen and no-flux for other species alongside no-slip and no-penetration conditions for velocity field, and transfer these quantities back to the underlying Eulerian mesh. Therefore, any flow field generated inside the bubble is disregarded as it is irrelevant to the flow physics outside the bubble. The no-slip boundary condition on the bubble is chosen in order to represent a fully contaminated bubble surface [72].

Finally, the location of Lagrangian markers is updated in time based on (1.9). It is further worth mentioning that the concentration gradient  $(\nabla C_j \cdot \hat{\mathbf{n}})|_{\Sigma}$  at the bubble interface is calculated through extending a probe normal to the barycentre of each triangulated Lagrangian face and determining the scalar concentration at the tip of the probe by an additional MLS interpolation.

The computational domain has a fixed height of 4 mm in all cases and has a quadratic outline in the horizontal (parallel to the electrode) plane with varying side length  $S$ . The initial bubble size is limited by resolution requirements. Here, we have chosen the initial diameter of the bubble to be 1/20 of the domain height and used  $\approx 13$  grid points to resolve the initial bubble diameter after checking grid independence. This choice offered a reasonable compromise between starting with the smallest bubble possible and keeping the computational cost at bay. The time at which the bubble is initialized in the simulations (here 28.21 s) with diameter of 0.2 mm has been chosen to match the experimental data (black curve in figure 1.1(c)). The initialization time was also kept constant when varying the current density from the experimental value for consistency. We ran tests with an earlier bubble injection at higher currents in order to confirm that the choice of the bubble initialization time did not change our results significantly.

Physical properties of the analyzed electrochemical system are tabulated in table 1.1. The molar expansion coefficient of hydrogen in sulfuric acid varies depending on the initial concentration of sulfuric acid in water and we have computed it using the correlation proposed by Vogt [95]. The full set of numerical parameters is listed in table 1.2.

### 1.5.3 Transition time and gas plumes location

We base the criterion for the onset of convection on the  $H_2$  distribution and define the transition time  $\tau_c$  as the time at which the averaged advective flux first exceeds the diffusive transport, i.e.,

$$\langle \mathbf{u}_{CH_2} \rangle_{y,z} \geq \langle D_{H_2} \nabla C_{H_2} \rangle_{y,z}, \quad (1.22)$$

where  $\langle \rangle_{y,z}$  denotes an average over the midplane of the domain. figure (1.12) displays samples of the ratio of the advective to diffusive fluxes for  $S = 6$  mm at different current densities, where  $\tau_c$  is marked with crosses.

Properties	Unit
$(C_{\text{H}_2\text{SO}_4})_0 = 100$	$\text{mol m}^{-3}$
$T_\infty = 298$	K
$P_0 = 1$	bar
$\rho_L = 1030$	$\text{kg m}^{-3}$
$\nu_L = 0.94 \times 10^{-6}$	$\text{m}^2 \text{s}^{-1}$
$D_{\text{H}^+} = 9.308 \times 10^{-9}$	$\text{m}^2 \text{s}^{-1}$
$D_{\text{SO}_4^{2-}} = 1 \times 10^{-9}$	$\text{m}^2 \text{s}^{-1}$
$D_{\text{H}_2} = 3.7 \times 10^{-9}$	$\text{m}^2 \text{s}^{-1}$
$k_{\text{H}_2} = 7.2 \times 10^{-6}$	$\text{mol m}^{-3} \text{Pa}^{-1}$
$\beta_{\text{H}_2} = +11.5 \times 10^{-6}$	$\text{m}^3 \text{mol}^{-1}$
$\beta_{\text{H}_2\text{SO}_4} = -62 \times 10^{-6}$	$\text{m}^3 \text{mol}^{-1}$

Table 1.1: Physical properties of the analyzed system.  $k_{\text{H}_2}$  is Henry's constant such that  $C_{\text{H}_2, \text{sat}} = k_{\text{H}_2} P_0$ .

Parameter	Value	Unit
Domain size	$4 \times S \times S$	mm
Initial bubble diameter	0.2	mm
Grid No. per initial bubble diameter	13	
Time step	0.005 – 0.05	s
Bubble injection time	28.21	s

Table 1.2: Numerical setup information

We used the location of the gas plumes at transition time to distinguish two different modes of the convective pattern, which can lead to either enhanced growth or dissolution of the bubble. To determine the plume detachment position  $x_p$ , we consider the horizontal profile of the vertical velocity ( $u_z$ ) at  $z = \delta_{\text{H}_2}$  as shown in figure 1.12(b), where  $\delta_{\text{H}_2}$  is the hydrogen boundary layer thickness sufficiently far from the bubble. We then define  $x_p$  as the location of the peaks in the velocity profile as indicated figure 1.12(b).

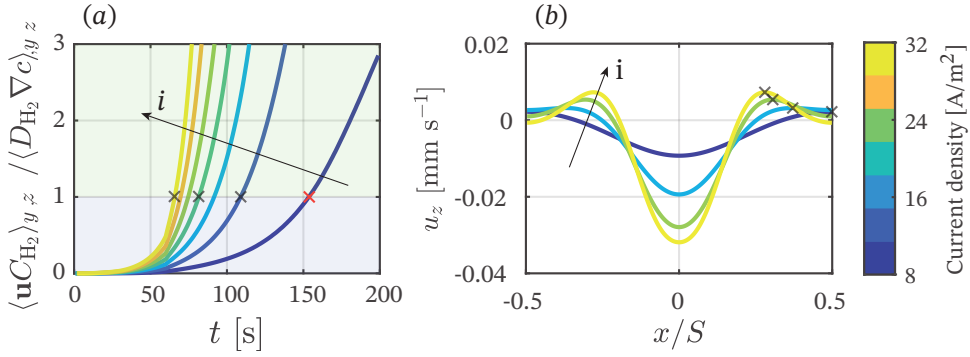


Figure 1.12: (a) Ratio of advective to diffusive fluxes of hydrogen at  $S = 6\text{ mm}$ . Different lines represent varying current density in the range from  $8\text{ A/m}^2$  to  $32\text{ A/m}^2$ . Cross markers indicate the transition time measured at the instants when the ratio of the fluxes is unity. (b) horizontal profile of the vertical component of the velocity ( $u_z$ ) at the edge of the hydrogen boundary layer ( $\delta_{H_2}$ ) at transition times ( $\tau_c$ ) obtained from panel (a). Cross markers locate the peaks in the profile based on which  $x_p$  is determined. Current density is varied from  $8\text{ A/m}^2$  to  $32\text{ A/m}^2$ .

### 1.5.4 Effective diffusion depth

Here, we explain the approach employed for measuring the instantaneous effective diffusion depth  $\delta$ , which accounts for the density variations resulting from the change in concentration of  $\text{H}_2\text{SO}_4$  and hydrogen gas adjacent to the electrode. A typical density profile and its constituents at  $t = 80\text{ s}$  are plotted in figure 1.13. As the figure shows, both hydrogen enrichment and electrolyte depletion contribute approximately equally to the total density variation. We define  $\delta$  as used in the definition of  $Gr$  in (2.23) based on the total density profile according to

$$\delta = \left. \frac{\Delta\rho}{\partial_z(\Delta\rho)} \right|_{z=0}. \quad (1.23)$$

This value is indicated by a black marker in figure 1.13. The ratio of the diffusivities for hydrogen and the sulfuric acid is  $\sqrt{D_{H_2}/D_s} \approx 1.22$ , such that the effective diffusion depths based on these profiles (also included in the figure) differ slightly.

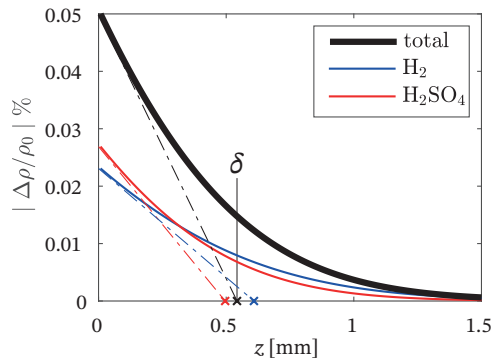


Figure 1.13: Total density variation profile and contributing components for a simulation without bubble and  $|i| = 24 \text{ A/m}^2$ . Profiles are plotted in the centerline of the mid-plane ( $x/S = 0$ ) at  $t = 80 \text{ s}$ . Dashed lines indicate the linear fit at the electrode surface ( $z = 0$ ) to each profile and crosses mark the corresponding locations of  $\delta$ .

# 2

## Mass transport at gas-evolving electrodes <sup>◦</sup>

*In this work, direct numerical simulations are employed to investigate multi-component mass transfer processes at gas-evolving electrodes subjected to successive formation and detachment of bubbles. The gas-liquid interface is modeled employing an Immersed Boundary Method (IBM) coupled with a finite-difference solver for the carrier phase. We simulate the growth phase of the bubbles followed by their departure from the electrode surface in order to study the mixing induced by these processes. We find that the growth of the bubbles switches from a diffusion-limited mode at low to moderate fractional bubble-coverages of the electrode to reaction-limited growth dynamics at high coverages. Furthermore, our results indicate that the net transport within the system is mainly governed by the effective buoyancy driving induced by the rising bubbles such that the resulting gas transport for different bubble sizes, current densities and electrode coverages can be collapsed as a function of an effective Grashof number. The same holds for the electrolyte mixing when additionally taking the the effect of surface blockage by adhering bubbles into account. Next, gas transport to the bubble is quantified and we find that the relevant Sherwood numbers collapse onto a single curve when accounting for the driving force of bubble growth incorporated in an effective Jakob number. Finally, connecting the hydrogen transfer rates at the electrode and bubble interface, an approximate relation for the gas-evolution efficiency is established. Taken together, these findings allow us to deduce parametrizations for all response parameters of the systems, for which only theoretical results exist to date.*

---

<sup>◦</sup>To be submitted as **Farzan Sepahi**, Roberto Verzicco, Detlef Lohse and Dominik Krug, *Mass transport at gas-evolving electrodes*.



## 2.1 Introduction

Production of green hydrogen through water electrolysis is projected to be an important technology to cope with the volatile output from renewable power sources in the future energy mix and as a sustainable feedstock in various industrial processes [1,3,5,6]. For the required upscaling of the production, the formation of gas bubbles on the electrode surface plays a critical role. Attached bubbles lower the efficiency of the electrolyser systems by blocking the active electrode area [49,96,97]. In addition, they increase the cell resistance by lowering the effective conductivity of the electrolyte [47,51,98] which leads to cell overpotential. However, the formation of bubbles is also beneficial as it enhances the mixing of the electrolyte and this aspect will be the main focus of this work.

The evolution of bubbles comprises nucleation, growth and detachment from the electrode surface. Bubble growth occurs due to the diffusive transport of dissolved hydrogen to the gas-liquid interface and its subsequent desorption to the gas phase [43,99]. The eventual detachment may be buoyancy driven [19,100] but can also be a consequence of coalescence events [101]. Bubble evolution can impact mass transfer at the electrode in several ways. This includes local ‘micro-convection’ and diffusion processes induced by bubble growth and break-off from the electrode surface [77,102], and also macro-convection within the bulk electrolyte caused by frequent detachment and rise of bubbles within the electrolyte solution [103–106]. The latter process is also referred as two-phase buoyancy-driven convection as it is resulting from the density variations in gas-in-liquid dispersion, and enhances the mass transport by mixing the electrolyte solution in electrode proximity via the established macro-flow pattern. Similar to forced convection effects induced by pressure gradient or magnetic field [107–111], such flow structure pumps the fresh bulk electrolyte to the electrode surface replacing the reactant-depleted and gas-enriched solution in the electrode boundary layer [112]. The significance of two-phase buoyancy-driven convection is further emphasized by the fact that the efficiency of electrochemical systems reduced remarkably under microgravity condition. This adverse effect was attributed to the prolonged adherence of the bubbles to the electrode, inhibiting proper mixing, as well as their growth to inordinate sizes, which further impeded the mass transfer to the electrode [113–118].

These different mass transfer mechanisms were studied separately in the literature. Ibl *et al.* (1971) [119] established the first mass transfer relation for the diffusive micro-processes associated with bubble evolution. This model neglected convection and focused on reactant diffusion to a microarea on the electrode surface affected during the waiting period after bubble detachment and nucleation of the subse-

quent one. This relation was later modified by Roušar & Cenzer (1975) [99] and Vogt & Stephan (2015) [77] to additionally account for diffusive transport during bubble growth, when the size of the microarea shrinks over time and becomes fractionally inactive under the bubble foot. Furthermore, the impact of micro-convection resulting from bubble growth on mass transfer at the microarea, was first quantified by Stephan & Vogt 1979 [102]. Additionally, Vogt & Stephan 2015 [77] took into consideration the impact of wake flow, which is induced by the bubble break-off, on mass transfer at the microarea. Based on their considerations, these authors conclude that micro-convection of bubble growth and detachment is the primary controlling factor for mass transfer when the gas-evolution rate is sufficiently high, particularly at moderate and large current densities. This model is almost exclusively based on theoretical considerations, but has extensively been used for practical applications by other authors [11,120].

In contrast to the the findings of Stephan & Vogt 1979 [102] and Vogt & Stephan 2015 [77], who identified the micro-convective processes of gas-evolution as the dominant mechanism, Janssen & Hoogland (1970, 1973) [75, 121], Janssen (1978) [122] and Janssen & Barendrecht (1979) [103] provided evidence that mass transfer at the electrode was governed by two-phase free convection driven by rising bubbles. This was corroborated by measurements conducted on hydrogen evolving electrodes, with no coalescence of bubbles, where the boundary layer thickness, as a function of volumetric gas evolution rate, exhibited a power law relationship with an exponent of  $1/3$ . This observation highlighted the analogy between such flows, induced by density variations in gas-in-liquid dispersion, and single-phase natural convection in heat and mass transfer problems [123,124]. These findings by different authors are indeed contradictory, and as of our current knowledge, there is no consensus on the rate-controlling mechanism, let alone a well-controlled quantification, of mass transfer at gas-evolving electrodes.

Numerous attempts have been made in the literature to combine experiments and numerical simulations to study the bubble-induced convection at gas-evolving electrodes [125]. Hydrodynamics of two-phase flow and their influence on mass transfer and reaction rate at the electrode have been modeled employing Euler-Euler [65, 126–130], or Euler-Lagrange [125, 131–133] approaches, in neither of which the gas-liquid interface of the bubble were resolved. However, only interface-resolved simulations are capable of capturing the micro-convection as a result of bubble growth and break-off. Several authors performed numerical simulations to study the dynamics of bubble growth coupled with electrokinetics of gas-evolution reaction at the electrode using immersed boundary method (IBM) [18] or body-fitted grids [134, 135]. Other relevant dynamics of bubbles near the electrodes such as co-

alescence, detachment and rising have separately been investigated with interface-resolved simulations [136, 137]. However, none of these studies treats the effect of bubble growth micro-convection and two-phase buoyancy-driven convection simultaneously.

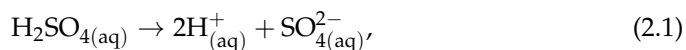
Despite numerous studies targeting the interplay between two-phase hydrodynamics and electrochemical phenomena at gas-evolving electrodes, the question of whether the primary mass transfer mechanism is attributed to the micro-convective processes of bubble growth [77, 102] or two-phase free convection of gas-in-liquid dispersion [103], remains unsettled. Therefore, we aim to perform interface-resolved direct numerical simulations to account for various mechanisms in play by electrolytically-generated gas bubbles. In particular, we look into the successive processes of bubble growth and rise in the electrolyte solution [58, 138] until an equilibrium state is reached, i.e. the global statistics of the system no longer varies in time. Our findings provides a broader perspective over different mass transfer processes at the electrode and bubble interface by leveraging disentangled parameters in the numerical simulations.

The remainder of this chapter is structured as follows; the problem set-up and governing equations are discussed in § 2.2. The results for bubble dynamics and mass transfer rates at the electrode are presented in § 2.3. Mass transfer to the bubble and gas-evolution efficiency are quantified in § 2.4 and § 2.5. Finally, we summarize and discuss our findings in § 2.6.

## 2.2 Configuration and numerical methods

### 2.2.1 Problem set-up

The electrochemical model considered here concerns a water-splitting system with dilute sulfuric acid ( $\text{H}_2\text{SO}_4$ ,  $500 \text{ mol/m}^3$ ) as electrolyte. A schematic is provided in figure 2.1(a) demonstrating the chemical reactions at the cathodic part of the cell. Full dissociation of sulfuric acid to sulphate ( $\text{SO}_4^{2-}$ ) and hydrogen ( $\text{H}^+$ ) ions is assumed according to



and in order to avoid further complications, self-ionization of water is disregarded due to its low equilibrium constant at room temperature. The cathodic reactions solely comprise the Hydrogen Evolution Reaction (HER) as

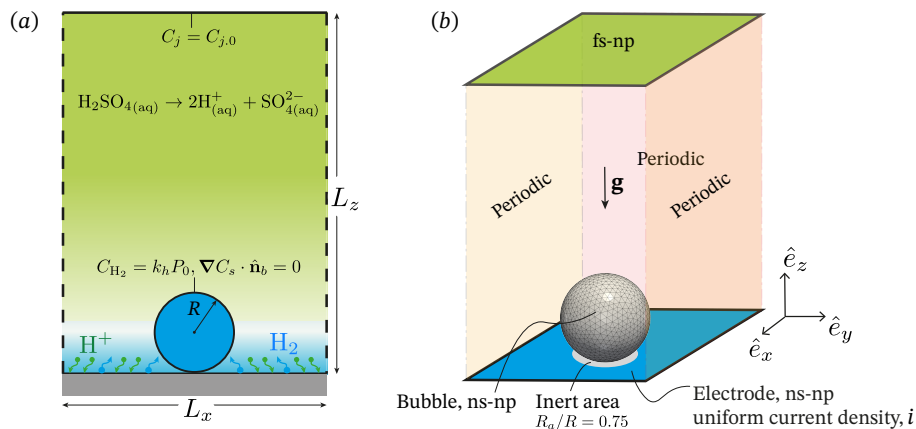


Figure 2.1: (a) Schematic representation of the two-phase electrochemical system with relevant chemical reactions and boundary conditions at the cathode. (b) Sketch of the 3-dimensional numerical setup with the applied boundary conditions for the velocity field (periodic, no-slip (ns), no-penetration (np) and free-slip (fs)). The bubble is modeled with IBM using a triangulated Lagrangian grid on the bubble interface (a sample is illustrated in panel (b)). Current density is uniformly distributed on the electrode surface except for an inactive ( $i = 0$ ) circular part with an outer radius of  $R_a = 0.75R$  under the bubble.



whereby the hydrogen enrichment and electrolyte depletion co-occur within a mass-transfer boundary layer in the vicinity of the electrode as schematically illustrated in figure 2.1(a).

The numerical set-up is a cuboid box as depicted in figure 2.1(b). The electrode is oriented horizontally ( $x$  and  $y$  directions) such that the gravitational acceleration  $\mathbf{g}$  acts normal to it in the negative  $z$  direction. A fully spherical bubble is initialized with a certain radius ( $R_0 = 50 \mu\text{m}$ ) and zero-degree contact angle on the electrode. The bubble subsequently grows to a prescribed diameter, namely the break-off diameter  $d_b$ , before it departs from the electrode surface and rises within the electrolyte solution due to its buoyancy. This process then repeats with the next bubble initialized at the same spot as soon as the previous bubble exits from the top boundary. By applying periodicity in the lateral directions of the computational domain, the set-up replicates a system of monodisperse bubbles with uniform spacing of  $S = L_x = L_y$ , which grow and rise in the medium simultaneously. The initialization, growth and rise of the bubbles in succession are modeled until an equilibrium

Configuration				$ i $ [A/m <sup>2</sup> ]
Constant bubble spacing, $L_x = L_y = 2$ mm				$10^1$
No.	$d_b$ [mm]	$\Theta$	$N_x \times N_y \times N_z$	$1.7 \times 10^1$
1	0.3	0.018	$144^2 \times 288$	$3.0 \times 10^1$
2	0.5	0.05	$144^2 \times 288$	$5.4 \times 10^1$
3	0.7	0.10	$144^2 \times 288$	$10^2$
4	0.9	0.16	$144^2 \times 288$	$1.7 \times 10^2$
Constant bubble size, $d_b = 0.5$ mm				$3.0 \times 10^2$
No.	$L_x = L_y$ [mm]	$\Theta$	$N_x \times N_y \times N_z$	$5.4 \times 10^2$
5	3	0.021	$216^2 \times 288$	$1.0 \times 10^3$
6	2	0.05	$144^2 \times 288$	$1.7 \times 10^3$
7	1.33	0.11	$96^2 \times 288$	$3.0 \times 10^3$
8	0.89	0.25	$64^2 \times 288$	$5.4 \times 10^3$
9	0.70	0.40	$48^2 \times 288$	$10^4$
10	0.59	0.60	$42^2 \times 288$	

Table 2.1: Simulation parameters for cases with varying bubble departure diameter at constant bubble spacing, and with varying bubble spacing at a fixed bubble departure diameter. The domain height is  $L_z = 4$  mm for all the simulation cases. At each configuration, the simulations are performed at 13 different current densities as listed in the last column, leading to 130 simulation cases in total.

state is attained, i.e. the averaged mass transfer statistics, which will be introduced in § 2.2.3, remain constant in time.

The control parameters for the electrolytically-generated two-phase free convective flow are the cathodic current density  $i$ , the bubble break-off diameter  $d_b$ , and the bubble spacing  $S$ . Simulations are performed with two different sets of configuration as listed in table 2.1; in the first set the bubble spacing is kept constant while the bubble break-off diameter is varied. In the second set, spacing between the bubbles is varied at a constant break-off diameter of the bubbles to investigate the effect of bubble population density on the mass transport at the electrode. An auxiliary parameter for either set is the fractional bubble coverage of the electrode,  $\Theta$ , which refers to the fraction of the electrode area shadowed by the orthogonal projection of the bubble surface. Therefore, it is formulated as  $\Theta = \pi d_b^2 / 4A_e$ , where  $A_e = L_x L_y$  is the electrode area available for a single bubble. At each configuration, 13 current densities within the range  $10^1 \leq |i| \leq 10^4$  A/m<sup>2</sup>, as listed in table 2.1, are simulated.

Symbol	Description	Value	Unit
$C_{s,0}$	H <sub>2</sub> SO <sub>4</sub> initial concentration	500	mol/m <sup>3</sup>
$C_{H_2,0}$	H <sub>2</sub> initial concentration	0	mol/m <sup>3</sup>
$C_{H_2,sat}$	H <sub>2</sub> saturation concentration	0.72	mol/m <sup>3</sup>
$T_0$	Ambient temperature	298	K
$P_0$	Ambient pressure	1	bar
$\mathcal{R}$	Gas universal constant	8.314	J/mol · K
$\rho_L$	Electrolyte density	1030	kg/m <sup>3</sup>
$\rho_G$	H <sub>2</sub> density	1	kg/m <sup>3</sup>
$\mu$	Electrolyte dynamic viscosity	$1.03 \times 10^{-3}$	kg/s · m
$\nu$	Electrolyte kinematic viscosity	$1.0 \times 10^{-6}$	m <sup>2</sup> /s
$D_{H^+}$	H <sup>+</sup> diffusivity	$9.308 \times 10^{-9}$	m <sup>2</sup> /s
$D_{SO_4^{2-}}$	SO <sub>4</sub> <sup>2-</sup> diffusivity	$1.0 \times 10^{-9}$	m <sup>2</sup> /s
$D_s$	H <sub>2</sub> SO <sub>4</sub> diffusivity	$2.47 \times 10^{-9}$	m <sup>2</sup> /s
$D_{H_2}$	H <sub>2</sub> diffusivity	$3.7 \times 10^{-9}$	m <sup>2</sup> /s
$k_{h,H_2}$	H <sub>2</sub> Henry's constant	$7.2 \times 10^{-6}$	mol/m <sup>3</sup> · Pa

Table 2.2: Physical properties of the analyzed system.

## 2.2.2 Governing equations

### Carrier phase

Three-dimensional transient incompressible Navier-Stokes equations in Cartesian coordinate system are adopted to solve for the velocity field,  $\mathbf{u}$ , which include the continuity and momentum equations as

$$\nabla \cdot \mathbf{u} = 0, \quad (2.3)$$

and

$$\frac{\partial \mathbf{u}}{\partial t} + \nabla \cdot (\mathbf{u}\mathbf{u}) = -\nabla P + \nu \nabla^2 \mathbf{u} + \mathbf{f}_u, \quad (2.4)$$

where  $\nabla$  is the gradient operator vector,  $P$  and  $\nu$  are the kinematic pressure and viscosity of the solution and  $\mathbf{f}_u$  denotes the IBM direct forcing term used to enforce the velocity boundary conditions on the bubble interface.

In the most general case, the distribution of the H<sub>2</sub>SO<sub>4</sub> would need to be obtained by solving the advection-diffusion-migration equation for its constituent ions

( $\text{H}^+$ ,  $\text{SO}_4^{2-}$ ). Yet, for a binary electrolyte it is possible to simplify the problem by assuming electroneutrality throughout the electrolyte [17], thus eliminating the migration terms between the ions transport equations. Hence, a single transport equation for  $\text{H}_2\text{SO}_4$  with an effective diffusivity is obtained (see chapter 1 and [70]). Additionally accounting for  $\text{H}_2$ , the transport of each substance,  $C_j$ , in the system can be described by an effective advection-diffusion equation as

$$\frac{\partial C_j}{\partial t} + \nabla \cdot (\mathbf{u}C_j) = D_j \nabla^2 C_j + \mathbf{f}_{C_j}, \quad (2.5)$$

where the subscript  $j = (s, \text{H}_2)$  refers to  $\text{H}_2\text{SO}_4$  and  $\text{H}_2$  respectively. Here,  $\mathbf{f}_{C_j}$  is the IBM forcing term to enforce the respective gas-liquid interfacial condition for each substance and will be explained in § 2.2.2. The effective diffusivity of  $\text{H}_2\text{SO}_4$  can be obtained from the diffusion coefficients,  $D_k$ , and ionic valences,  $z_k$ , of the ions ( $k = 1, 2$  denotes  $\text{H}^+$  and  $\text{SO}_4^{2-}$ , see table 2.2 for ions diffusivity) as

$$D_s = \frac{D_1 D_2 (z_1 - z_2)}{z_1 D_1 - z_2 D_2}. \quad (2.6)$$

The no-slip impermeable condition is applied on the electrode. A uniform current density,  $i = I/A_e$  where  $I$  and  $A_e$  are respectively the overall electric current and electrode surface area, is spread on the electrode surface except for an inactive area with instantaneous radius of  $R_a = 0.75R$  [77] underneath the bubble where zero current density is applied (see figure 2.1(b)). The current density in the outer region is therefore corrected slightly as the bubble grows in order to keep the overall electric current,  $I$ , constant throughout the simulations. The cathodic set of boundary conditions for  $C_j$  reads (chapter 1 and [70])

$$\frac{i}{(n_e/s_1)F} = 2D_1 \left(1 - \frac{z_1}{z_2}\right) \left(\frac{\partial C_s}{\partial z}\right)_{z=0}, \quad (2.7)$$

$$-\frac{i}{(n_e/s_{\text{H}_2})F} = D_{\text{H}_2} \left(\frac{\partial C_{\text{H}_2}}{\partial z}\right)_{z=0}. \quad (2.8)$$

Here,  $n_e = 2$  is the number of the transferred electrons in the cathodic reaction (2.2),  $s_1 = 2$  and  $s_{\text{H}_2} = 1$  are the stoichiometric coefficients of the ions and  $F = 96485 \text{ Cmol}^{-1}$  is the Faraday constant. After simplification, the corresponding cathodic flux  $J_j = D_j \left(\frac{\partial C_j}{\partial z}\right)_{z=0}$ , for each species can be related to the current density via the Faraday constant as

$$J_s = \frac{1}{3} \frac{i}{F} \frac{D_s}{D_1}, \quad \text{and} \quad J_{\text{H}_2} = -\frac{i}{2F}. \quad (2.9)$$

While generally the boundary conditions at the top boundary are free-slip no-penetration and constant concentrations for the velocity and scalar fields, respectively, a remedy is required to allow the bubble pass the top boundary. For this purpose, we momentarily change the boundary condition to an in-outflow condition once the bubble arrives at the top boundary and revert back to the original boundary conditions once the bubble has left the computational box. The bubble passes through the top boundary with a constant velocity equal to its rise velocity before the boundary condition switch. We ensured that the computational domain was sufficiently high such that this procedure has negligible influence on mass transfer processes at the electrode. Moreover, periodic boundary conditions for the velocity and concentration fields are employed in the lateral directions of the computational domain. The choice of these boundary conditions is such that the corresponding pure-diffusion problem reaches a steady state for which an analytical self-similar solution exists [58, 139]. Thus, the known mass transfer rate of the pure-diffusion problem can be served as a base system for comparison of mass transfer change resulting from the bubbly flows within the electrolyte (see § 2.3).

In order to numerically obtain the solution of (2.3), (2.4), and (2.5), a second-order accurate central finite-difference scheme is employed for spatial discretization and time-marching is performed with a fractional step third-order accurate Runge-Kutta scheme [92, 140]. A multiple-resolution strategy [141], with refinement factor of two for the scalar fields, is used to solve the momentum and scalar equations, to cope with the fact that the mass diffusivity is several orders of magnitudes smaller than momentum diffusivity. The grid is equally spaced in all directions. A grid independence check has also been performed and is reported in Appendix 2.7.2.

### Dispersed phase

Numerically, we represent the growth and rise phases of the bubbles but circumvent the intricacies of the nucleation process by initializing the bubbles with a finite size of  $R_0 = 50 \mu\text{m}$ . During the growth phase, the expansion rate of the bubble is directly related to the diffusive transport of the dissolved gas across the gas-liquid interface which is determined by Fick's law. Balancing the rate of the change of mass within the bubble and the diffusive flux of hydrogen across the interface as

$$\dot{N}_b = \frac{\mathcal{R}T_0}{P_0} 4\pi R^2 \frac{dR}{dt} = \int_{\partial V} D_{\text{H}_2} \nabla C_{\text{H}_2} \cdot \hat{\mathbf{n}}_b \, dA, \quad (2.10)$$

yields the bubble growth rate

$$\frac{dR}{dt} = \frac{\mathcal{R}T_0}{P_0} \frac{1}{4\pi R^2} \int_{\partial V} D_{\text{H}_2} \nabla C_{\text{H}_2} \cdot \hat{\mathbf{n}}_b dA, \quad (2.11)$$

where  $\mathcal{R}$ ,  $T_0$  and  $P_0$  are the gas universal constant, ambient temperature and pressure respectively.  $R$  is the instantaneous radius of the bubble and  $\hat{\mathbf{n}}_b$  is the unit normal vector at the surface  $\partial V$  of the bubble. Here, we assume a constant pressure inside the bubble throughout the growth phase, which is valid since for the range of bubble sizes  $R \geq 50 \mu\text{m}$  the Laplace pressure is negligible compared to the ambient pressure of  $P_0 = 1 \text{ bar}$ . We further confirmed that inertial effects on the pressure inside the bubble can be neglected by quantifying this effect for the largest bubble growth rates encountered based on the Rayleigh-Plesset equation.

The bubble detaches and rises under the influence of buoyancy in the electrolyte solution after growing to a prescribed departure diameter,  $d_b$ . Note that we do not consider a potential bubble growth during the rise phase. Given the short rise times ( $\sim 0.1 \text{ s}$ ) compared to the residence time of the bubble on the electrode ( $\sim 1 - 100 \text{ s}$ ) and the significantly lower hydrogen concentrations outside the boundary layer at the electrode, this has no sensible effect on our results. The bubble is treated as a spherical rigid particle during the rising phase and its deformation is disregarded due to its small size ( $d_b < 1 \text{ mm}$ ), i.e. surface tension forces, which maintain the spherical form of the bubble, are predominant over inertia and drag forces in the ascent (Weber and Capillary numbers are significantly lower than unity). We solve for the translational velocity of the bubble,  $\mathbf{u}_b$ , which is governed by the Newton's second law of motion as

$$\rho_g V_b \frac{d\mathbf{u}_b}{dt} + \mathbf{F}_v = \int_{\partial V_b} \boldsymbol{\tau} \cdot \hat{\mathbf{n}}_b dA + (\rho_G - \rho_L) V_b \mathbf{g} + \mathbf{F}_v, \quad (2.12)$$

where

$$\mathbf{u}_b = \frac{d\mathbf{x}_b}{dt}, \quad \boldsymbol{\tau} = -p\mathbf{I} + \mu (\nabla \mathbf{u} + \nabla \mathbf{u}^T) \quad \text{and} \quad \mathbf{F}_v = C_v \rho_L \frac{d\mathbf{u}_b}{dt}. \quad (2.13)$$

Here,  $\mathbf{x}_b$  is the bubble centroid position,  $\rho_G$  and  $\rho_L$  are the gas and fluid densities, respectively,  $V_b$  is the bubble volume after detachment, and  $\boldsymbol{\tau}$  is the stress tensor for Newtonian fluids. Following Schwarz *et al.* (2015) [142], the virtual mass term,  $\mathbf{F}_v$  with  $C_v > 0$  is added to both sides of (2.13) in order to stabilize the numerical scheme in view of the very low gas-fluid density ratio. In the present work, the latter is set to  $\text{Gamma} = \rho_G/\rho_L = 0.001$  and the bubble motion equation is solved

with  $C_v = 0.5$ . We resort to virtual mass method with standard IBM here due to the rather simple wake flow of the light rising bubbles at low Reynolds number. A comparison between our simulation results and those of *et al.* (2015) [142], presented in Appendix 2.7.1, demonstrates reasonable accuracy and reliability of this method for the problem under investigation in this study. However, in case of higher Reynolds in which wake instabilities lead to complex flow motion, one may consider using more robust but computationally much more demanding methods like IBM with strong coupling of fluid-structure interaction [143] or IBM projection method [144, 145]. It is worth noting that the hydrodynamic force on the bubble is related to the IBM forcing term,  $\mathbf{f}_u$ , as follows [146–148]

$$\int_{\partial V_b} \boldsymbol{\tau} \cdot \hat{\mathbf{n}}_b \, dA = -\rho_L \int_{V_b} \mathbf{f}_u \, dV + \rho_L \frac{d}{dt} \left( \int_{V_b} \mathbf{u} \, dV \right). \quad (2.14)$$

A set of the boundary conditions for the carrier phase on the bubble interface is required for the concentration and velocity fields. Saturation concentration based on Henry's law ( $C_{\text{H}_2, \text{sat}} = k_h P_0$  with  $k_h$  being the Henry's constant) for  $\text{H}_2$  and zero flux ( $\nabla C_s \cdot \hat{\mathbf{n}}_b = 0$ ) for  $\text{H}_2\text{SO}_4$  are applied on the bubble interface. Assuming a fully contaminated bubble [72], the no-slip no-penetration condition is employed on the bubble interface ( $|\mathbf{x} - \mathbf{x}_b| = R$ ) such that the velocity  $\mathbf{u}|_{\partial V}$  of a point on the bubble surface is given by

$$\mathbf{u}|_{\partial V} = \mathbf{u}_b + \frac{dR}{dt} \hat{\mathbf{n}}_b, \quad (2.15)$$

which is coupled to the mass transfer via (2.11) to determine the bubble growth rate  $dR/dt$ . To ensure continuity within the domain during the bubble growth, the continuity equation needs to be revised by adding a source term in the bubble interior according to

$$\nabla \cdot \mathbf{u} = \phi \frac{3}{R} \frac{dR}{dt}, \quad (2.16)$$

where  $\phi$  is an indicator function which smoothly transitions from 0 to 1 based on a cut-cell method [147] for the cells outside and inside the bubble respectively. This amendment is necessary for modeling expanding/shrinking boundaries using an incompressible solver with IBM. The same approach has also been adopted in the literature for simulation of the flows with evaporating droplets [149, 150]. The local velocity field is still entirely divergence free outside the bubble and the

nonzero divergence inside the bubble is irrelevant to the flow physics outside due to the boundary conditions enforced on the gas-liquid interface. To ensure the global conservation of the mass in the course of the bubble growth, a small but non-zero uniform vertical velocity is prescribed at the top boundary such that the outflow rate equals the expansion rate of the bubble, similar to the simulations of evaporating droplets in the wall-bounded turbulent flows using IBM [150].

The bubble interface is discretized using another triangulated Lagrangian grid as depicted in figure 2.1(b). The IBM method here is based on moving least squares (MLS) approach to conduct the interpolation and distribution of the direct forcing terms between the Eulerian and Lagrangian grids [94, 151, 152]. The enforcement of the Dirichlet and Neumann conditions on the interface for  $H_2$  and  $H_2SO_4$  is performed employing a ghost-cell based IBM to ensure the conservation of the species [153]. To validate these procedures, we verified that mass conservation for the hydrogen distribution is full-filled in our simulations (see Appendix 2.7.3).

### 2.2.3 Response parameters

The most basic response parameters relate to the transport of  $H_2$  away and  $H_2SO_4$  towards the electrode. Since the respective rates of production and consumption at the electrode,  $J_{H_2}$  and  $J_s$ , are constant in time, the effective transport is reflected in difference between the surface averaged concentrations of hydrogen,  $\hat{C}_{H_2,e}$  and electrolyte,  $\hat{C}_{s,e}$ , at the electrode surface and their respective initial values in the bulk ( $C_{H_2,0}$  and  $C_{s,0}$ ). We can normalize these differences using the fluxes  $J_j$  and the bubble diameter  $d_b$  as reference scales to yield the Sherwood numbers

$$\hat{Sh}_{H_2,e} = \frac{J_{H_2} d_b}{D_{H_2} (\hat{C}_{H_2,e} - C_{H_2,sat})}, \quad \text{and} \quad \hat{Sh}_{s,e} = \frac{J_s d_b}{D_s (C_{s,0} - \hat{C}_{s,e})}. \quad (2.17)$$

Here and in the following the hat is used to indicate time-dependant response parameters ( $\hat{\psi}$ ) and a time average over a bubble-period is implied otherwise. By introducing the boundary layer thickness  $\hat{\delta}_j = D_j \Delta \hat{C}_j / J_j$ , this Sherwood number can equivalently be expressed as  $\hat{Sh}_{j,e} = d_b / \hat{\delta}_j$ . For pure diffusion,  $\hat{\delta}_j$  ultimately reaches the cell height irrespective of current density such that the same steady-state value of  $\hat{Sh}_{j,e}$  would be obtained for all cases without the effect of the bubbles.

Analogously, we characterise the mass transfer of hydrogen into the bubble using the bubble Sherwood number

$$\hat{Sh}_{H_2,b} = \frac{2\dot{R}R}{\frac{\mathcal{R}T_0}{P_0} D_{H_2} (\hat{C}_{H_2,e} - C_{H_2,sat})}. \quad (2.18)$$

which employs the time-dependant bubble diameter,  $2R$ , the instantaneous surface area,  $4\pi R^2$ , and the concentration difference between the electrode and bubble interface,  $(\hat{C}_{\text{H}_2,e} - C_{\text{H}_2,\text{sat}})$ , for normalization of the mass flux into the bubble given by (2.10).

A final important output is the fraction of the total hydrogen produced that ends up in gaseous form, i.e. gets desorbed into the bubble [76, 105, 154, 155]. Mathematically formulating this leads to an expression for the gas evolution efficiency

$$f_G = \frac{\frac{V_b}{\tau_c}}{\frac{\mathcal{R}T_0}{P_0} \frac{-i}{n_e F} A_e} = \frac{\dot{V}_G}{\frac{\mathcal{R}T_0}{P_0} \frac{-i}{n_e F} A_e}, \quad (2.19)$$

where  $\tau_c = \tau_g + \tau_r$  is the bubble life-time which comprises the bubble residence (growth) time,  $\tau_g$ , and the bubble rise time,  $\tau_r$ .  $\dot{V}_G = V_b/\tau_c$  is the volumetric gas flux into the gas phase.

## 2.3 Bubble dynamics and mass transfer at the electrode

To begin with, we present the simulation results for a bubble departure diameter of  $d_b = 0.5$  mm and spacing  $S = 2$  mm. The physical properties of the system are set in accordance to table 2.2. Figure 2.2(a) shows the growth dynamics of successively generated bubbles on the electrode at four different current densities. At each current density, the first few bubbles show a slower growth while the supersaturation level of the gas in the electrode boundary layer is building up and the growth pattern becomes more repetitive at later times. This is also reflected in the bubble growth time, which drops initially, but remains constant for subsequent bubbles later on (see inset of figure 2.2(b)). These observations are indicative of an equilibrium state, in which the time-averaged mass transport and gas production rates at the electrode surface are balanced, leading to the repetition of the same growth dynamics for bubbles evolving in sequence. The bubble size evolution at statistically steady-state is plotted and compared in figure 2.2(b) for different current densities. These curves have been taken at times when the bubble residence time,  $\tau_g$ , with bubble number,  $n$ , no longer varies as depicted in the inset. Despite the fact that the bubble growth time varies several order of magnitudes from 100 s to less than 0.1 s when increasing the current density from  $10^1$  to  $10^4$  A/m<sup>2</sup>, the growth dynamic pertaining to diffusion-limited growth, i.e.  $R \propto t^{1/2}$ , is maintained [156, 157]. This is evidenced by the double-logarithmic plot of the bubble size evolution in figure 2.2(c), where the time axis is normalized with  $\tau_g$ . In this form, all cases approximately collapse onto a single curve that is in good agreement with the 1/2 power law.

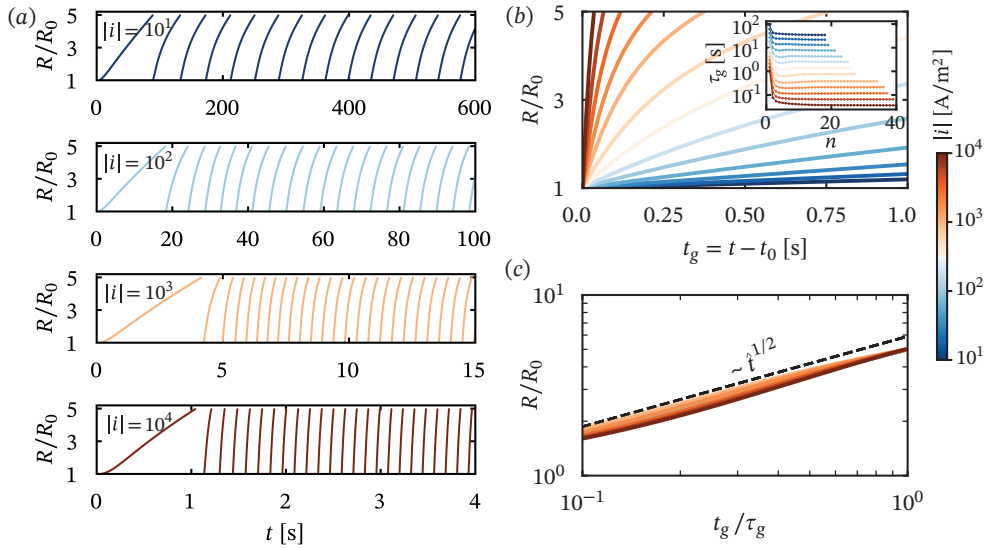


Figure 2.2: (a) Radius of the successively growing bubbles as a function of time for current densities  $|i| = 10^1, 10^2, 10^3$  and  $10^4$  A/m<sup>2</sup>. The radius has been normalized with the initial size of the bubble used for the simulations,  $R_0 = 50 \mu\text{m}$ . (b) Temporal evolution of the bubble radius at statistically steady-state for each current density in the range of  $10^1 < |i| < 10^4$  A/m<sup>2</sup>. The magnitude of the current density is illustrated with the colormap.  $t_0$  is the start of the bubble life-time in each case and hence  $t_g = t - t_0$  is the bubble age. The inset shows the bubble growth time,  $\tau_g$ , for the  $n^{\text{th}}$  bubble. (c) double-logarithmic plot of the bubble evolution curve for all the current densities. Time axis has been normalized with the growth time in the steady state as shown in the inset of panel (b).

Next, we look into the mass transfer rate at the electrode by tracking the spatially averaged concentrations on the electrode surface in time, as shown in figures 2.3(a) and 2.3(b) for  $H_2$  and  $H_2SO_4$ , respectively. As the reaction proceeds, the hydrogen concentration increases in time in contrast to the electrolyte concentration, which is depleted at the electrode. For the one-dimensional pure diffusion problem in the absence of the bubbles (diffusion in a semi-infinite medium with constant flux on the boundary) the analytical solution gives the time evolution of the cathodic concentrations,  $C_{j,e}^*$  as [85]

$$\hat{C}_{j,e}^*(t) - C_{j,0} = 2J_j \sqrt{\frac{t}{\pi D_j}}, \quad (2.20)$$

which has been provided for comparison at each current density in the figure 2.3(a) and 2.3(b). Small differences between this solution and the simulation results are related to the presence of the adhering bubble on the electrode and the inactive area underneath it, which alters the local concentrations slightly. Major deviations from the analytical solution occur after the departure of the first bubble, which leads to significantly enhanced mixing. As a result, fresh electrolyte is transported to the electrode replacing the gas-enriched and electrolyte-depleted solution there. Eventually, the system reaches an equilibrium in which the reaction and transport rates are balanced, such that the cycle-averaged concentrations remain constant in time.

A comparison of the behaviour for different current densities  $i$  is best done using the transient Sherwood numbers (2.17) plotted in figures 2.3(c) and 2.3(d) for  $H_2$  and  $H_2SO_4$ , respectively. Prior to the first bubble departure from the electrode surface, time-dependent Sherwood numbers collapse to a single curve regardless of the current density, as do those pertaining to the analytical solution of the pure diffusion problem. The bifurcation from the main trend happens after the detachment of the first bubble, i.e. transition to the convection, which takes place earlier at higher current density due to the higher oversaturation of the dissolved gas in the electrode boundary layer and faster bubble growth. Once the system is at equilibrium and the bubble generation rate no longer changes, the Sherwood numbers also approach an equilibrium value. Small oscillations around this value occur within each bubble cycle (see insets for the highest current density). For these, the minimums of  $\hat{Sh}_{j,e}$  correspond to the detachment times after which the Sherwood numbers immediately increase and the maximums are the instants when the bubble lifetime starts followed by a slow decrease during the growth time. Furthermore, due to the higher frequency of bubble generation and hence stronger mixing in the electrolyte, the effective mass transfer rate at the electrode, reflected in the values of  $\hat{Sh}_{j,e}$  in

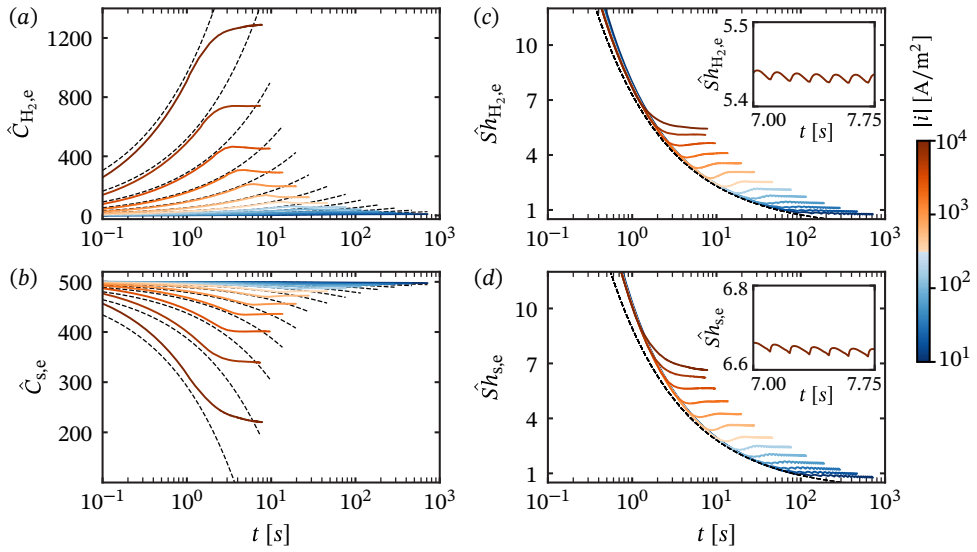


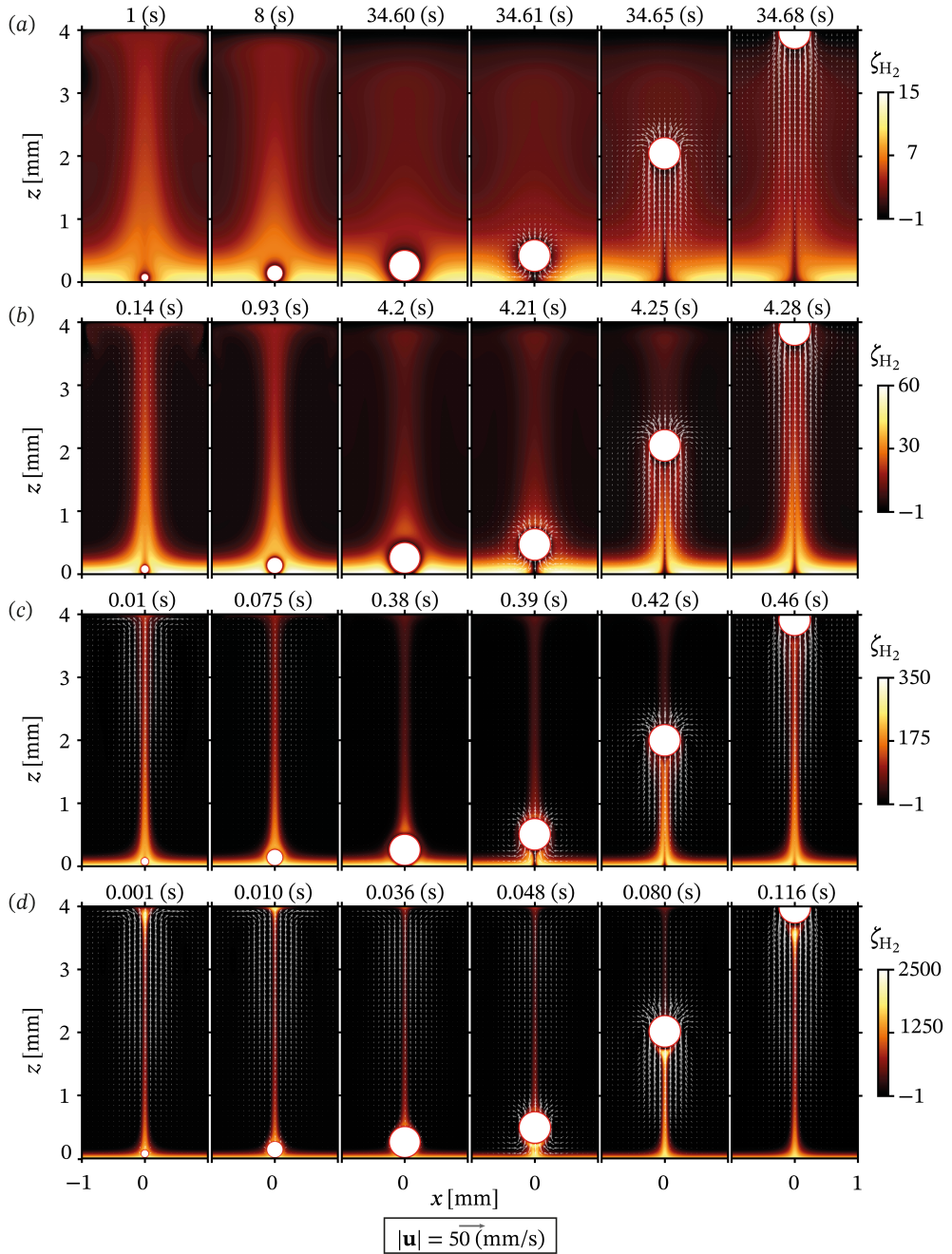
Figure 2.3: Temporal evolution of hydrogen (a) and electrolyte (b) averaged concentrations at the electrode surface for bubble departure diameter of  $d_b = 0.5$  mm and spacing of  $S = 2$  mm for all the investigated current densities. Broken black lines represent the solution of the pure diffusion problem in a semi-infinite medium with constant flux condition at the boundary, calculated using (2.20). Corresponding Sherwood numbers of simulations and pure-diffusion problem for hydrogen (c) and electrolyte (d) transport, computed based on (2.17). Insets in panels (c) and (d) show a closer view of Sherwood variation for the highest current density in statistically steady state. Current density at each case is distinguished using the colormap whose range is shown in the colorbar.

equilibrium, is significantly enhanced at higher current densities.

In order to provide insights into flow structure and scalar distribution in the equilibrium state, figure 2.4 displays snapshots of the hydrogen supersaturation,  $\zeta_{\text{H}_2} = C_{\text{H}_2}/C_{\text{H}_2,\text{sat}} - 1$ , overlaid with velocity vectors at different stages of the bubble evolution and for varying current densities. For the case with  $|i| = 10^3 \text{ A/m}^2$ , corresponding plots for the electrolyte concentration distribution are provided in figure 2.5. At this current density, a maximum electrolyte depletion of  $\approx 15\%$  occurs at the electrode and even in the most extreme case with  $|i| = 10^4 \text{ A/m}^2$ , this value does not exceed  $\approx 70\%$ , meaning that the electrolyte concentration remains finite in all cases even though the diffusion limited current density,  $|i|_{\text{diff}} = n_e F D_s C_{s,0} / H = 59.7 \text{ A/m}^2$ , is exceeded significantly. The associated transport enhancement is due to a large-scale convective pattern that is established during the rise stage, with an up-draught stream in bubble column, downwelling flow along the (periodic) side-walls, and wall-parallel flow close to the electrode. At low current density (figure 2.4(a)), the bubble driving is highly intermittent as the convective motion dissipates during the long growth period. However, as the latter becomes shorter for larger  $i$  (figures 2.4(b) and 2.4(c)), the flow becomes more and more continuous and a strong circulation is visible throughout the entire bubble cycle at  $|i| = 10^4 \text{ A/m}^2$  in figure 2.4(d). The convective pattern counteracts the penetration of the electrode boundary layer into the bulk by advecting the fresh electrolyte towards the electrode. This effect is stronger at higher currents due to the higher frequency of bubble formation driving a stronger flow. This can be also appreciated from figure 2.6(a) and 2.6(b), which compares the vertical profiles of normalized  $\text{H}_2$  and  $\text{H}_2\text{SO}_4$  at location halfway between adjacent bubbles, where an appreciable drop in the electrode boundary layer thickness with increasing current density is observed, consistent with an enhanced mass transport.

---

Figure 2.4 (following page): Snapshots of the hydrogen and velocity distributions in the equilibrium state at different stages of the bubble lifetime for current densities of (a)  $10^1$ , (b)  $10^2$ , (c)  $10^3$  and (d)  $10^4 \text{ A/m}^2$ . Bubble break-off diameter is  $d_b = 0.5 \text{ mm}$  and spacing is set at  $S = 2 \text{ mm}$ . In all cases, the first three panels cover the bubble growth and the last three the bubble rise time. The supersaturation level,  $\zeta_{\text{H}_2}$ , is shown using the colorbar. The superimposed vectors represent the induced velocity field by the growth and rise of the bubbles in the electrolyte. The velocity scale provided at the right of the figure applies to all panels.



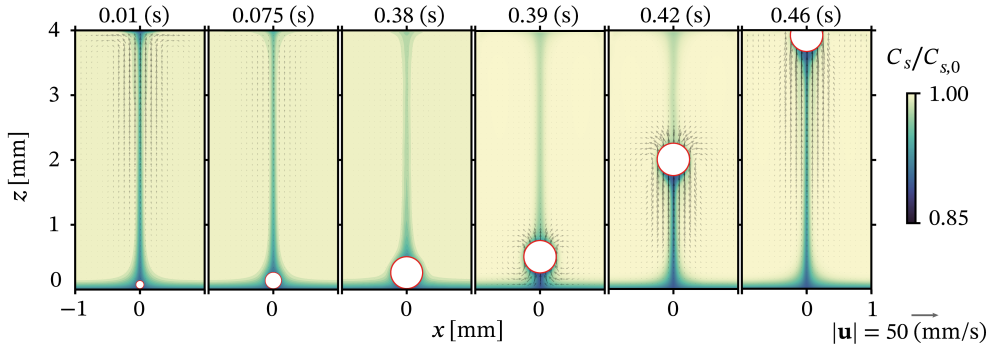


Figure 2.5: Snapshots of the electrolyte distribution for the case ( $|i| = 10^3 \text{ A/m}^2$ ) shown in figure 2.4(c).

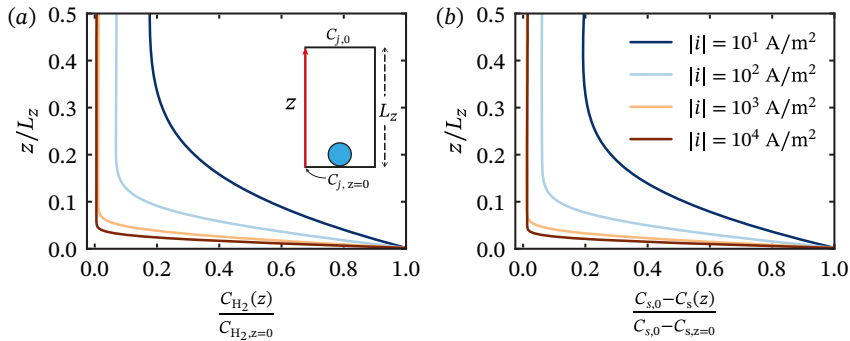


Figure 2.6: Vertical profiles of normalized hydrogen (a) and electrolyte (b) concentration half-way between adjacent bubbles (see the sketch in panel (a)) at the instant of bubble break-off. The profiles are captured at statistically steady state for different current densities.

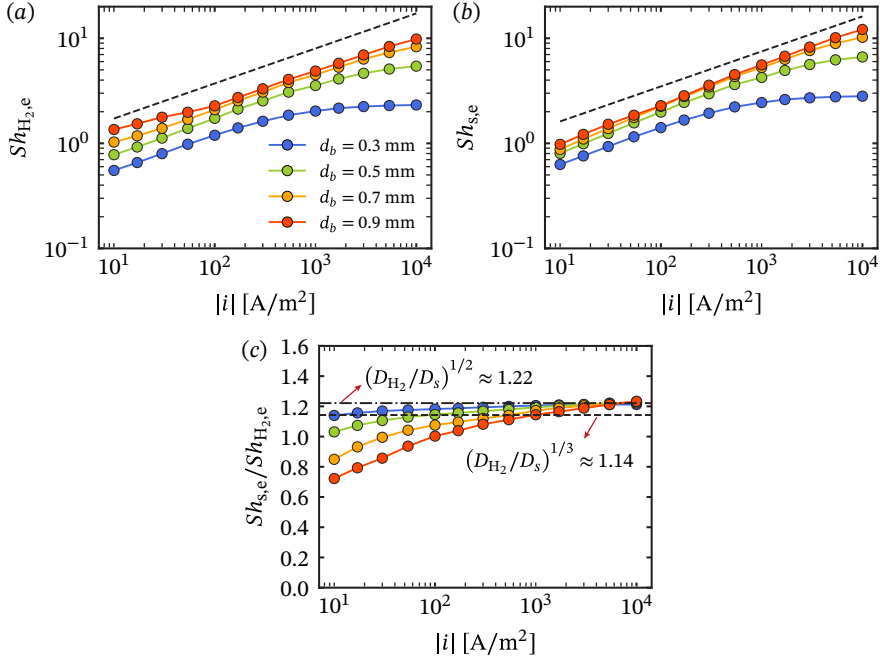


Figure 2.7: Sherwood number of (a) hydrogen and (b) electrolyte transport averaged over an entire bubble lifetime in the statistically steady state, as a function of current density for different bubble break-off diameter,  $d_b$ . The broken lines indicate the power law relation  $Sh_j \sim i^{1/3}$  for reference. (c) Ratio of electrolyte to hydrogen Sherwood numbers versus the current density at different bubble diameters. Dashed and dashed-dotted lines correspond to  $(D_{H_2}/D_s)^{1/3}$  and  $(D_{H_2}/D_s)^{1/2}$ , respectively, for comparison.

### 2.3.1 Current dependence of the Sherwood number and bubble size effect

Next, we consider the current dependence of the Sherwood numbers of hydrogen and electrolyte transport, averaged over an entire bubble lifetime in the statistically steady state, which are plotted in figure 2.7(a,b), respectively. Apart from the case with  $d_b = 0.5$  mm considered so far, these figures also include results for other bubble departure diameters. The trend of increasing  $Sh_{j,e}$  with increasing  $i$ , which was already evident in figures 2.3(c,d) for  $d_b = 0.5$  mm, is consistently observed for all these cases. The current dependence approximates a power law scaling of  $Sh_{j,e} \sim i^{1/3}$  especially for larger bubbles, but deviations occur for smaller bubbles at high current densities, where  $Sh_{j,e}$  increases significantly slower. It is further

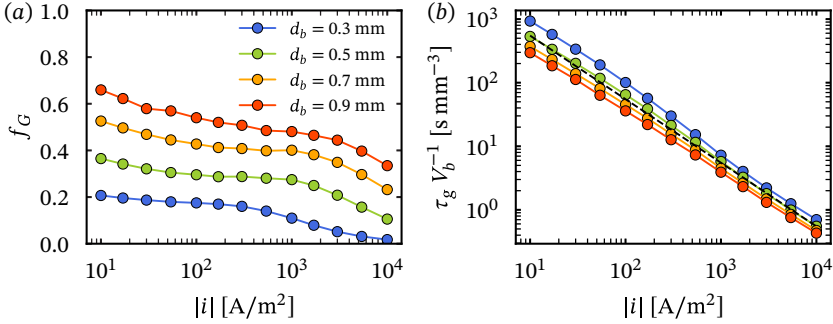


Figure 2.8: (a) Gas-evolution efficiency,  $f_G$  as a function of current density for different bubble break-off diameter,  $d_b$ . (b) Bubble residence time,  $\tau_g$ , compensated with bubble departure volume,  $V_b$ , as a function of current density for different values of  $d_b$ . The broken line indicates the power law of  $\tau_g \sim i^{-1}$ .

interesting to examine how  $Sh_{\text{H}_2,e}$  and  $Sh_{s,e}$  relate to each other, which we do by plotting the ratio  $Sh_{s,e}/Sh_{\text{H}_2,e}$  in figure 2.7(c). Given that  $Sh_{s,e}/Sh_{\text{H}_2,e} = \delta_{\text{H}_2}/\delta_s$ , one expects this ratio to yield a constant of either  $(D_{\text{H}_2}/D_s)^{1/2}$  (for diffusive transport) or  $(D_{\text{H}_2}/D_s)^{1/3}$  (for convection given that the Schmidt number  $Sc_j = D_j/\nu$  is large) for a single-phase flow. In the present simulations,  $D_{\text{H}_2}/D_s = 1.5$ , such that the resulting values (1.22 and 1.14) do not differ significantly. In our results in figure 2.7(c), a ratio of comparable magnitude is attained for the smallest bubbles and similar values are also approached for the cases with larger  $d_b$  at successively larger magnitudes of  $i$ . The deviation from the single-phase value is related to the fact that the electrolyte is only transported in solution while hydrogen is also carried inside the bubble. It is therefore most pronounced at low current densities and for large bubble sizes since for these cases the fraction of gas transported in the bubbles is largest as the plot of  $f_G$  in figure 2.8(a) confirms. The gas efficiency decreases significantly with decreasing bubble size, but is only a weak function of the current density especially for  $|i| \lesssim 10^3 \text{ A/m}^2$ . From gas-evolution efficiency relation, (2.19), it is deduced that  $\tau_g \sim V_b (f_G i)^{-1}$ , considering a constant rise time ( $\tau_c$ ) for the bubbles with the same size. Given the weak dependence of  $f_G$  on  $i$ , the scaling of  $\tau_g/V_b \sim i^{-1}$  holds reasonably well for all the cases shown here as can be seen from figure 2.8(b).

### 2.3.2 Effect of bubble spacing

Changing the bubble departure size, as was done in § 2.3.1, has multiple effects since it affects bubble growth times and the flow, but also alters the effective bubble coverage  $\theta$ . To disentangle these, we now fix the departure diameter of the bubble at  $d_b = 0.5$  mm and vary the box size  $S$  to explore a range of  $0.02 \leq \Theta \leq 0.56$ . This resembles a change in the bubble population density, which in practice is tied to the current density and typically increases when  $i$  is increased [49, 158]. Taking the advantage of the numerical simulations, we can explore the effect of this parameter independently here.

Figures 2.9 and 2.10 offer insight into how changing  $\theta$  affects the mass transport processes at the electrode by showing snapshots of the distributions of  $\text{H}_2$  and  $\text{H}_2\text{SO}_4$ , respectively, taken in the instant of bubble detachment after the system has reached a steady state. Figure 2.9(a) displays data for  $\text{H}_2$  at the lowest current density investigated ( $|i| = 10^1$  A/m<sup>2</sup>). For this case, the boundary layers are thick due to the weak convective transport at low  $\theta$ . However, as the bubble coverage is increased, the amount of dissolved hydrogen decreases and almost all the produced gas is contained in the bubble at  $\theta = 0.56$ . This implies very efficient transport for  $\text{H}_2$  via the gas phase, but since the detachment frequency is low, the same does not hold for  $\text{H}_2\text{SO}_4$  as can be seen from figure 2.10(a). Here, the depletion boundary layer is very thick with almost a linear gradient across the domain height. At the highest current density of  $|i| = 10^4$  A/m<sup>2</sup>, the significantly shorter detachment period leads to a much stronger driving of the flow. Convective transport therefore prevails even at high  $\theta$ , where  $\tau_c$  tends to increase as the amount of hydrogen produced per bubble decreases for smaller bubble spacings (see figure 2.12(c)). As a consequence, not only the hydrogen boundary layer (figure 2.9(b)) but also that for the electrolyte concentration (figure 2.10) remain thin even at  $\theta = 0.56$ .

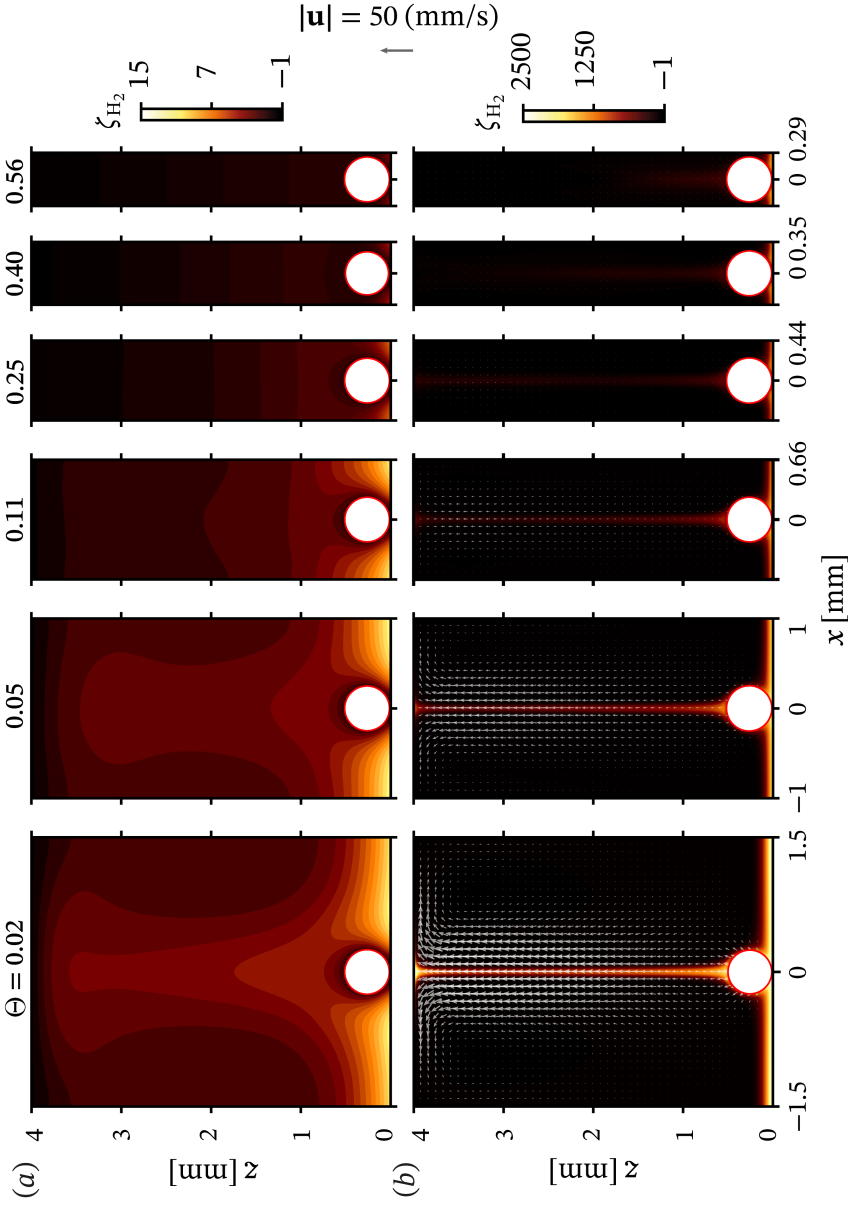


Figure 2.9: Snapshots of hydrogen supersaturation taken at the time of bubble detachment in the statistically steady state for  $|i| = 10^1$  (a) and  $|i| = 10^4$  A/m<sup>2</sup> (b). The fractional bubble coverage is increased from left to right within the range  $0.02 \leq \Theta \leq 0.56$  whose value is specified at top. The velocity scale applies to all panels.

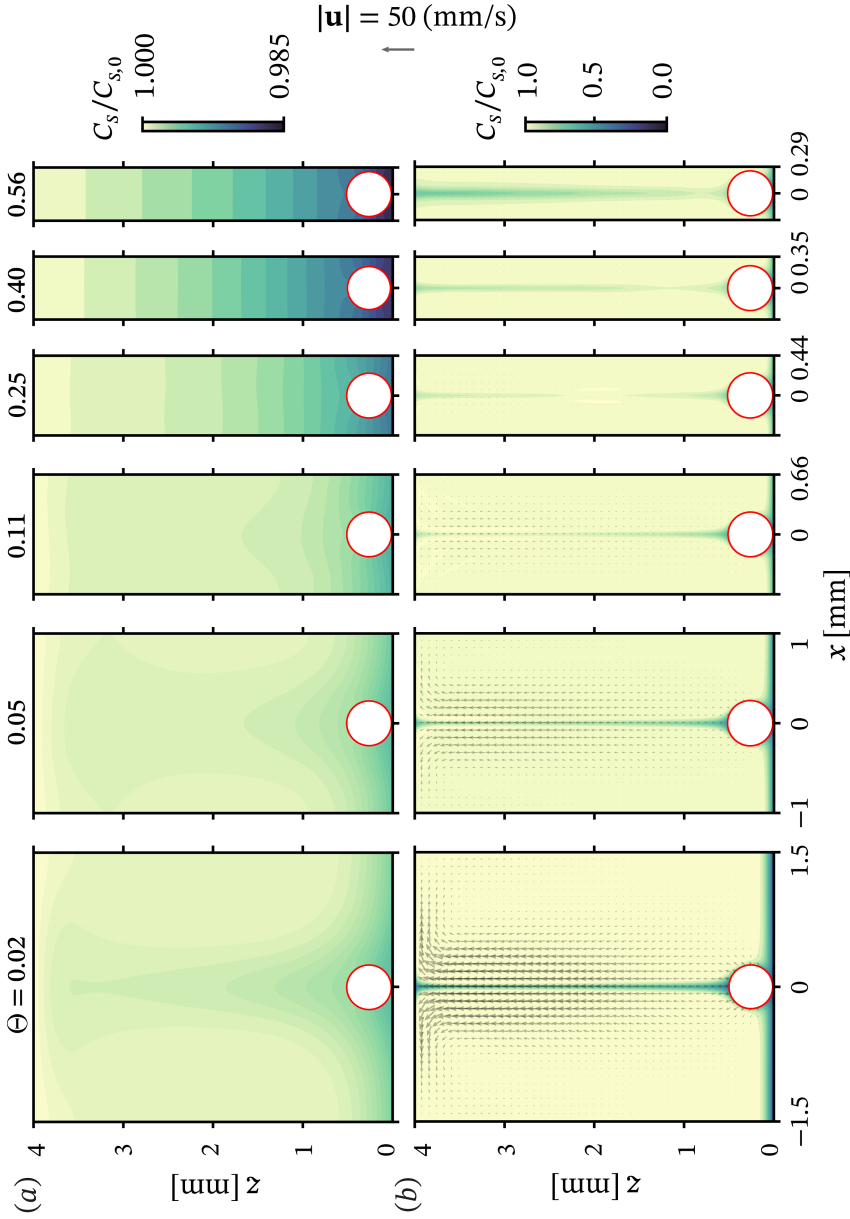


Figure 2.10: Snapshots of normalized  $\text{H}_2\text{SO}_4$  distribution at the time of bubble detachment in the statistically steady state for  $|i| = 10^1$  (a) and  $10^4 \text{ A/m}^2$  (b).

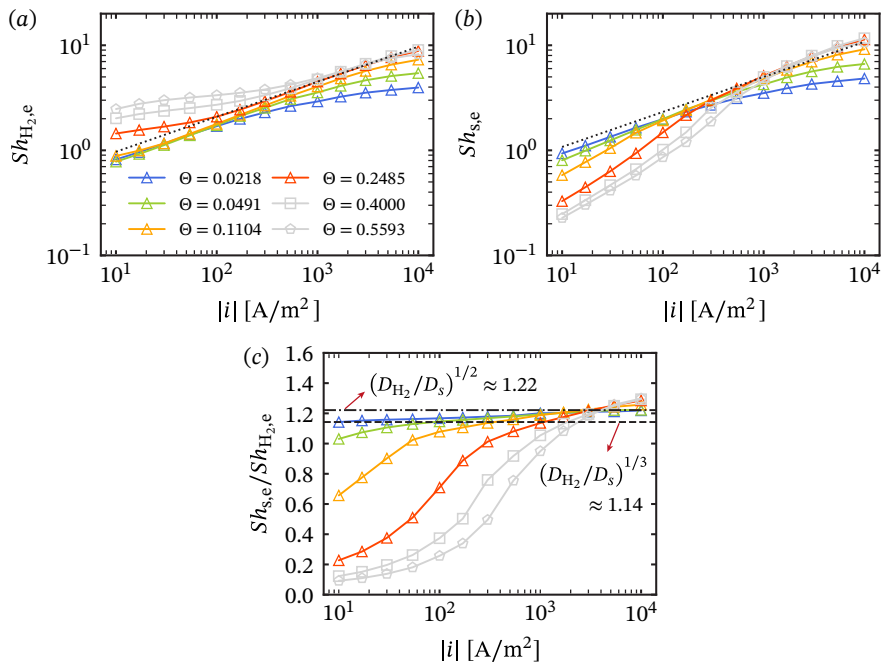


Figure 2.11: Sherwood number of (a) hydrogen and (b) electrolyte transport averaged over one bubble life-time in the statistically steady state, as a function of current density for different bubble spacings. The bubble departure diameter is fixed at  $d_b = 0.5$  mm and the range of fractional bubble coverage is  $0.02 \leq \Theta \leq 0.56$  as specified in the legend.

The trends observed in figures 2.9 and 2.10 are also reflected in the Sherwood numbers of  $H_2$  and  $H_2SO_4$  plotted in figure 2.11(a) and 2.11(b).  $Sh_{H_2,e}$  increases with  $\Theta$  throughout the whole range of current densities investigated. Again, the data generally approximate an  $i^{1/3}$  scaling albeit with significant deviations at low  $i$  and high  $\theta$  where the results significantly exceed this trend. Additionally,  $Sh_{H_2,e}$  falls below the  $1/3$ -scaling line for large current densities and low bubble coverage, which is in accordance with the trend observed in figure 2.7(a) for smaller  $d_b$  for which the value of  $\theta$  is also reduced. For these higher currents,  $Sh_{s,e}$  behaves similar to  $Sh_{H_2,e}$  and this is also reflected in the ratio  $Sh_{s,e}/Sh_{H_2,e}$  (figure 2.11(c)) being close to those expected for single-phase transport. Interestingly,  $Sh_{s,e}/Sh_{H_2,e}$  attains values even slightly larger than 1.22 for larger  $\theta$ . Presumably, this is caused by the lower  $H_2$  concentration in the dissolved phase, which dominates the transport for these cases. Remarkably, the  $\theta$  trend of  $Sh_{s,e}$  at current densities  $|i| \lesssim 10^3$   $A/m^2$  is opposite to that observed for the hydrogen transport in this regime with  $Sh_{s,e}$

decreasing for larger  $\theta$ . The ratio  $Sh_{s,e}/Sh_{H_2,e}$  drops to values as low as 0.1 for the most extreme case confirming that the gas is predominantly carried in bubbles whose rise triggers no significant convection as the detachment frequency is low.

Corresponding results for the gas evolution efficiency,  $f_G$ , are presented in figure 2.12(a). As expected,  $f_G$  increases significantly with fractional bubble coverage,  $\Theta$ . It approaches unity at lower currents and for the tightest spacings consistent with the observations in figures 2.9(a) and 2.11(c). Furthermore,  $f_G$ , generally decreases at higher current densities because the more frequent detachment events drive an increasingly stronger convection. As a result, the bulk of the gas is transported in dissolved form at  $|i| = 10^4$  A/m<sup>2</sup> even at the highest coverage of  $\theta = 0.56$ . When comparing our data to the empirical relation provided by Vogt 2011 [105], it is important to keep in mind that in practice increasing current density generally leads to higher  $\Theta$ . To identify realistic combinations of  $i$  and  $\Theta$  in the simulations, we compare the parameter space to the  $\Theta(i)$ -relation given by Vogt & Balzer (2005) [49] in figure 2.12(c). Simulations lying close to this line are marked with filled symbols in figures 2.12(a-c). If focusing on these points, our results for  $f_G$  in figure 2.12(a) approximately agree with the empirical relation for  $|i| \sim 10^3$ , but differences arise for higher and in particular for low current densities  $|i| \leq 10^2$  A/m<sup>2</sup>.

The results for  $f_G$  are replotted in figure 2.9(b), but this time as a function of  $\Theta$  since this is the practically more relevant form. It also allows for a comparison to the relations provided by Vogt (2011,2013,2015,2017) [77,105,158,159] based on theoretical considerations (see dashed gray and green lines in figure 2.9(b)). An obvious difference is that empirical relations are independent of  $i$ , whereas the data at any given  $\Theta$  exhibit a significant variation depending on the current density. This difference is significantly less prominent when considering only the ‘realistic’ cases, which are also reasonably well approximated by the expression of Vogt (2017) [159] at least up to  $\Theta \approx 0.3$ .

Figure 2.12(c) also includes results for the hydrogen supersaturation on the electrode in the steady state,  $\zeta_{H_2,e}$ , which are shown as colour contours interpolated between the simulation data points. Remarkably, the ‘realistic’ cases close to the relation of Vogt & Balzer (2005) [49] are seen to cover a very wide range of  $\zeta_{H_2,e} \approx 10$  up to very high values exceeding  $10^3$ . It should be noted, however, that for the latter cases, the boundary layers are very thin (see figure 2.9(b)), such that the effective supersaturation on the scale of the bubble will be significantly lower.

As a final point, we plot the bubble lifetime,  $\tau_c$ , in figure 2.9(c). The data is pre-multiplied with  $i$  to compensate for the  $1/i$ -dependence, which leads to variations in  $\tau_c$  over 4 orders of magnitude. For  $f_G = \text{const.}$ , all curves in the presented form would be expected to collapse onto a single line with linear dependence on  $\Theta$  based

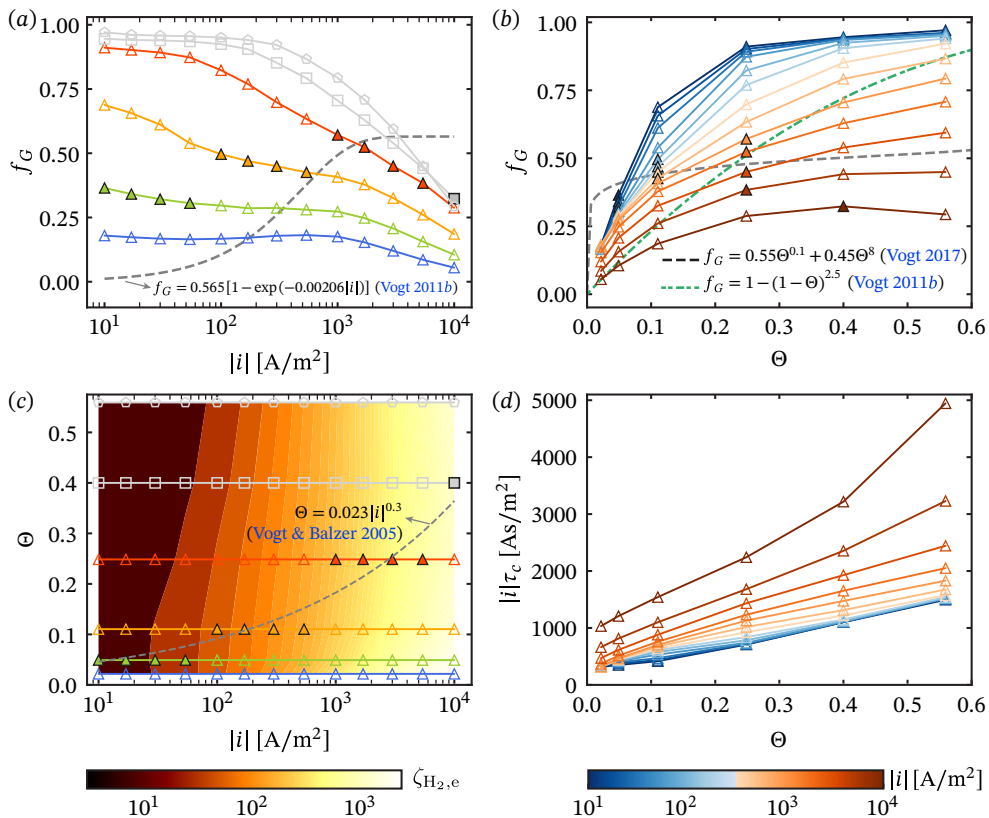


Figure 2.12: (a) Gas-evolution efficiency,  $f_G$ , as a function of current density for varying bubble spacing (specified in terms of the fractional bubble coverage,  $\Theta$ ). The bubble departure diameter has been fixed at  $d_b = 0.5$  mm. (b) Gas-evolution efficiency versus bubble coverage for varying current densities. (c) Hydrogen supersaturation on the electrode surface,  $\zeta_{H_2,e}$ , for all the simulation cases with varying current density and bubble spacing. (d) Bubble lifetime,  $\tau_c$ , pre-multiplied with current density as a function of bubble coverage for varying current densities. The relevant empirical relations by Vogt *et al.* are provided with broken lines in the panels. The filled markers in panels (a) and (b) show the closest data to the empirical relation  $\Theta = 0.023|i|^{0.3}$  [49] in panel (c), to highlight the more realistic cases.

on (2.19). While the linear trend is approximately preserved for all but the highest current density, the variations in  $f_G$  lead to an increase in  $i\tau_c$  with  $i$  that is most pronounced for the highest current densities.

### 2.3.3 Relating the electrode mass transfer to the effective buoyancy driving

The goal of this section is to provide scaling relations for the mass transport at the electrode based on the relevant physical transport mechanism. Our results so far have already highlighted the relevance of the convective flow driven by the departing bubbles. There is an analogy between the present configuration and single-phase buoyancy-driven convection in the sense that the detaching bubbles resemble the plumes of buoyant liquid in the latter case. Analyses based on boundary layer theory for convective heat transfer along vertical plates yield the power-law dependence on the Rayleigh number  $Ra^m$ , where the exponent  $m$  asymptotically varies from  $1/4$  for laminar flows to  $1/3$  for turbulent flows at high  $Ra$  [123]. The same power laws have empirically been shown to be valid for the convective heat transfer over horizontal plates and in particular for single-phase free-convective mass transfer over upward-facing horizontal electrodes by Wragg (1968) [124]. Beyond the laminar regime featuring an exponent of 0.25, these authors provided the relation

$$Sh = 0.16 (GrSc)^{0.33}, \quad (2.21)$$

for the mass transport in the turbulent regime, where the Grashof number  $Gr$  captures the buoyancy driving and Schmidt number is given by  $Sc = \nu/D$ . For two-phase buoyancy-driven convection,  $Gr$  can be defined to account for the effective buoyancy provided by the bubbles according to

$$Gr = \frac{gd_b^3}{\nu^2} \frac{\rho_L - \rho_e}{\rho_e} = \frac{gd_b^3}{\nu^2} \frac{\rho_L - [(1 - \epsilon)\rho_L + \epsilon\rho_G]}{(1 - \epsilon)\rho_L + \epsilon\rho_G}, \quad (2.22)$$

where  $\rho_L$  is the density of the bulk electrolyte,  $\rho_e$  is the mixture density at the electrode surface,  $\rho_G$  is the gas density and  $\epsilon$  is the gas volume fraction. Considering  $\rho_G \ll \rho_L$  yields the simplified expression

$$Gr = \frac{gd_b^3}{\nu^2} \frac{\epsilon}{1 - \epsilon}. \quad (2.23)$$

Based on the fact that a single bubble is contained in a box with base area  $A_e$  and height  $u_b\tau_c$ , where  $u_b$  denotes the bubble rise velocity,  $\epsilon$  can be related to the

volumetric flow rate of the gas,  $\dot{V}_G = V_b/\tau_c$ , by [112]

$$\epsilon = \frac{\dot{V}_G}{A_e u_b}. \quad (2.24)$$

For all cases investigated here we find that  $\epsilon \ll 1$ . Assuming Stokes drag for the bubbles yields the terminal velocity

$$u_b = \frac{1}{12} \frac{g d_b^2}{\nu} \frac{\rho_L - \rho_G}{\rho_L}, \quad (2.25)$$

which along with (2.19) leads to the final expression for  $Gr$  as

$$Gr = 12 f_G d_b \frac{-i}{n_e F} \frac{\mathcal{R}T_0}{P_0 \nu}. \quad (2.26)$$

The ratio of buoyancy to viscous forces therefore depends linearly on the input parameters  $d_b$ ,  $f_G$ , and in particular on  $i$ . The experimentally reported scaling of  $Sh \sim i^{1/3}$  [75, 103, 122, 160] is therefore equivalent to  $Sh \sim Gr^{1/3}$  provided that the dependence of  $d_b f_G$  on  $i$  remains relatively weak.

Next, we consider the dependence of the Sherwood numbers for the mass transport at the electrode as a function of  $Gr$ . Figure 2.13(a) presents a plot of  $Sh_{H_2,e}$  vs.  $Gr$  for all data presented in § 2.3.1 and § 2.3.2. In this form, the results very convincingly collapse onto a line indicating the power law of  $Sh_{H_2,e} \sim Gr^{1/3}$ , which validates adopting the single phase concept to the present configuration. Remarkably, the ‘turbulent’ scaling exponent of 1/3 applies to the full range of  $Gr$  studied here even though the flow is relatively weak and only intermittent in some cases (see figures 2.4 and 2.9). The data in figure 2.13(a) is well described by the fit

$$Sh_{H_2,e} = 1.0 (Gr Sc_{H_2})^{1/3}, \quad (2.27)$$

where the difference in the prefactor compared to the single-phase equivalent (2.21) is related to the multiphase nature of the present flow but also to the fact that a different length scale of bubble diameter is used here instead of lateral length scale of the electrode by Wrag (1968) [124]. The only significant deviation from (2.27) occurs for the ‘slow’ (in terms of  $\tau_c$ ) cases featuring a high  $f_G$ , for which the gas transport (carried almost exclusively inside the bubbles) is more efficient than buoyancy driving would suggest.

It is important to note that here  $Sh_{H_2,e}$  and therefore (2.27) accounts for both the transport of gaseous and dissolved hydrogen. We can focus on the dissolved transport specifically by multiplying  $Sh_{H_2,e}$  with  $(1 - f_G)$ , as is done in figure 2.13(b). For reference, a plot of  $f_G$  for all data vs.  $Gr$  is also included in figure 2.13(c). Consistent

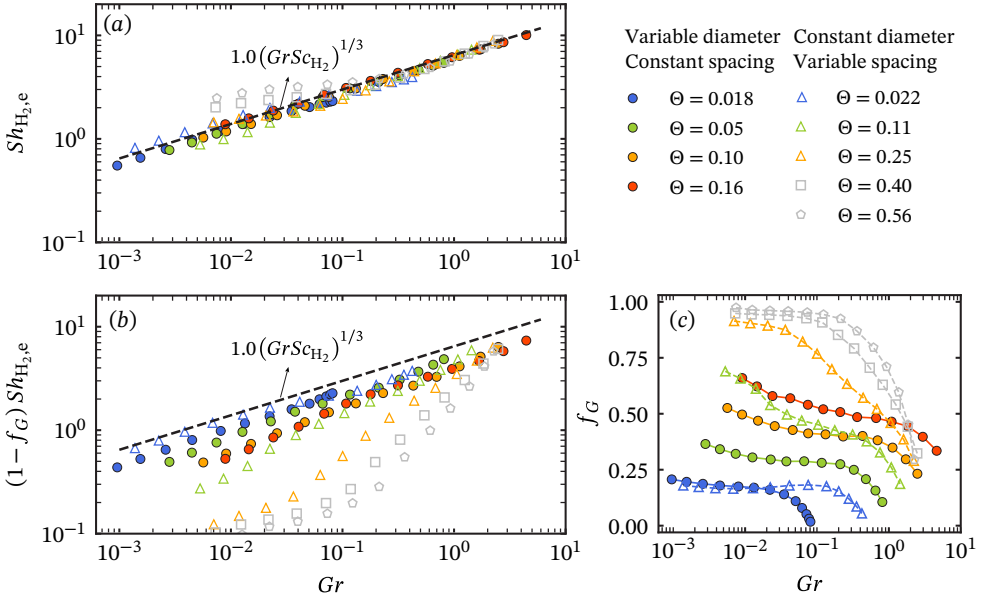


Figure 2.13: (a) Sherwood number of hydrogen transport,  $Sh_{H_2,e}$  (2.17), averaged over one bubble lifetime in the statistically steady state, versus  $Gr$  for all cases studied in this work. (b) Fractional Sherwood number of hydrogen transport as dissolved gas in the liquid phase,  $(1 - f_G)Sh_{H_2,e}$ . (c) Corresponding values of  $f_G$  vs.  $Gr$ .

with the fact that there is a wide spread in  $f_G$  at any given  $Gr$ , there is no collapse of the data in figure 2.13(b) underlining that the analogy between single and multiphase buoyancy driven flows is applicable at the level of the total transport only.

The transport of the electrolyte, which entirely acts as a passive scalar here, for the most part falls in line with the trends discussed for  $Sh_{H_2,e}$ . In particular,  $Sh_{s,e}$  primarily follows the power law of  $Sh_{s,e} \sim Gr^{1/3}$  even with the same prefactor when accounting for the difference in  $Sc$  as shown in figure 2.14(a). However, in accordance with figures 2.7(c) and 2.11(c),  $Sh_{s,e}$  drops below this scaling at low  $Gr$  and high  $\Theta$ . This means that electrolyte transport from the bulk to the electrode surface is limited when the bubbles highly cover the electrode and adhere to it for a long period during their lifetime. According to Vogt (1989,2012) [161,162] a factor contributing to the lower transport of the electrolyte is the blockage effect due to the presence of the bubble as can be seen from the snapshots in figure 2.10(a). To account for this, we divide  $Sh_{s,e}$  by the factor  $(1 - \Theta\tau_g/\tau_c)$  in figure

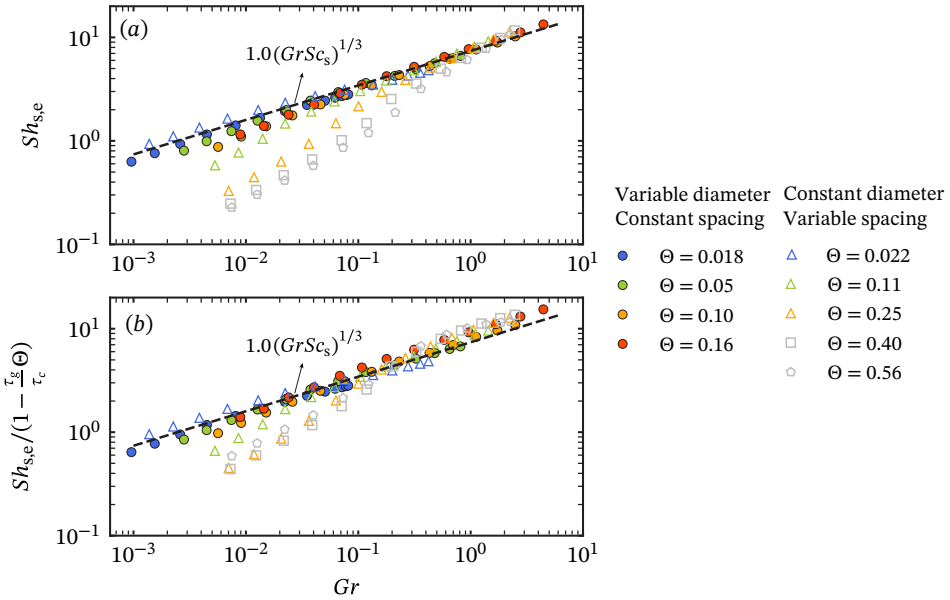


Figure 2.14: (a) Sherwood number of electrolyte transport,  $Sh_{s,e}$  (2.17), averaged over one bubble lifetime in the statistically steady state, versus  $Gr$  (2.22) for all cases studied in this work. (b)  $Sh_{s,e}$  compensated for net blockage effect,  $\Theta\tau_g/\tau_c$ , caused by bubbles adhering to the electrode surface in the residence time. The legend specifies cases simulated for different bubble diameter and spacing using the corresponding fractional bubble coverage of the electrode,  $\Theta$ . The broken lines indicates the fitted power law,  $Sh_{s,e} = 1.0(GrSc_s)^{1/3}$ , in which  $Sc_s = \nu/D_s$ .

2.14(b). Here,  $1 - \Theta$  is the fraction of the electrode not covered by the bubble and the additional timescale ratio accounts for the fact that the blockage applies only during the growth time  $\tau_g$ . Introducing this correction in fact reduces the deviations at lower  $Gr$  somewhat (but not fully) and the effect may therefore be relevant in this regime. However, the data for  $Gr \gtrsim 1$  is overcompensated. In summary, it therefore appears that the fact that no sustained convection exists at high bubble coverages if  $Gr$  is low plays the most important role leading to the lower electrolyte transport. This leads to limitation in the applicability of the single-phase analogy for this case. Nevertheless, it is worth noticing that the agreement with the  $1/3$  scaling law is much better for  $Sh_{s,e}$  (figure 2.14(a)) than for dissolved  $H_2$  (figure 2.13(b)) even though transport is exclusively within the electrolyte in both cases.

## 2.4 Mass transfer to the bubble

### 2.4.1 Bubble growth regimes

We now consider the dynamics of bubble growth and mass transfer into the bubble in more detail. The growth of the electrolytically generated gas bubbles can be described by the power law of  $R(t) = \mathcal{B}t^x$ . During the very initial stage, when the growth of the bubble is strongly influenced by the inertia forces from the liquid [19], an exponent of  $x = 1$  has been reported [163–166]. Later on, depending on whether the bubble growth is limited by the diffusive mass transfer of dissolved gas to the interface [156,157,163] or by the gas production rate in the reaction [57,135,166–168], exponents of  $x = 1/2$  or  $x = 1/3$  have been identified, respectively. Effective power laws in electrolysis may deviate from these values due to the interplay between diffusion and reaction rates.

Figure 2.15 presents different growth dynamics in the statistically steady state depending on current density and bubble coverage. Plotting the bubble radius versus the number of hydrogen moles,  $n_{\text{H}_2}$ , produced in the reaction from the beginning of bubble's lifetime,  $t_g$ , allows for easy comparison of the bubble growth dynamics over time for the full range of the current density. It is worth noting that  $n_{\text{H}_2} = J_{\text{H}_2} A_e t_g$  and therefore  $n_{\text{H}_2} \sim it_g$ . Power laws with exponent  $1/3$  and  $1/2$  have been added for comparison in figure 2.15 at different bubble coverages. Here, corrections are fitted to the prefactor  $\beta = (3\mathcal{R}T_0/4\pi R_0^3 P_0)^{1/3}$ , which represents the value for purely reaction-limited growth (i.e.  $f_G = 1$ ). For the lowest bubble coverage in figure 2.15(a), the growth dynamics are best described by the exponent of  $x = 1/2$  at all current densities. This indicates that the rate of mass transfer to the bubble is controlled by the diffusive transfer of dissolved hydrogen to the bubble interface for these cases. However, a switch from  $x = 1/2$  to  $1/3$  is appreciable as the current density increases at higher bubble coverages of  $\Theta = 0.25, 0.40$  presented in figure 2.15(b) and 2.15(c). At first sight, it may seem counter-intuitive that the reaction rate becomes more relevant as a limiting factor when it is increased. However, as discussed in the previous section, an increase in current density also significantly intensifies the convective transport which is then predominantly in the dissolved phase even at high  $\Theta$ . This reduces the boundary layer thickness and the amount of dissolved  $\text{H}_2$  (see figures 2.4 and 2.9), such that diffusive transport becomes increasingly less relevant compared to the faster reaction rate. Therefore, the exponent approaches  $x = 1/3$  and the prefactor approaches  $\beta$ , as observable from figure 2.15(b) and 2.15(c) where the bubble size evolution is better described by such power law at higher bubble coverages and current densities.

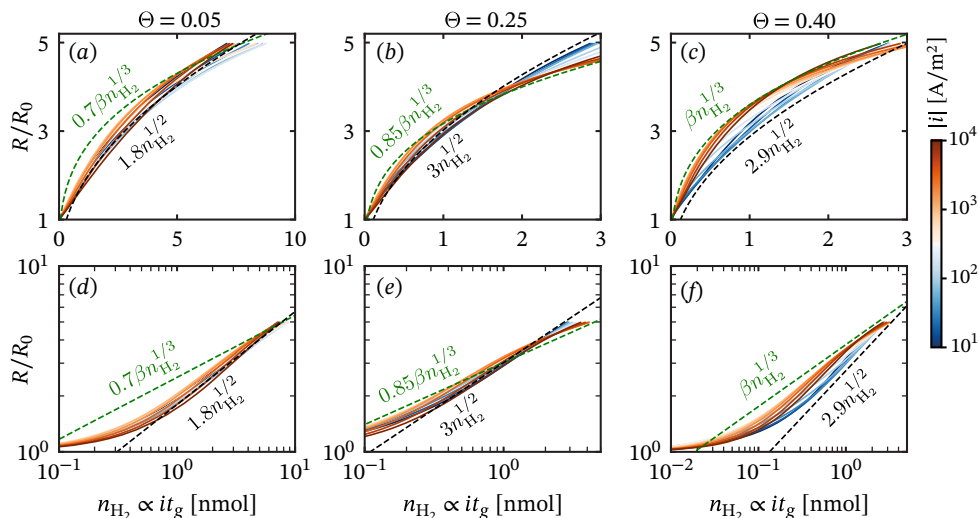


Figure 2.15: Temporal evolution of normalized bubble radius,  $R/R_0$ , versus the molar amount of hydrogen produced in the cathodic reaction,  $n_{\text{H}_2} = J_{\text{H}_2} A_e t_g$ , where  $t_g$  is the time elapsed from the start of bubble lifetime in the stationary steady state. The results are for all the investigated current densities (distinguished with the colormap) at bubble coverages of  $\Theta = 0.05$  (a) 0.25 (b) and 0.40 (c). The second row (d-e) shows the same data as (a-c) respectively with logarithmic scaling. The green and black broken lines show the power laws with exponent of  $1/3$  and  $1/2$ , respectively. Prefactors for  $1/3$  power law are adjusted relative to the growth constant purely reaction-limited bubble growth,  $\beta = 3.6 \text{ nmol}^{-1/3}$ .

## 2.4.2 Quantification of mass transport to the bubble

Figure 2.16(a) shows the transient behavior of  $Sh_{\text{H}_2,b}$  according to (2.18) over one bubble lifetime in the statistically steady state for varying current densities. Since bubble growth is neglected during the rise stage (see § 2.2.2 for further details)  $Sh_{\text{H}_2,b}$  becomes equal to zero after the bubble break-off from the electrode surface. In figure 2.16(a), it can be observed that at low current densities, an equilibrated mass transfer rate to the bubble is established towards the end of bubble residence time. This is evident from nearly constant values of  $Sh_{\text{H}_2,b}$  at late stages of the growth phase, for current densities  $|i| < 10^3 \text{ A/m}^2$ . In contrast, at higher current densities,  $Sh_{\text{H}_2,b}$  remains in a transient all the way until the departure of the bubble. To study the mass transport to the bubble, the instantaneous  $Sh_{\text{H}_2,b}$ , is averaged over the bubble residence time,  $\tau_g$ . The corresponding results for the data presented in figure 2.16(a) are shown in figure 2.16(b) and indicate an increase of  $Sh_{\text{H}_2,b}$  with increasing current density.

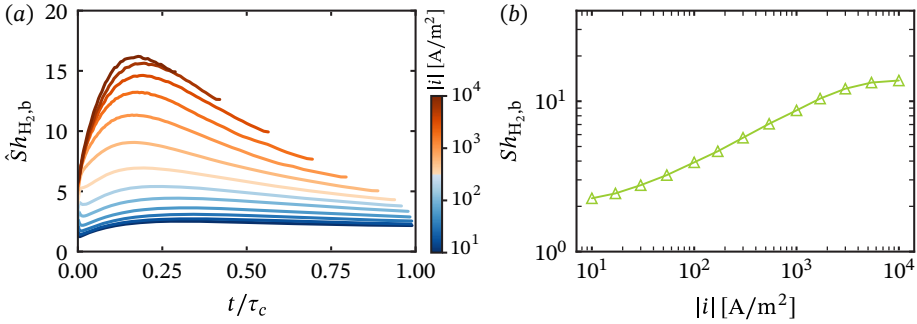


Figure 2.16: (a) Temporal evolution of the Sherwood number for the bubble,  $\dot{Sh}_{H_2,b}$  (2.18), during the entire bubble lifetime,  $\tau_c$ , in the statistically steady state and across the entire range of current density distinguished using the colormap. The data correspond to the case with bubble departure diameter of  $d_b = 0.5$  mm and a bubble spacing of  $S = 2$  mm, which leads to bubble coverage of  $\Theta = 0.1104$ . (b) The corresponding averaged Sherwood number of the bubble,  $Sh_{H_2,b}$ , over the residence time,  $\tau_g$ , plotted against the current density.

To gain a broader understanding of hydrogen transport to the bubble and facilitate its quantification, we have plotted  $Sh_{H_2,b}$  against current density in figure 2.17(a) for all the simulation cases, including those with variable bubble size or spacing. It is evident that at low current densities  $Sh_{H_2,b}$  is nearly constant and then it starts to ramp up with current density at all of the simulated cases. Furthermore, the normalized mass transfer to the bubble tends to decrease with bubble coverage as the lower values of  $Sh_{H_2,b}$  at higher  $\Theta$  suggests.

The current density is not directly related to the mass transfer into the bubble. In fact, the driving force for bubble growth is the concentration difference across the boundary layer developing at the bubble interface. The latter can be normalised with the gas concentration inside the bubble to yield the Jakob number,  $Ja$  [76, 155, 168]

$$Ja = \frac{M_G}{\rho_G} \Delta C = \frac{\mathcal{R}T_0}{P_0} (C_{H_2,e} - C_{H_2,sat}), \quad (2.28)$$

where  $M_G$  is hydrogen molar mass and  $C_{H_2,e}$  is employed to estimate the concentration difference  $\Delta C$  across the bubble boundary layer. At low  $Ja$  radial convection is negligible, such that  $Sh_{H_2,b}$  remains constant. At moderate ( $Ja \approx 1$ ) values and beyond, theoretical considerations predict that the bubble Sherwood number becomes dependent on  $Ja$  as the only parameter [76, 156, 157, 168]. However, the plot of  $Sh_{H_2,b}$  vs  $Ja$  for our results in figure 2.17(b) fails to collapse all the data onto a single curve. The reason for this is that theoretical derivations do not account for the confinement

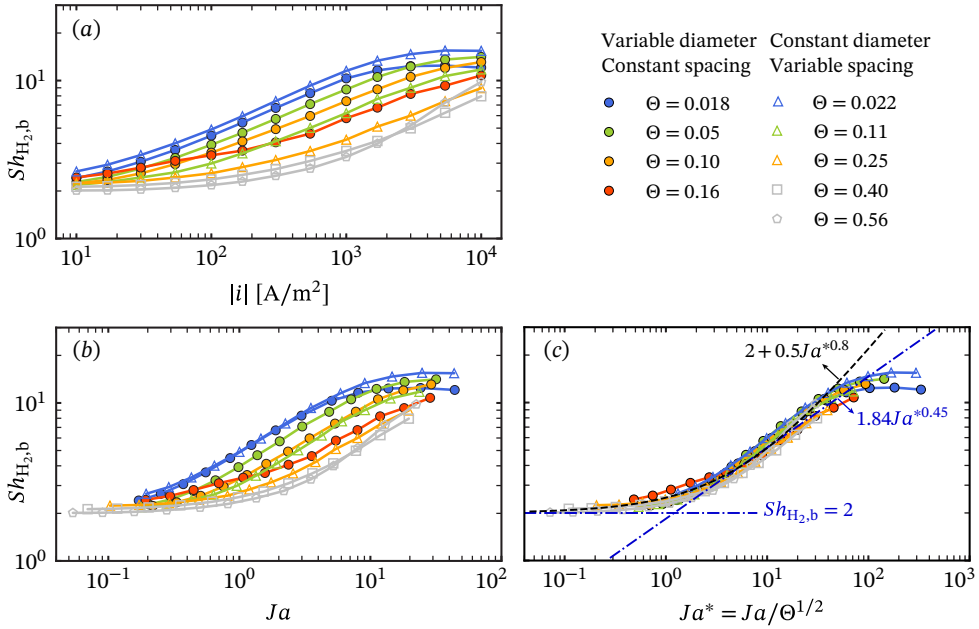


Figure 2.17: (a) Sherwood number of hydrogen transport to the bubble,  $Sh_{H_2,b}$ , averaged over bubble residence time,  $\tau_g$ , in the statistically steady state, as a function of current density for all the simulation cases with varying bubble size or spacing. (b)  $Sh_{H_2,b}$  versus Jakob number,  $Ja$ , computed according to (2.28). (c)  $Sh_{H_2,b}$  versus  $Ja^*$ , i.e., the Jakob number corrected with  $\Theta^{0.5} \approx d_b/S$  to account for the interference of mass transfer boundary layer on bubbles with each other. Approximate fit to the data and asymptotes have been shown with black and blue broken lines respectively. The legend specifies cases simulated for different bubble diameter,  $d_b$ , and spacing,  $S$ , using the corresponding fractional bubble coverage of the electrode,  $\Theta$ .

and assume a bubble in an infinitely large medium. However, especially for large  $\Theta$  the growing bubbles interact and thereby enhance the effect of radial convection. This interaction becomes more prominent the smaller the bubble spacing  $S$  is relative to the bubble diameter  $d_b$ . It therefore seems useful to define a compensated Jakob number which additionally depends on the ratio  $\Theta^{1/2} \approx d_b/S$ . Figure 2.17(c) reports the results of  $Sh_{H_2,b}$  versus compensated Jakob number,  $Ja^* = Ja/\Theta^{1/2}$ , in which a reasonable collapse of the data has been achieved. An approximated fitting to the data has been performed and shown with the black broken line in figure 2.17(c) which follows

$$Sh_{H_2,b} = 2 + 0.5Ja^{*0.8}. \quad (2.29)$$

It is worth noting that for very low values of bubble coverage, particularly at  $\Theta = 0.018$  and  $0.022$ , once again a nearly constant  $Sh_{H_2,b}$  can be observed towards the upper limit of  $Ja^*$  (as shown in figure 2.17(c)) where deviation from (2.29) occurs. This is related to the very short residence time of the bubble at high current densities for these cases. As seen in transient  $Sh_{H_2,b}$  in figure 2.16(a), as the current density increases, the bubble departs from the electrode at increasingly earlier times before an equilibrated mass transfer to the bubble can be established. This leads to nearly constant averaged  $Sh_{H_2,b}$  for such cases in figure 2.17(c), where a deviation from (2.29) occurs.

The relation (2.29) for the mass transfer to the bubble is consistent with the classical theories of Epstein & Plesset (1950) [156] and Scriven (1959) [157] for bubble growth in an infinitely large and uniformly supersaturated solution. The problem was later modified by Verhaart *et al.* (1980) [168] to account for bubble growth over electrodes with non-uniform supersaturation around the bubble. The theories show a constant bubble Sherwood number of  $Sh_{H_2,b} = 2$  for small values of Jakob number,  $Ja \rightarrow 0$ . Such condition is maintained in our simulations for high bubble coverages and low current densities where the concentration variation within the boundary layer is relatively low. The functional form used to represent the increase of  $Sh_{H_2,b}$  for larger  $Ja^*$  in (2.29) follows that suggested by Vogt 2011 [76] to approximate the exact solution of Verhaart *et al.* (1980) [168].

It is useful to reformulate the definition of the Jakob number in terms of the Peclet number of mass transfer at the electrode,  $Pe^*$  (defined as the ratio of reaction to diffusion rates), and  $Sh_{H_2,e}$ , as

$$Ja^* = \frac{Pe^*}{\Theta^{1/2} Sh_{H_2,e}}, \quad \text{with } Pe^* = \frac{-i \mathcal{R} T_0}{2F P_0} \frac{d_b}{D_{H_2}}. \quad (2.30)$$

Substituting the empirical fit (2.27) for  $Sh_{H_2,e}$  together with (2.29) leads to

$$Sh_{H_2,b} = 2 + 0.5 \left[ \frac{Pe^*}{\Theta^{1/2} (Gr Sc_{H_2})^{1/3}} \right]^{0.8}. \quad (2.31)$$

The Grashof number can be expressed as  $Gr = 12 f_G Pe^* / Sc_{H_2}$  (see (2.26)) such that the final mass transfer relation for the bubble is given by

$$Sh_{H_2,b} = 2 + 0.258 \left( \frac{Pe^{*2/3}}{\Theta^{1/2} f_G^{1/3}} \right)^{0.8}. \quad (2.32)$$

Since  $Pe^*$  and  $\Theta$  only depend on input parameters, the only previously unknown variable in (2.32), just as in (2.27), is  $f_G$ . In order to enable prediction solely based on input parameters, we will establish a suitable relation for  $f_G$ , in the next section.

## 2.5 Gas-evolution efficiency

In steady-state conditions, we can restate the definition of  $f_G$  in (2.19) in terms of the cycle averaged molar fluxes into the bubble and at the electrode according to

$$f_G = \frac{\int_0^{\tau_c} \int_{\partial V} D_{\text{H}_2} \nabla C_{\text{H}_2} \cdot \hat{\mathbf{n}}_b \, dA_b \, dt}{\int_0^{\tau_c} \int_{A_e} D_{\text{H}_2} \nabla C_{\text{H}_2} \cdot \hat{\mathbf{n}}_e \, dA_e \, dt} \sim \frac{D_{\text{H}_2} \frac{(C_{\text{H}_2,e} - C_{\text{H}_2,\text{sat}})}{\delta_b} d_b^2}{D_{\text{H}_2} \frac{(C_{\text{H}_2,e} - C_{\text{H}_2,0})}{\delta_e} A_e}, \quad (2.33)$$

where  $\delta_b$  and  $\delta_e$  are the boundary layer thickness normal to the bubble interface and electrode surface, respectively. Using  $Sh_{\text{H}_2,b}^* \sim d_b/\delta_b$ ,  $Sh_{\text{H}_2,e} \sim d_b/\delta_e$ ,  $\Theta \sim d_b^2/A_e$  and noting that  $(C_{\text{H}_2,e} - C_{\text{H}_2,\text{sat}}) / (C_{\text{H}_2,e} - C_{\text{H}_2,0}) \approx 1$ , this leads to the expression

$$f_G = \alpha \Theta \frac{Sh_{\text{H}_2,b}^*}{Sh_{\text{H}_2,e}}, \quad (2.34)$$

where the prefactor  $\alpha$  is to be determined from the data. The difference between  $Sh_{\text{H}_2,b}$  and  $Sh_{\text{H}_2,b}^*$  is that the former is averaged over the bubble residence time,  $\tau_g$ , whereas the latter is averaged over the entire bubble lifetime,  $\tau_c$ , consistent with definition of  $f_G$  (2.19). Since bubble growth is disregarded during rise stage,  $Sh_{\text{H}_2,b}(t) = 0$  during this period such that the different definitions are related by  $Sh_{\text{H}_2,b}^* = (\tau_g/\tau_c) Sh_{\text{H}_2,b}$ .

Next,  $f_G$  for all of the cases simulated here is plotted as a function of the dimensionless group,  $\Theta Sh_{\text{H}_2,b}^* Sh_{\text{H}_2,e}^{-1}$ , in figure 2.18. All data collapse to a single line for  $\Theta Sh_{\text{H}_2,b}^* Sh_{\text{H}_2,e}^{-1} < 0.375$  consistent with (2.34) and the slope is obtained as  $\alpha = 2.65$  based on the linear fit indicated as dashed line in the figure. For  $\Theta Sh_{\text{H}_2,b}^* Sh_{\text{H}_2,e}^{-1} > 0.375$ , the gas-evolution efficiency approaches its upper limit  $f_G \rightarrow 1$  and the data level off close to this value.

Inserting  $Sh_{\text{H}_2,e}$  from (2.27) and  $Sh_{\text{H}_2,b}$  from (2.32) into (2.34) results in an implicit expression for  $f_G$  that cannot be solved explicitly (see Appendix 2.7.4). Instead, we resort to piecewise solutions for  $f_G$  by inserting the asymptotes of  $Sh_{\text{H}_2,b}$  indicated by dashed blue lines in figure 2.17(c), into (2.34). Doing so yields the explicit expressions

$$f_G = 1.877 \Theta^{3/4} P e^{*-1/4}, \quad \text{for } Ja^* \lesssim 1, \quad (2.35)$$

$$f_G = 1.295 \Theta^{0.522} P e^{*-0.0225}, \quad \text{for } Ja^* \gtrsim 1. \quad (2.36)$$

It should be noted that in the derivation of (2.35) and (2.36), we have taken  $Sh_{\text{H}_2,b} = Sh_{\text{H}_2,b}^*$  presuming that  $\tau_g/\tau_c \approx 1$ , i.e. the bubble rise time is negligible. This is valid

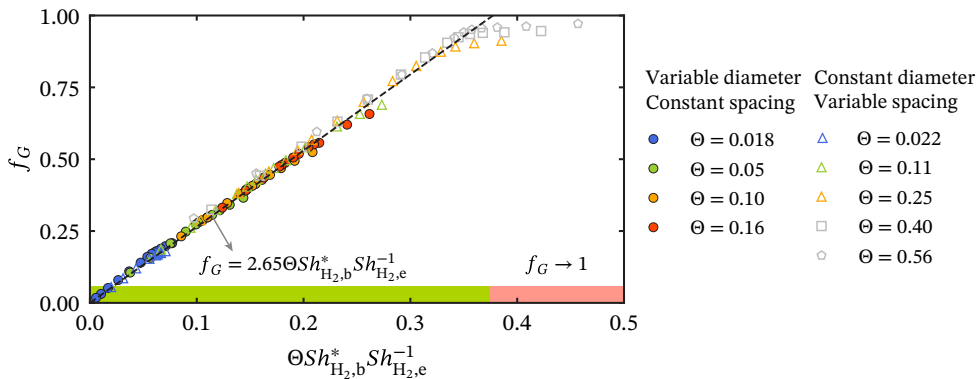


Figure 2.18: Gas-evolution efficiency,  $f_G$ , versus the dimensionless group  $\Theta Sh_{H_{2,b}}^* Sh_{H_{2,e}}^{-1}$ . The broken line shows the linear fit with slope  $\alpha = 2.65$  for  $\Theta Sh_{H_{2,b}}^* Sh_{H_{2,e}}^{-1} < 0.375$ , highlighted with green. For  $\Theta Sh_{H_{2,b}}^* Sh_{H_{2,e}}^{-1} > 0.375$ , highlighted with red, gas-evolution efficiency approaches its upper bound,  $f_G \rightarrow 1$ .

for our simulations at low and moderate current densities, whereas at high current densities  $\tau_g$  ultimately becomes even smaller than the bubble rise time,  $\tau_r$ , violating this assumption (e.g. see figure 2.4(d)). This can be considered an artifact of the simulations in which there is always a single bubble inside the computational box and the next bubble is initialized once the previous one has left the domain from the top boundary. Therefore the waiting time is equal to the bubble rise time,  $\tau_r$ , whereas experiments have revealed that the waiting time is extremely short especially at high current densities where the supersaturation level adjacent to the nucleation spot is very high [21, 53, 57]. Therefore, the waiting time is insignificant and it can be safely considered that  $Sh_{H_{2,b}}^* = Sh_{H_{2,b}}$  for practical applications.

For reference, we have included explicit relations for  $Sh_{H_{2,e}}$  and  $Sh_{H_{2,b}}$ , resulting from combining (2.35) and (2.36) with (2.27) and (2.32), in Appendix 2.7.4.

## 2.6 Discussion and conclusions

In this work, we set out to identify and quantify the governing mass transfer mechanism at gas-evolving electrodes by means of direct numerical simulations. Our work provides details on the mass transfer processes on a horizontal electrode subjected to successive growth and rise of electrolytically-generated gas bubbles. We employed immersed boundary method to enforce the mass and momentum interfacial conditions on the bubble surface, and therefore, to solve for its growth rate as

well as translational motion employing Fick's law and particle equations of motion, respectively. To elucidate the main effects, we varied the current density within the range of  $10 \leq |i| \leq 10^4$  A/m<sup>2</sup> for different prescribed bubble size and spacing, incorporated in fractional bubble coverage of the electrode surface,  $\Theta$ .

We quantified the cumulative hydrogen transport from the electrode surface (as dissolved gas and within the gas bubble) in figure 2.13 and that of electrolyte transport to the electrode in figure 2.14. By drawing an analogy to single-phase heat and mass transfer problems, the buoyancy-driven convection induced by consecutively departing bubbles from the electrode surface was identified as the governing mass transfer mechanism. This finding was corroborated by a unique power law of  $Sh_{j,e} = 1.0 (GrSc_j)^{1/3}$ , which was found to describe the hydrogen, and to a large part also the electrolyte, transport at the electrode. For the electrolyte, a factor of  $(1 - \Theta)$  to compensate for the surface blockage effect reduces, yet does not fully eliminate, deviations from the power law at low  $Gr$ . No such deviations occur at high  $Gr$ , at which also most of the gas transport is in the dissolved state.

Furthermore, we found a connection between bubble growth dynamics and hydrogen transport rate from the electrode. Specifically, as  $Gr$  ramps up with increasing current density and bubble coverage of the electrode, the growth dynamics of the bubble switch from diffusion-controlled,  $R = \mathcal{B}t^{1/2}$ , to reaction-controlled,  $R = \mathcal{B}t^{1/3}$ , regime (see figure 2.15). This transition was attributed to the high transport rate of hydrogen from electrode surface at large  $Gr$  which prevailed over the gas production rate thereby limiting the available oversaturation that would favour diffusive growth. Next, we quantified the hydrogen transport to the bubble as a function of the Jakob number  $Ja$ . Our data showed no collapse when plotted against the conventional definition of  $Ja$ . The agreement was much better, when additionally incorporating the ratio  $d_b/S \sim \Theta^{1/2}$  into the definition of a modified Jakob number,  $Ja^*$ , to account for the effect of neighbouring bubbles. With this modified definition, the resulting expression for mass transfer into the bubble is given by (2.32).

Finally, we established a semi-empirical relation between the dimensionless mass transfer rates at the electrode and bubble interface and the gas-evolution efficiency,  $f_G$ . Ultimately, this allowed us to provide explicit (i.e. depending on input parameters only) expressions for  $f_G$  given by (2.35) and (2.36) and consequently also for the other response parameters  $Sh_{H_2,e}$  and  $Sh_{H_2,b}$  (see Appendix 2.7.4). These findings can help quantify mass transfer rates in practical applications provided typical bubble sizes and spacing on the electrode can be quantified.

Our findings reveal different governing physics of mass transfer at gas-evolving electrodes than what was envisioned by Stephan & Vogt (1979), Vogt (2011) and

Vogt & Stephan (2015) [77, 102, 105], who attributed the rate-controlling mechanism of mass transfer to micro-processes induced by bubble growth and break-off from the electrode. As briefly introduced in § 2.1, these micro-processes originate from three different sources: pure diffusion of fresh electrolyte to the electrode surface in the small region previously occupied by the bubble, convective flow induced by the expanding boundary of the bubble, and wake-flow after its break-off from the electrode. These processes impact the mass transfer in a microarea surrounding the nucleation spot whose size declines in time due to the bubble growth. For pure-diffusion transport of the reactant to the electrode during bubble growth, the authors [77] modified the mass transfer relations established by Roušar & Cenzer (1975) [99]. To account for microconvection of bubble growth and break-off, the authors considered an analogy of the flow pattern around a growing bubble to lateral plug flow [102], which was later modified with a boundary layer flow [77]. This approach allowed them to employ the mass transfer relations developed for such flows over flat plate to quantify the averaged transport of reagent to the microarea within the time interval of bubble growth and break-off. The authors concluded that micro-processes in the small region surrounding the bubble were the rate-determining mechanism of mass transfer and prevailed over single-phase and two-phase free convection at moderate and high values of current density [105]. Our results are inconsistent with these considerations due to several reasons. The authors assumed that the space previously occupied by the bubble was fully replenished with fresh electrolyte immediately after bubble break-off, and hence they employed Cottrell's relationship to predict the pure-diffusion mass transfer at the microarea. While this assumption holds true to some extent for high current densities, it is violated at low currents where the electrode boundary layer is much larger than the bubble break-off diameter (the bubble is fully immersed in the boundary layer, see figure 2.4). In such cases, stirring the solution in a region that is already depleted of reactant fails to fully replace the bubble volume with fresh bulk electrolyte. Likewise, the employed analogy to plug/boundary-layer flow over flat plate is questionable because the predominantly wall-parallel advection of a depleted boundary layer caused by bubble growth does not affect the wall-normal mass transfer significantly. Consequently, we fail to observe enhanced mixing during growth periods in our simulations.

In contrast, our findings provide evidence that the flow pattern established by two-phase buoyancy-driven convection (see figure 2.4) is key in setting the mass transfer rate at the electrode. It is clearly visible from the  $\text{H}_2$  and  $\text{H}_2\text{SO}_4$  snapshots in figures 2.4 and figure 2.5 that the concentration fields are changed in accordance with the flow pattern induced by bubble motion; i.e., an up-drought in bubble

column, descent of the solution mixture between the bubbles and a roughly wall-parallel flow adjacent to the electrodes. Such flow pattern is analogous to those induced by plume emissions in single-phase free convection. In fact, the similarity of the mass transfer relations established in this work (2.27) to those of single-phase free convection [123,124] proves that two-phase buoyancy-driven convection of departing bubbles is the rate-controlling mechanism of mass transfer at gas-evolving electrodes. This is further consistent with experimental measurements by Janssen & Hoogland (1973) [75], Janssen (1978) [122] and Janssen & Barendrecht (1979) [103] where the thickness of boundary layer on hydrogen-evolving electrodes followed the same power law as (2.27) when the bubble coalescence did not happen frequently. In summary, it therefore does not appear necessary to account for micro-processes, such as bubble growth, specifically when considering mass transfer.

There remain some limitations that apply to this work. To avoid additional complications, we did not take into account the potential contribution of single-phase free convection, which arises from density gradients in the solution caused by concentration variations in the electrode and bubble boundary layers [25,28]. Single-phase free convection might be of some influence at low current densities, where the bubbles adhere to the electrode for long period of time and allow the density gradients in the electrode boundary layer to develop to a sufficient extent necessary for triggering the instabilities [169]. However, we found in the chapter 1 that these instabilities are suppressed for bubble spacing of less than  $\approx 2$  mm, which is the case for most of the simulation cases here except those with the least bubble coverage of the electrode. At higher values of the current density where the frequency of bubble generation is relatively high, the induced flow of departing bubbles is very likely to suppress the single-phase free convection by reducing the density gradients in the cell or prevails over it if both mechanisms coexist. Furthermore, the Marangoni convection arising from surface tension gradients along the interface due to the temperature increase or electrolyte depletion in bubbles proximity might play a role. Thermal Marangoni is mostly playing a role in electrolytically-generated gas bubbles on microelectrodes where the current density can easily surpass  $10^6$  A/m<sup>2</sup> in the bubble foot area and increase the temperature remarkably by ohmic heating [59,60,170,171]. However, thermal Marangoni is likely less of a factor in the present configuration, as our current density does not exceed  $10^4$  A/m<sup>2</sup>, which is not sufficient to increase the temperature considerably. However, solutal Marangoni as a result of electrolyte depletion [172] might play a role which needs further investigation in future works. Eventually, as our numerical solver treats the full 3-dimensional problem, we are able to extend this work to a set-up in which several bubbles are generated in a asymmetrical network of nucleation spots to

study the collective effects of bubbles and replicate a system which mimics the relevant physics more accurately for practical applications.

**Acknowledgments.** We thank Prof. Andrea Prosperetti for the fruitful discussions. We acknowledge PRACE for awarding us access to MareNostrum at Barcelona Supercomputing Center (BSC), Spain, and Irene at Trés Grand Centre de calcul du CEA (TGCC), France, under project No. 2021250115.

## 2.7 Appendix

### 2.7.1 Validation of bubble motion with IBM

As discussed in § 2.2.2, a remedy is required to solve for the bubble motion with IBM due to stability issues that arise at low gas to liquid density ratios. To mitigate this, the virtual mass approach by Schwarz *et al.* (2015) [142] is employed here and a virtual force,  $\mathbf{F}_v$  (2.13), is added to both sides of (2.25). To check the reliability of this method, we simulate the test case of Schwarz *et al.* (2015) [142] using our code. The ascending motion of a light particle with a density ratios of  $\Gamma = 0.5$  and 0.001 in a quiescent viscous fluid is considered. Such flows are characterized by the Galileo number defined as

$$Ga = \frac{\sqrt{|\Gamma - 1|} g d_b^3}{\nu}. \quad (2.37)$$

Additionally, the gravitational velocity and time scales read

$$u_G = \sqrt{|\Gamma - 1|} g d_b, \quad t_G = \sqrt{\frac{d_b}{|\Gamma - 1|} g} \quad (2.38)$$

respectively and are utilized as reference values. The related parameters considered here are  $Ga = 170$ ,  $g = \|\mathbf{g}\| = 10$ ,  $d_b = 1$  and  $\rho_L = 1$ . The size of the computational box is set to  $\mathbf{L} = (6.4, 6.4, 12.8) d_b$  and is discretized with  $\mathbf{N} = (256, 256, 512)$  cells in  $x, y$  and  $z$  directions, respectively. The sphere is initially at rest and released at  $\mathbf{x}_{b,0} = (3.2, 3.2, 0.6) d_b$ . Periodic boundary conditions are applied in all directions and time marching is performed with steps of  $\Delta t = 1 \times 10^{-3}$  to exactly replicate the test case in Schwarz *et al.* (2015) [142]. The simulation for  $\Gamma = 0.5$  is stable without modification of the original equation and is therefor run with  $C_v = 0$ . Stability for  $\Gamma = 0.001$  is ensured by setting  $C_v = 0.5$ . Figure 2.19(a) presents the results for the time-evolution of the particle rise velocity  $u_p$  along with the corresponding data

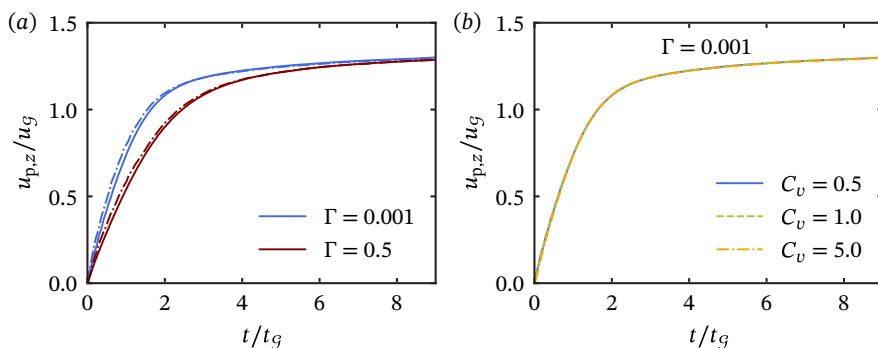


Figure 2.19: (a) Temporal evolution of normalized particle rise velocity for Galilei number  $Ga = 170$  at density ratios  $\Gamma = 0.001$  and  $0.5$ , obtained from present work (solid lines) and comparison to data from Schwarz *et al.* (2015) [142] (broken lines). Virtual mass coefficients of  $C_v = 0.5$  and  $0$  have respectively been used for density ratios  $\Gamma = 0.001$  and  $0.5$ . (b) Sensitivity of rise velocity to virtual mass coefficient for  $\Gamma = 0.001$ .

from Schwarz *et al.* (2015) [142], with which excellent agreement is observed. Furthermore, we have performed the simulations for  $\Gamma = 0.001$  using different values of  $C_v$  to check the sensitivity of results to the artificial virtual force. Figure 2.19(b) shows that the particle rise velocity is quite insensitive to virtual mass. Hence, we conclude that this method can safely be employed to simulate the rising motion of electrolytically-generated gas bubbles with  $\Gamma = 0.001$  in this work.

## 2.7.2 Grid-independence check

To ensure the accuracy of the simulations, a grid-independence check has been performed on the case presented in § 2.3 with  $d_b = 0.5$  mm and  $S = 2$  mm. The highest current density of  $|i| = 10^4$  A/m<sup>2</sup> featuring the thinnest boundary layer on the electrode (cf. figure 2.4) is selected for this purpose. Figure 2.20(a) and 2.20(b) show the time-evolution of H<sub>2</sub> and H<sub>2</sub>SO<sub>4</sub> Sherwood numbers on the electrode surface for three grids with increasing resolution confirming that the results are independent of the grid size in the investigated range. The base-grids are refined by a factor of two for H<sub>2</sub> using a multiple resolution strategy as explained in § 2.2.2. This strategy ensures the hydrogen conservation in the system by sufficiently resolving the boundary layer thickness on the bubble interface (see Appendix 2.7.3). Grid refinement is only applied for H<sub>2</sub> transport, as dissolved hydrogen and its diffusion into the bubble determine the bubble dynamics and hence the whole hydrodynamics and mass transfer in the system. Based on the results in figure 2.20,

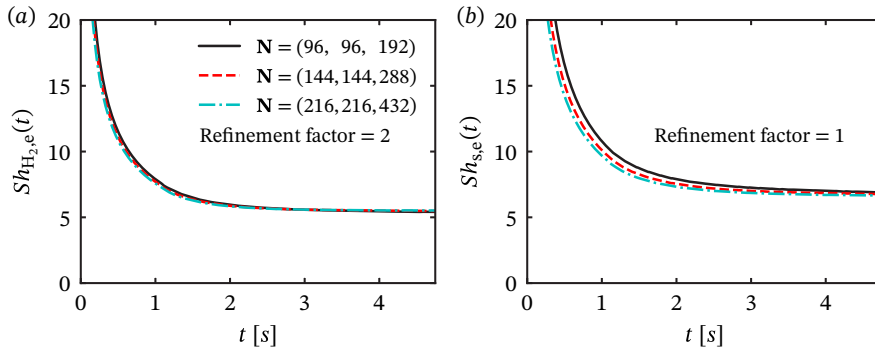


Figure 2.20: Grid independence check based on the temporal evolution of  $\text{H}_2$  (a) and  $\text{H}_2\text{SO}_4$  (b) Sherwood numbers on the electrode surface for the case presented in § 2.3, i.e.,  $d_b = 0.5$  mm and  $S = 2$  mm at the highest current density of  $|i| = 10^4$  A/m<sup>2</sup>. Base-grid sizes, introduced in panel (a), are refined by factor of 2 for  $\text{H}_2$  transport. Grid-independent results have been achieved for both species.

the base grid resolution of  $\mathbf{N} = (144, 144, 288)$  is selected for the reference case and grid sizes for other cases with varying lateral size of the computational box have been adjusted to keep the spatial resolution constant. This results in 36 grid cells across the bubble diameter if  $d_b = 0.5$  mm, whereas this value is 21 if  $d_b = 0.3$  mm.

### 2.7.3 Hydrogen conservation

It is crucial to assure that the fluxes of dissolved hydrogen into the bubble interface, yielding the bubble growth rate, are calculated accurately with IBM. To this end, we perform an analysis to check the conservation of hydrogen in the system. This requires that the rate of change of  $\text{H}_2$  moles dissolved in the bulk electrolyte should be balanced with the net of  $\text{H}_2$  interfacial fluxes. The latter include the  $\text{H}_2$  production rate on the electrode surface ( $J_{\text{H}_2,e}$ ), the desorption rate at the bubble interface ( $J_{\text{H}_2,b}$ ), and the outflux at the top boundary ( $J_{\text{H}_2,\text{top}}$ ). Figure 2.21 compares the net interfacial fluxes with the rate of change of  $\text{H}_2$  in solution during bubble growth. This analysis concerns the reference case presented in § 2.3 ( $d_b = 0.5$  mm and  $S = 2$  mm) in the statistically steady state. It is evidenced by figure 2.21 that our numerical scheme is conservative for hydrogen gas within the studied range of current density. However, higher current densities most likely demand finer spatial and temporal resolutions in order to capture the extremely thin mass boundary layers developed on the bubble and electrode interfaces.

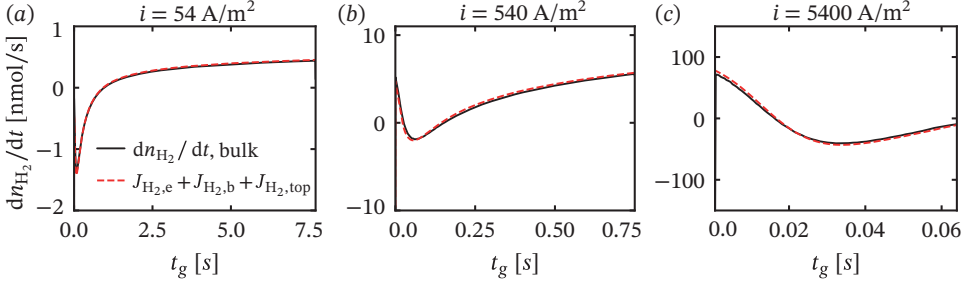


Figure 2.21: Hydrogen conservation check during the bubble residence time on the electrode at statistically steady state, performed for the case presented in § 2.3, i.e.,  $d_b = 0.5$  mm and  $S = 2$  mm at current densities  $|i| = 54$  (a) 540 (b) 5400 A/m<sup>2</sup>(c).  $t_g$  is the age of the bubble generated in the statistically steady state. Black solid lines are the rate of change of H<sub>2</sub> moles in the solution mixture. Red broken lines are the summation of H<sub>2</sub> production rate on the electrode ( $J_{H_2,e}$ ), desorption rate into the bubble ( $J_{H_2,b}$ ), and loss rate from the top boundary ( $J_{H_2,top}$ ).

## 2.7.4 Additional expressions

Implicit expression for  $f_G$ , after insertion of (2.27) and (2.32) into (2.34), reads

$$f_G = 2.65\Theta \frac{2 + 0.258 \left( \frac{Pe^{*2/3}}{\Theta^{1/2} f_G^{1/3}} \right)^{0.8}}{(12f_G Pe^*)^{1/3}}. \quad (2.39)$$

which only has a piecewise solution. Inserting the expression for  $f_G$  given by (2.35) and (2.36) into the fit of  $Sh_{H_2,e}$  given by (2.27) leads to an expression for  $Sh_{H_2,e}$  solely based on input parameters as

$$Sh_{H_2,e} = 2.83 (\Theta Pe^*)^{1/4}, \quad \text{for } Ja^* \lesssim 1, \quad (2.40)$$

$$Sh_{H_2,e} = 2.50\Theta^{0.174} Pe^{*0.326}, \quad \text{for } Ja^* \gtrsim 1. \quad (2.41)$$

Similarly, inserting (2.35) and (2.36) into (2.32) yields an expression for  $Sh_{H_2,b}$  based on input parameters as

$$Sh_{H_2,b} = 2 + 0.218 \left( \frac{Pe^*}{\Theta} \right)^{0.6}, \quad \text{for } Ja^* \lesssim 1, \quad (2.42)$$

$$Sh_{H_2,b} = 2 + 0.241 \left( \frac{Pe^*}{\Theta} \right)^{0.54}, \quad \text{for } Ja^* \gtrsim 1. \quad (2.43)$$

# 3

## Diffusive and convective dissolution of carbon dioxide in a vertical cylindrical cell <sup>◦</sup>

*The dissolution and subsequent mass transfer of carbon dioxide into liquid barriers play a vital role in many environmental and industrial applications. In this work, we study the downward dissolution and propagation dynamics of CO<sub>2</sub> into a vertical water barrier confined to a narrow vertical glass cylinder, using both experiments and direct numerical simulations. Initially, the dissolution of CO<sub>2</sub> results in the formation of a CO<sub>2</sub>-rich water layer, which is denser in comparison to pure water, at the top gas-liquid interface. Continued dissolution of CO<sub>2</sub> into the water barrier results in the layer becoming gravitationally unstable, leading to the onset of buoyancy driven convection and, consequently, the shedding of a buoyant plume. By adding sodium fluorescein, a pH-sensitive fluorophore, we directly visualise the dissolution and propagation of the CO<sub>2</sub> across the liquid barrier. Tracking the CO<sub>2</sub> front propagation in time results in the discovery of two distinct transport regimes, a purely diffusive regime and an enhanced diffusive regime. Using direct numerical simulations, we explain the propagation dynamics of these two transport regimes in this laterally strongly confined geometry, namely by disentangling the contributions of diffusion and convection to the propagation of the CO<sub>2</sub> front.*

---

<sup>◦</sup>Submitted as Daniel P. Faasen, **Farzan Sepahi**, Dominik Krug, Roberto Verzicco, Pablo Peñas, Detlef Lohse and Deveraj van der Meer, *Diffusive and convective dissolution of carbon dioxide in a vertical cylindrical cell*. Experiments by D. P. Faasen, simulations by F. Sepahi, analyses and writing by D. P. Faasen, F. Sepahi and D. Krug, supervision by P. Peñas, D. Krug, R. Verzicco, D. Lohse and D. van der Meer, proofread by everyone. D. P. Faasen and F. Sepahi contributed equally to this work.



## 3.1 Introduction

**D**issolution and subsequent mass transfer of carbon dioxide gas into liquid barriers plays a vital role in many environmental and industrial applications. In microfluidics for example, Taylor flow, a segmented flow of alternating gas and liquid plugs, is utilised in microreactor designs to increase heat and mass transfer rates, resulting in higher reactor performance [173–175]. On a larger scale, carbon capture and sequestration is often based on injecting CO<sub>2</sub> into deep saline aquifers, trapping the CO<sub>2</sub> between a layer of cap rock and a liquid reservoir, which results in the long term, stable storage of CO<sub>2</sub> in the aquifer [176–178].

Once the carbon dioxide starts to dissolve into the water layer, a CO<sub>2</sub>-rich water layer forms at the interface, which is denser in comparison to pure water. While initially stable, the continued dissolution of CO<sub>2</sub> into the water layer results in the CO<sub>2</sub>-rich fluid layer becoming gravitationally unstable, leading to the onset of buoyancy driven convection and the formation of a buoyant plume, which greatly enhances the mass transfer of CO<sub>2</sub> in the water layer [36, 37]. Furthermore, density driven convection can also occur as a result of buoyancy generating chemical reactions [169, 179–181], droplet dissolution [88, 182] and bubble growth [78, 183].

In literature, studies investigating the dissolution and density driven convection in the CO<sub>2</sub>-water system have reported between two and four distinct transport regimes [38–40]. These regimes are vaguely defined by their assumed dominant driving mechanism and thus referred to as, for example, "purely diffusive", "early convective", or "late convective" [38]. Moreover, in the regimes where convection is contributing to the mass transport, apparent diffusive behaviour is observed, albeit with a much higher effective diffusion coefficient. Depending on the experimental conditions, this effective diffusion coefficient can be several orders of magnitude bigger in comparison to the expected diffusive counterpart under similar experimental conditions [120, 184–187]. However, little explanation has been given as to what drives the different observed regimes, the transitions between the regimes and why the system still appears to behave in a diffusive manner.

This is precisely the focus of our work. We study the dissolution and downward propagation of CO<sub>2</sub> into a vertical water barrier confined to a narrow cylindrical cell either above a trapped air bubble, an alkane layer or directly on top of a solid silicon plate, as shown in figure 3.1. We replace the ambient air atmosphere with a CO<sub>2</sub> atmosphere at the same pressure and by adding sodium fluorescein, a pH-sensitive fluorophore, to the liquid barrier, we can directly visualise the propagation of CO<sub>2</sub> [188–190]. We compare the experimental results to those obtained by 3D direct numerical simulations, in order to elucidate the relevant transport mechanisms.

In a nutshell, our aim is to investigate the mass transport mechanisms in a laterally strongly confined system after the dissolution of  $\text{CO}_2$  into a liquid barrier. We will identify two different regimes, namely: a purely diffusive regime and an enhanced diffusive regime. The direct numerical simulations allow us to disentangle the contributions of the buoyancy driven convection and diffusion towards the front propagation velocity. We will show that the onset of convection leads to a distortion of the propagation front surface, resulting in the increase of the concentration gradients which in turn leads to enhanced diffusive fluxes. As a result, the overall behaviour remains diffusive, although with an increased diffusion coefficient. The diffusive propagation acts to flatten the interfacial area, which over time leads to an equilibrium with the convective bulging of the front, after which the front propagates at an almost constant velocity.

This paper is organised as follows. The experimental setup and procedure are described in § 3.2. Section 3.3 presents the results of our visualisation experiments. In § 3.4 the amount of  $\text{CO}_2$  in the liquid barrier over time is investigated by first obtaining the intensity profiles from the visualisation experiments and subsequently converting them to concentration profiles. In § 3.5 we study the front propagation dynamics of the  $\text{CO}_2$  layer and identify two distinct propagation regimes. In § 3.6 we provide the details on the numerical model we use to study the physics behind the front propagation dynamics and provide a comparison between the numerical model and the experiments. The paper ends with a summary of the main findings and an outlook in § 3.7.

## 3.2 Experimental procedure

A schematic overview of our experimental setup is shown in figure 3.1(a). The experiments are conducted inside a sealed chamber which can be flushed with  $\text{CO}_2$  gas. The inlet pressure is fixed to 1.0 bar using the pressure regulator PR1, whereas pressure regulator PR2 prevents over-pressurisation of the experimental tank. A more detailed description of the experimental chamber and pressure control system can be found elsewhere [191].

A single borosilicate glass (Duran) cylinder (28 mm in length, inner diameter  $d = 3.0$  mm, outer diameter of 5.0 mm) is attached on one end to a silicon wafer plate using Loctite 4305 (Farnell), in an almost perfectly vertical manner, while the other end is left open. Before use, the cylinder is rinsed using ethanol (Boom, technical grade) followed by Milli-Q water (resistivity = 18.2 M $\Omega$  cm) and finally dried in a nitrogen stream.

We prepare the cylinder in one of three different configurations, a liquid–solid,

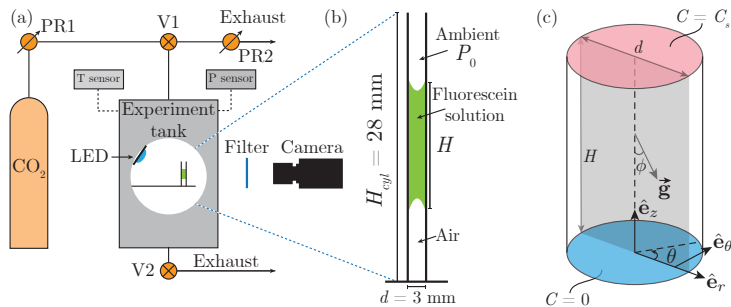


Figure 3.1: (a) Schematic overview of the experimental setup. (b) Sketch of the cylinder containing the liquid–air setup. The cylinder is placed inside the experimental chamber, which is subsequently flushed with CO<sub>2</sub> gas. (c) Schematic overview of the numerical setup.

liquid–liquid, or a liquid–air configuration, as depicted in figure 3.1(b). In all configurations, a layer of a  $10^{-4}$  M aqueous fluorescein solution is injected into the cylinder, at a volume of  $V = 120 \mu\text{L}$  (or  $H \approx 18$  mm), which acts as the liquid barrier. This solution is freshly prepared prior to the experiments by adding sodium fluorescein salt (Fisher Scientific, general purpose grade) to Milli-Q water. Fluorescein is a well known fluorophore often used in biological application, with its main absorbance peak at 490 nm and main emission peak at 513 nm [188–190]. More importantly, the emission intensity of fluorescein has a (non-linear) dependency on the pH level of the liquid, allowing us to follow the dissolution and propagation of the CO<sub>2</sub> in the liquid. Furthermore, the presence of the sodium fluorescein in the barrier does not affect the diffusive and convective behaviour of the CO<sub>2</sub>, as we have  $\sim 4.4 \mu\text{g}$  sodium fluorescein in the  $120 \mu\text{L}$  barrier to achieve the desired concentration.

For the liquid–air configuration, the fluorescein layer is placed in the cylinder such that a bubble of arbitrary height spanning the entire width of the cylinder, is trapped underneath the liquid. The liquid barrier remains in place due to a stable balance between the surface tension of the liquid–air interface, the weight of the liquid barrier, and the differences in gas pressures. Since the surface tensions of CO<sub>2</sub> and air above water are almost identical, the force balance persists throughout our experiments [192]. For the liquid–solid configuration, the fluorescein solution is injected into the cylinder such that no air is trapped between the liquid barrier and the silicon wafer plate. During this process, special attention is paid to ensure no small bubbles are entrained at the liquid–solid interface. Finally, for the liquid–liquid interface,  $60 \mu\text{L}$  *n*-hexadecane (VWR, 99% purity) is injected first into the cylinder. On top of this liquid layer, the fluorescein solution is carefully injected,

again to prevent the entrapment of bubbles. Despite the density of *n*-hexadecane being lower compared to the density of water, this configuration remains stable during our experiments, again due to a stable balance between the surface tensions at the interface and the weight of the top liquid column.

Inside the tank, a LED (Thorlabs,  $\lambda_{centre} = 470$  nm) is located to illuminate the cylinder, while the pressure and temperature sensors in the chamber record the pressure  $P_0$  and temperature  $T$  in time respectively (1 acquisition per second). The average temperature during our experiments is determined to be  $T = 22.3 \pm 0.4$  °C. We use a Nikon D850 camera in silent interval timer shooting mode (1 fps) in combination with a Zeiss Makro Planar T 100 mm lens to achieve a mean optical resolution of  $10.4 \mu\text{m}/\text{pixel}$ . In the optical path between the cylinder and the camera, a bandpass filter (Thorlabs,  $\lambda_{centre} = 530$  nm, BW = 43 nm) is located to block out the LED light.

After preparation, the cylinder is placed inside the experimental chamber. The inlet pressure is fixed to 1.0 bar using PR1 while valve V1 remains closed. Valve V2 is opened to allow the experimental tank to be flushed during the flushing stage. The LED inside the chamber is turned on and 5 seconds later the interval timer shooting mode on the camera is activated. 15 seconds after camera activation, the pressure and temperature sensor data starts being recorded. Finally, 35 seconds after turning on the LED inside the chamber, valve V1 is opened and the system is flushed with CO<sub>2</sub> gas in order to fully replace the ambient air inside the tank. The time at the start of the flushing stage is  $t = 0$  seconds and marks the start of the "experiment" stage. After flushing for 60 seconds, valves V1 and V2 are closed in quick succession, with the former being closed first to prevent pressurisation of the experimental tank. At the end of the experiment (typically at  $t = 15$  minutes), the experimental tank is opened and flushed using a nitrogen spray gun to prepare the experimental chamber for the next experiment.

Based on the aforementioned experimental conditions, we can calculate the relevant dimensionless numbers. Our Schmidt number is found to be  $Sc = \nu/D = 515$ . Since the maximum CO<sub>2</sub> concentration difference in the barrier is  $\Delta C = C_{sat}$ , we find our maximum Rayleigh number to be:

$$Ra_H \equiv \frac{\beta C_{sat} g H^3}{\nu D}, \quad (3.1)$$

where  $g$  is the acceleration due to gravity,  $\beta = (8.2 \pm 0.03) \text{ cm}^3/\text{mol}$  the solutal expansion coefficient of CO<sub>2</sub>, the saturation concentration  $C_{sat} = k_H P_0$ , with  $k_H = (3.53 \pm 0.04) \times 10^{-4} \text{ mol}/\text{m}^3\text{Pa}$  and  $P_0 = 1.0$  bar,  $D = (1.85 \pm 0.02) \times 10^{-9} \text{ m}^2/\text{s}$  the diffusion coefficient of CO<sub>2</sub> in water,  $H = 17.6 \pm 0.35$  mm the height of the liquid

barrier, and  $\nu = 9.5 \times 10^{-7} \text{ m}^2/\text{s}$  the kinematic viscosity of water [37, 193, 194]. We obtain  $\text{Ra}_H \approx (8.8 \pm 0.5) \times 10^6$ , which is well above the critical Rayleigh number,  $\text{Ra}_{H,c} = 1.29 \times 10^6$ , based on the minimal aspect ratio ( $\Gamma_{max} = d/H = 0.17$ ) of our experimental setup [195].

### 3.3 Experimental observations

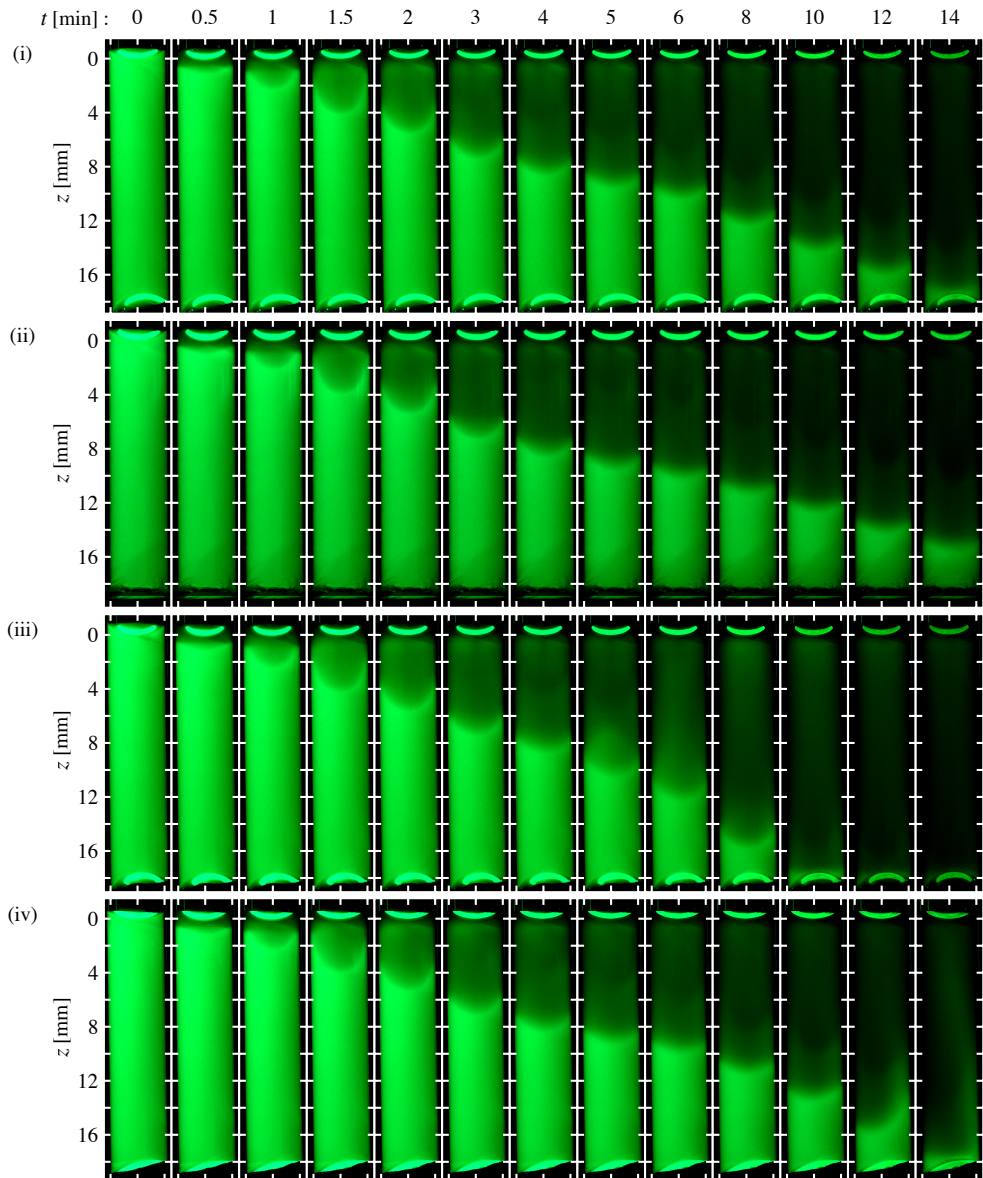
We begin by analysing a series of liquid–air experiments, (i), (iii), and (iv) in figure 3.2, and a liquid–solid experiment, (ii) in figure 3.2. Snapshots of additional experiments can be found in the Appendix 3.8.2 in figures 3.15 and 3.16. As the  $\text{CO}_2$  starts dissolving into the liquid barrier, the pH of the  $\text{CO}_2$  imbued liquid starts to decrease. Since fluorescein is a pH sensitive fluorophore in the range  $5 \lesssim \text{pH} \lesssim 10$ , the emission intensity of the fluorescein dye starts to decrease, resulting in a colour change of the dye from bright green to black in the images [196].

At the beginning of the experiments,  $t = 0 \text{ s}$ , we start replacing the air atmosphere with a  $\text{CO}_2$  atmosphere. Almost immediately,  $\text{CO}_2$  starts dissolving into the liquid barrier, forming a  $\text{CO}_2$ -rich water layer just below the gas–liquid interface. While initially stable, the continued dissolution of  $\text{CO}_2$  into the water barrier results in the layer becoming gravitationally unstable, as the  $\text{CO}_2$ -rich water is denser in comparison to the pure water underneath. Once this happens, a convective plume is shed from the  $\text{CO}_2$ -rich boundary layer which starts propagating downwards into the liquid barrier. In the experiments shown, the shedding of the buoyant plume occurs around  $t \sim 1 \text{ minute}$ .

After shedding the convective plume, differences in the  $\text{CO}_2$  front propagation dynamics can be observed. In (i) and (ii) the front appears to propagate axisym-

---

Figure 3.2 (*following page*): Fluorescence images of the initial dissolution process of  $\text{CO}_2$  in a vertical liquid column within a cylindrical cell. The fluorescence intensity decays with pH or increasing  $\text{CO}_2$  concentration. At  $t = 0$ , the upper interface is exposed to a  $\text{CO}_2$  gas ambient. Subsequently, a  $\text{CO}_2$ -containing layer (dark region) propagates downwards. The bottom liquid interface for (i, iii, iv) is liquid–air; for (ii) it is liquid–solid. The type of boundary has no impact on the propagation dynamics of the  $\text{CO}_2$  front. In (i) and (ii) the front propagates axisymmetrically throughout the entire water depth. In (iv), axisymmetry is broken at  $t \approx 12 \text{ min}$  with the shedding of a lateral buoyant upwelling plume. A similar symmetry-breaking upwelling plume occurs in (iii) at  $t \approx 5 \text{ min}$ , yet the plume appears visually centred due to the planar visualisation of the 3D system. Such an event causes the front to accelerate towards a higher velocity. Coordinate  $z$  denotes the depth from the apex of the top meniscus; the horizontal ticks are 2 mm apart.



metrically throughout the water barrier. As a result, the CO<sub>2</sub> front does not quite reach the lower liquid–gas, (i), or liquid–solid, (ii), interface. In contrast, the apparent axisymmetry observed in (i) and (ii) is seemingly broken in (iii) and (iv) at  $t = 5$  minutes and  $t = 12$  minutes, respectively. In (iv) the shedding of a lateral buoyant upwelling plume can be observed at the right side of the cylinder at the interface of the denser CO<sub>2</sub>-rich liquid and the pure bulk liquid. In (iii), the plume appears visually centred due to the planar visualisation of the 3D system. Regardless, in both cases the CO<sub>2</sub> front accelerates towards a higher velocity, leading to the front reaching the bottom liquid–air interface around  $t \sim 10$  min in experiment (iii) and  $t \sim 15$  min in experiment (iv). It therefore appears that the type of bottom boundary does not affect the CO<sub>2</sub> propagation dynamics, but the occurrence of the shedding of a secondary plume does.

To further study the propagation dynamics, we track the progression of the CO<sub>2</sub> front in the liquid barrier over time. We define 20 equispaced bins along the cylinders diameter for which the vertical intensity profiles are calculated. The obtained intensity profiles are normalised with respect to the intensity profiles at  $t = 0$ s, in order to account for variations in illumination. The CO<sub>2</sub> front is defined as the iso-concentration contour  $z_f = z_f(x, t)$  corresponding to a normalised intensity  $I^*(x, z, t)$  value of 60%. For experiments (i-iv), the obtained projected front surfaces are shown in figure 3.3. The time step between the contour lines is  $\Delta t = 20$ s. The front profiles of the additional experiments can be found in Appendix 3.8.2 in figures 3.17 and 3.18.

The shown front contours emphasise that the initial behaviour for the four experiments is very similar. After the shedding of the buoyant plume by the diffusive boundary layer, the front initially rapidly accelerates, and then slows down again as time progresses. As mentioned, in experiments (i) and (ii), the front reaches a stable velocity, indicated by the front contours becoming equidistant in space. For experiments (iii) and (iv), the arrows indicate the depth at which we observe the shedding of a lateral buoyant plume. After this event, the spatial distance between the lines increases again, indicating the acceleration of the front to a higher velocity. This is very similar to the initial shedding event observed from the diffusive boundary layer. The secondary plume shedding is not observed in all cases and is therefore likely related to uncontrolled noise in the experiments, such as small, local deviations in CO<sub>2</sub> concentration or the small inclination of the cylinder with respect to the base plate.

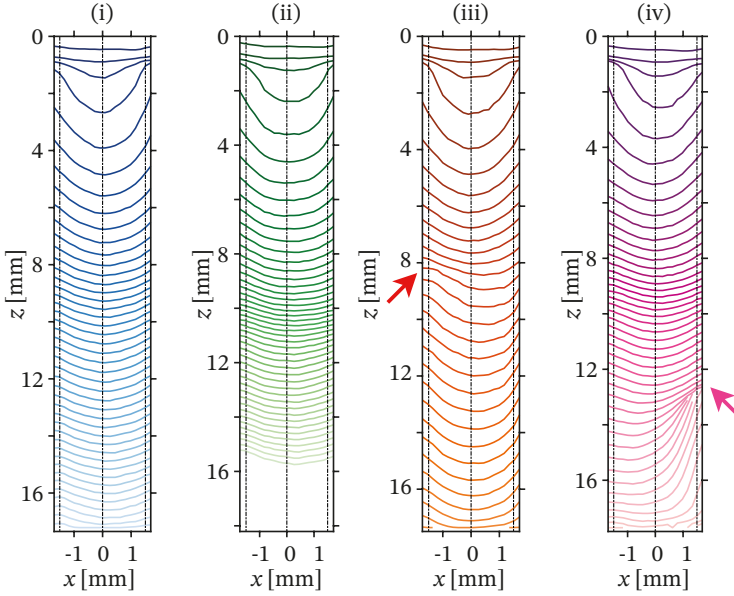


Figure 3.3: Propagation of the projected front surface for experiments (i–iv) shown in figure 3.2 during  $0 < t < 15$  min. The front is defined as the iso-concentration contour  $z_f = z_f(x, t)$  corresponding to a normalised intensity  $I^*(x, z, t)$  value of 60 %. The front is computed from the vertical intensity profiles computed across 20 equispaced positions in  $x$ . The time step between contour lines is  $\Delta t = 20$  s. In (iii) and (iv), the arrows denote the front positions at which lateral plume shedding occurs, i.e., when the axisymmetric propagation is broken.

### 3.4 Intensity and concentration profiles

We continue our analysis by investigating the amount of  $\text{CO}_2$  absorbed in the liquid barrier over time. In order to do so, we first have to obtain the intensity profiles of the fluorescein solution in the barrier and convert these to the corresponding  $\text{CO}_2$  concentration profiles. Therefore, we start by computing the horizontally averaged intensities  $G(z, t)$  which are then a function of depth  $z$  and time  $t$  only. We normalise the obtained intensities with respect to the initial intensity profile in order to account for spatial inhomogeneity of the LED lighting, defined as the normalised intensity  $I = G(z, t)/G(z, 0)$ . Additionally, we correct these intensity profiles for the decay in intensity due to photobleaching of the fluorescein solution. This is achieved by measuring the decay due to photobleaching over time in a by  $\text{CO}_2$  unaffected segment of the cylinder and correcting the measured intensities correspondingly. Finally, we once more normalise the obtained intensities by the

maximum and minimum obtained intensities of the experiment which are found to be quite close for all experiments, resulting in  $\bar{I}^*(z, t)$ .

For experiments (i-iv), the obtained intensity profiles are shown in figure 3.4(a). As before, the time step between consecutive profiles is  $\Delta t = 20s$  and the profiles are shown for the entire experiment, i.e. between  $0 < t < 15$  min. The vertical dotted lines indicate the depth of the top ( $z = 0$ ) and bottom boundaries of the liquid barrier. For experiments (i) and (ii), the steady propagation discussed before is clearly reflected in the intensity profiles. As the front propagates through the barrier, the intensity drops rapidly, as expected based on the snapshots from figure 3.2. Moreover, the decrease in propagation velocity is again reflected in the intensity profiles, as the spacing between the profiles decreases as time progresses. For experiments (iii) and (iv), the shedding of the lateral buoyant upwelling plume causes the intensity at certain depth to increase, resulting in overlapping intensity profiles.

As mentioned before, the emission intensity of fluorescein has a non-linear dependency on the pH level of the liquid. Therefore, we need to obtain a calibration curve before we can convert the measured intensities to the  $CO_2$  concentration in the barrier. To achieve this, we performed a set of experiments in which the cylinder is placed in an inverted configuration. When inverted, the  $CO_2$ -liquid mixture is stably stratified and therefore the  $CO_2$  can only be transported up the barrier by diffusion. We obtain the intensity profiles of these experiments and use these to obtain a calibration function  $C/C_{sat} = F(1 - I^*)$ , linking the dimensionless concentration in the barrier to a measured intensity by means of the self-similar solution of the pure diffusion problem. A more detailed description of this process can be found in Appendix 3.8.1.

Figure 3.4(b) shows the resulting  $CO_2$  concentration profiles for experiments (i-iv). Similarly, for experiments (v-xii), the intensity and concentration profiles can be found in Appendix 3.8.2 in figures 3.19 and 3.20. Note that we show the  $CO_2$  concentration  $\bar{C}(z, t)$  as a fraction of the saturation concentration  $C_{sat}$ , with  $\bar{C}/C_{sat} < 0.6$ , which corresponds to the lower bound of the pH-sensitive range of sodium fluorescein. As a result, we cannot differentiate concentration levels  $\bar{C}/C_{sat} > 0.6$ . The concentration values close to the boundaries of the liquid column are tainted by the presence of a meniscus (or a solid interface).

As expected, the concentration profiles of experiments (i) and (ii) show a steady progression of the  $CO_2$  concentration in the liquid barrier. In experiments (iii) and (iv), the shedding of the lateral buoyant upwelling plume causes additional  $CO_2$ -rich liquid to be propagated downwards, while additional pure liquid is propagated upward by the plume. This is reflected by the concentration profiles, as we observe a sudden increase in concentration near the bottom of the cylinder, while the con-

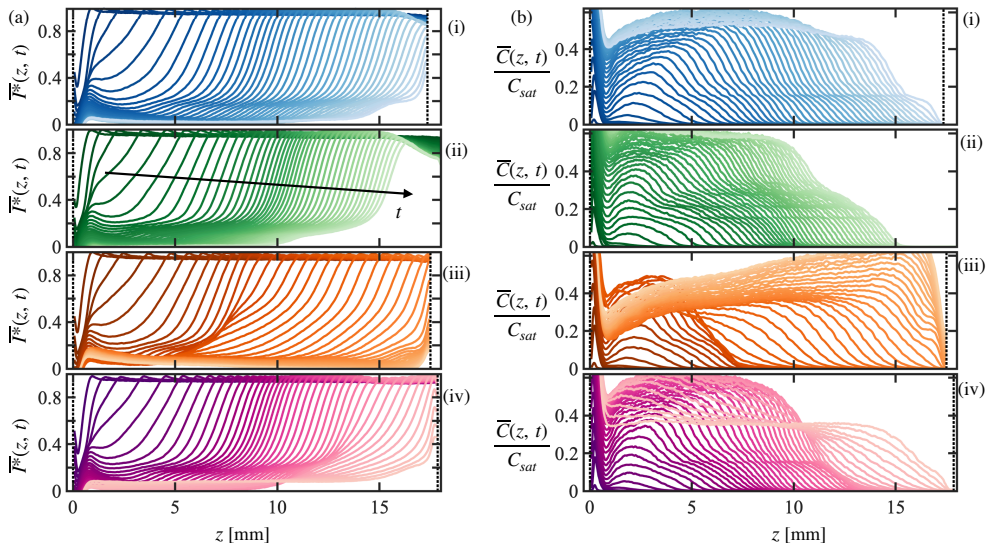


Figure 3.4: (a) Normalised intensity profiles for experiments (i–iv) from figure 3.2 and figure 3.3. The intensity profiles have been horizontally-averaged over the entire cell diameter ( $-d/2 < x < d/2$ ) at every depth  $z$ . The time step between consecutive profiles is  $\Delta t = 20$  s for  $0 < t < 15$  min. (b) Tentative concentration profiles directly obtained from  $\bar{I}^*$  after calibration;  $C_{sat}$  refers to the saturation concentration. Concentration values close to the boundaries of the liquid column are tainted by the presence of a meniscus (or a solid interface) and are limited to  $\bar{C}/C_{sat} < 0.6$ , which corresponds to the lower bound of the pH-sensitive range of sodium fluorescein. The vertical dotted lines indicate the depth of the top ( $z = 0$ ) and bottom boundaries of the liquid barrier.

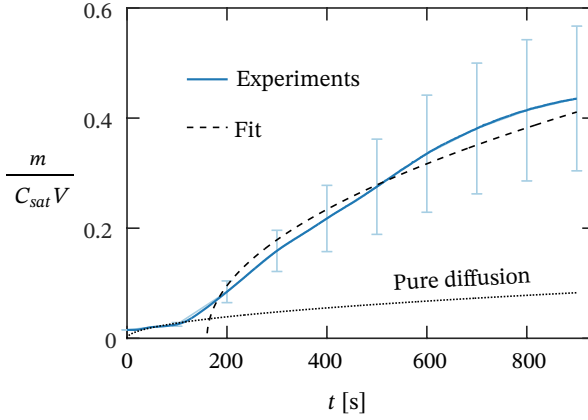


Figure 3.5: Mass  $m$  of  $\text{CO}_2$  absorbed by the liquid column as a function of time, averaged across all 12 experiments;  $m$  is normalised by the maximum dissolution capacity  $C_{sat}V$ , where  $V \equiv \pi d^2 H/4$  is the liquid volume and  $C_{sat}$  the saturation density (or concentration) of  $\text{CO}_2$  in water. The dissolution fraction is estimated from the 1D axial concentration profiles as  $m(t)/(C_{sat}V) = H^{-1} \int_0^H \bar{C}(z, t)/C_{sat} dz$ . The wide error bars reflect the variability between experiments and the uncertainties in concentration calibration. The dissolution curve initially follows the self-similar solution for pure diffusion (dotted line):  $m = 2C_{sat}A\sqrt{Dt/\pi}$ , where  $A = \pi d^2/4$ . At the onset of convection it starts to deviate from the purely diffusive behaviour due to the contribution of convection. In that regime the curve can be described by an effective diffusive behaviour  $m = 2C_{sat}A\sqrt{D_c(t-t_c)/\pi}$  (dashed line), with the fit  $D_c = 30D$  as the effective diffusion coefficient and  $t_c = 160$  s as the virtual time origin.

centration decreases sharply at the top. Furthermore, an increase in mass transfer can also be observed after the shedding event, as the spatial spacing between the profile increases after shedding the buoyant plume.

Finally, we use the obtained  $\text{CO}_2$  concentration profiles to calculate the total mass  $m$  of  $\text{CO}_2$  absorbed by the liquid barrier as a fraction of the maximum dissolution capacity. We obtain the dissolution fraction from the  $\text{CO}_2$  concentration profiles as:

$$\frac{m(t)}{C_{sat}V} = H^{-1} \int_0^H \bar{C}(z, t)/C_{sat} dz, \quad (3.2)$$

where  $m(t)$  is the total mass of  $\text{CO}_2$  in the liquid phase,  $C_{sat}$  the saturation concentration of  $\text{CO}_2$  in water, and  $V \equiv \pi d^2 H/4$  the volume of the liquid barrier. As mentioned before, we can only measure the concentration up to  $\bar{C}/C_{sat} < 0.6$ , as higher concentrations are outside the pH sensitive range of the fluorescein. Fig-

ure 3.5 shows the obtained dissolution fraction  $m(t)/(C_{sat}V)$  versus time, averaged over all 12 experiments. The wide error bars reflect the variability among experiments, such as the occurrence of the shedding of a lateral buoyant upwelling plume, and the uncertainties in the concentration calibration. Initially, the dissolution curve follows the self-similar solution for pure diffusion (dotted line), where  $m = 2C_{sat}A\sqrt{Dt/\pi}$  and  $A = \pi d^2/4$ . However, after the onset of convection, the curve deviates, resulting in  $m = 2C_{sat}A\sqrt{D_c(t-t_c)/\pi}$  (dashed line) to be the best fit, with an effective diffusion coefficient of  $D_c = 30D$  and  $t_c = 160$  s as the virtual time origin. Compared to other authors, who report finding  $D_c/D \sim 10^2$  or  $10^3$  for experiments conducted in varying PVT or Hele-Shaw cells, this seems reasonable as variations in experimental conditions and cell configuration differences appear to severely affect the obtained effective diffusion coefficients [120,184–187].

### 3.5 Front propagation dynamics

We carry on our analysis by focusing on the propagation dynamics of the CO<sub>2</sub> front in the liquid barrier. We define the position of the CO<sub>2</sub> front,  $z_f(t)$ , which we arbitrarily set to the 60%-intensity threshold of the horizontally averaged intensity profiles,  $\bar{I}^*(z_f, t) = 0.6$  (cf. figure 3.4). Tracing this position in time yields figure 3.6, which shows the front trajectories of all 12 experiments versus time. The trajectories are offset by the (fitted) virtual origin  $z_0 = -0.3 \pm 0.06$  mm and  $t_0 = 5.5 \pm 2.2$  s of the diffusive regime. Correcting for the virtual origin absorbs the influence of the finite curvature of the top meniscus and the typical flushing response time required for full exposure to the CO<sub>2</sub>. Furthermore, the front trajectories in figure 3.6 have been colour coded based on the absence (green) or the occurrence (red) of the shedding of an upwelling plume.

As explained before, the dissolution of CO<sub>2</sub> into the liquid barrier results in the formation of a boundary layer at the top interface. The mass transport in this layer is driven purely by diffusion and it is therefore unsurprising that the propagation of the front  $z_f(t)$  follows the self-similar solution for pure diffusion:

$$\frac{C(z, t)}{C_{sat}} = \operatorname{erfc}\left(\frac{z - z_0}{\sqrt{4D(t - t_0)}}\right). \quad (3.3)$$

The front trajectory associated to concentration  $C_f$  is thus

$$z_f - z_0 = K_f \sqrt{D(t - t_0)}, \quad (3.4)$$

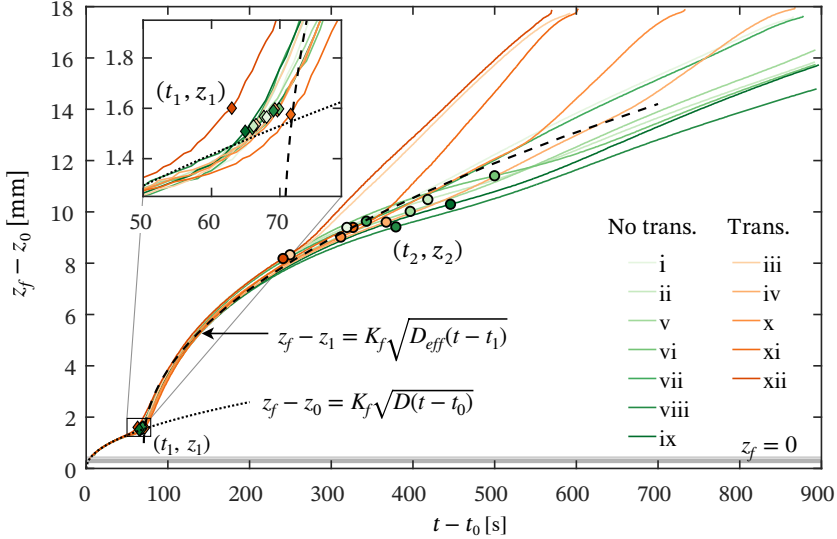


Figure 3.6: Front trajectory  $z_f(t)$  corresponding to the 60 %-intensity threshold of the horizontally-averaged intensity profiles (cf. figure 3.4), namely,  $\bar{I}^*(z_f, t) = 0.6$ . The front trajectory of all 12 experiments is plotted, which are colour-coded based on the absence (greens) or the occurrence (reds) of the shedding of the upwelling plume. The time  $t$  and front position  $z_f$  (the latter defined as the distance to the apex of the top meniscus) have been offset by the (fitted) virtual origin of the diffusive regime ( $t_0 = 5.5 \pm 2.2$  s and  $z_0 = -0.3 \pm 0.06$  mm), which absorb the influence of the finite curvature of the top meniscus and the typical flushing response time required for full exposure to the  $\text{CO}_2$  ambient. Initially,  $z_f(t)$  follows the self-similar solution for pure diffusion (dotted line), taking  $K_f \equiv 2\text{erfc}^{-1}(C_f/C_{sat}) = 4.27$  corresponding to  $C_f/C_{sat} = 2.5 \times 10^{-3}$  ( $I^* = 0.6$ ). The onset of the convective instability (diamond markers) occurs at  $t = t_1$ ,  $z_1 = z_f(t_1)$ , when the front acceleration ( $d^2z_f/dt^2$ ) is maximum. A zoom-in is provided in the inset, which highlights the reproducibility of the time onset:  $t_1 - t_0 = 67.6 \pm 2.4$  s. Thereafter,  $z_f(t)$  evolves in an enhanced diffusive manner (dashed line), with an effective fitted diffusivity  $D_{eff} = 8.25D$ , which implies that the convective velocity of the front decays in time. At approximately  $t = t_2$  (circular markers), when  $d^2z_f/dt^2 = 0$  for the first time, the front velocity stabilises and the front propagates as expected for late stage enhanced diffusive behaviour. For experiments in which an upwelling plume is shed,  $t = t_2$  marks this moment and the velocity shoots off towards a higher velocity.

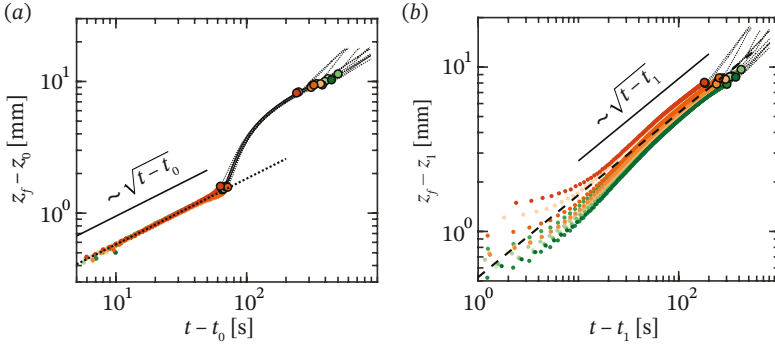


Figure 3.7: Double logarithmic plot of the two distinct regimes observed for the 12 front trajectories plotted in figure 3.6: (a) the purely diffusive regime for  $t < t_1$ , and (b) the enhanced diffusive regime for  $t_1 < t$ . In (b), the convective virtual origin ( $t_1, z_1$ ) is off-scale and has been fitted accordingly, given that the front behaviour around  $t_1$  is transitioning (during a transition period of  $\sim 10$  s) and consequently does not offer a suitable virtual origin of the convective-decay regime.

where growth prefactor  $K_f$  depends on the concentration

$$K_f \equiv 2\text{erfc}^{-1}(C_f/C_{sat}). \quad (3.5)$$

In figure 3.6, the dotted line follows from (3.4) and (3.5), taking  $K_f = 4.27$  corresponding to  $C_f/C_{sat} = 2.5 \times 10^{-3}$  ( $I^* = 0.6$ ). We see that  $z_f(t)$  follows the self-similar solution up to time  $t_1$ . We therefore define this first regime between  $t_0 < t < t_1$  as the purely diffusive regime. In figure 3.7(a), we show a rescaled plot of the purely diffusive regime on a double logarithmic scale, magnifying the  $z_f(t) \sim \sqrt{t - t_0}$  scaling relation.

At time  $t_1$ , we observe a sharp acceleration of the  $\text{CO}_2$  front position, due to the onset of the convective instability. Therefore, we can find  $t_1$  and correspondingly  $z_f(t_1) = z_1$  by finding the point in time at which the front acceleration,  $d^2z_f/dt^2$ , is maximum, indicated in figure 3.6 with the diamond markers. The inset shows a zoom-in around  $t_1$  to show the reproducibility of the onset time  $t_1 - t_0 = 67.6 \pm 2.4$  s, and corresponding front depth  $z_1 = 1.26 \pm 0.08$  mm.

At the onset of convection, the Rayleigh number based on the thickness  $\delta(t)$  of the boundary layer is given by

$$Ra_\delta(t) \equiv \frac{\beta C_{sat} g \delta^3(t)}{\nu D}. \quad (3.6)$$

The height of the liquid barrier  $H$  does not influence the onset. Taking the boundary

layer thickness equal to the position of the front at the time we observe the onset of convection, i.e.  $\delta = z_f(t_1) = z_1$ , we obtain a critical value of  $Ra_{z_1} = (3.30 \pm 0.6) \times 10^3$ , by taking the average critical value for the twelve experiments shown in figure 3.6. We compare this value to the critical Rayleigh number from Ahlers *et al.* for Rayleigh-Bénard convection in a cylinder with adiabatic sidewalls, which we believe to be the closest available approximation to our system [195]:

$$Ra_c \equiv 1708 \left( 1 + \frac{0.77}{\Gamma(t_1)^2} \right)^2, \quad (3.7)$$

where the local aspect ratio is defined as  $\Gamma(t_1) = d/z_f(t_1)$ . However, we have to emphasise the differences between our system and the systems usually described in Rayleigh-Bénard convection studies, for which (with constant  $\Gamma$ ) equation (3.7) holds. First of all, in those systems, it is assumed that at the onset of convection, a linear concentration (or temperature) profile exists as the base state which subsequently becomes unstable. Secondly, Rayleigh-Bénard setups have reached a steady state (or are very close to such), while in our experiment the system has not and never will reach a steady state during our experimental time frame. Finally, a constant aspect ratio is assumed, while in our experiment the aspect ratio continuously decreases with time, since the front position  $z_f(t)$  increases in time.

In our experiments, it is clear from figure 3.4(b) that we have non-linear concentration profiles in the boundary layer. As a result, the thickness of the self-similar diffusion boundary layer is not easy to define. If we use  $\delta$  to denote the effective thickness of the boundary layer, then  $\delta = K_\delta \sqrt{D(t-t_0)}$ , where the growth prefactor  $K_\delta \equiv 2\text{erfc}^{-1}(C_\delta/C_{sat})$  depends on the choice of the concentration cut-off  $C_\delta$ , and hence  $\delta$  may differ from the depth  $z_f = K_f \sqrt{D(t-t_0)}$  of our chosen iso-concentration contour  $C_f/C_{sat} = 2.5 \times 10^{-3}$ . For example, when we calculate  $Ra_c$  from (3.7), using  $\Gamma(t_1) = d/z_f(t_1) \approx 2.4$ , we find  $Ra_c = 2.20 \times 10^3$ , which is smaller than  $Ra_{z_1}$ . The value of  $\delta$  that satisfies  $Ra_\delta = Ra_c$ , i.e. for which (3.6) and 3.7 intersect, is exactly  $\delta = \delta^* = 1.06$  mm, which is reasonably close to  $z_1$ , with a corresponding  $Ra_{\delta^*} = Ra_c = 2.05 \times 10^3$ . This further emphasises the difficulty in defining the thickness for the self-similar diffusion boundary layer, as by selecting a lower intensity threshold, and thus higher concentration cut-off  $C_\delta$ , we could have reproduced the prediction from Ahlers *et al.* [195].

In addition, we compared our findings with the work of Tan & Thorpe (1992, 1999), who also studied the dissolution of  $\text{CO}_2$  in water [84,197] and transient heat conduction in deep fluids [79]. In their works, they try to account for the non-linear profile in the boundary layer within a theoretical framework which is compared with the experimental data. Using a PVT cell, they report an onset time of  $t = 100$

s for CO<sub>2</sub> dissolution in water. Deriving an expression for the maximum transient Rayleigh number,  $Ra_{max}$ , and taking  $Ra_c = 1100$  (which holds for Rayleigh-Bénard setups with a linear profile and upper free-surface [83]), yielded the transition times with close agreement with experiments [84]. When we enter the onset time obtained from our experiments, we find  $Ra_{max} = 336$ . This  $Ra_{max}$  is much lower than  $Ra_c = 1100$ , even though their setup is significantly wider than ours ( $d = 90$  mm compared to our  $d = 3$  mm), which suggests that our critical Rayleigh number should be even higher than 1100.

We conclude that applying the method from Tan & Thorpe (1992, 1999) [84, 197] to obtain the onset time leads to a severe and unrealistic overestimation for our experiments, which could be connected to the fact that in [84, 197] the pressure response of the system was studied instead of directly comparing to the concentration profile. The plot reporting the onset time in Ref. [84] comes with significant uncertainty. We note that adopting  $t = 64$  s instead of  $t = 100$  s, which still seems consistent with the data in [84], would result in similar findings to ours. Tan & Thorpe (1992) [84], however, does indicate that it is quite difficult to define a precise critical Rayleigh number for experiments with a non-linear profile, as we also discussed above. We therefore conclude that our method of finding the critical Rayleigh number using (3.6) and the boundary layer thickness at the onset gives the best approximation of the critical Rayleigh number for the chosen iso-concentration contour, which in our case is  $C_f/C_{sat} = 2.5 \times 10^{-3}$ .

After the onset of convection, the front propagates seemingly in a diffusive manner, however with an increased effective diffusion coefficient. By fitting all 12 experiments (dashed line in figure 3.6) we find that  $z_f(t)$  evolves with an effective fitted diffusivity  $D_{eff} = 8.25D$ . For comparison, Karimaie and Lindeberg report  $D_{eff} = 5.8D$  for transport of CO<sub>2</sub> in water confined in porous media [185]. Moreover, figure 3.7(b) shows the same regime on a double logarithmic scale, highlighting the  $z_f(t) - z_1 \sim \sqrt{t - t_1}$  scaling relation. As a result, we define this regime as the enhanced diffusive regime.

Eventually, the system appears to stabilise, leading to the front propagating at a seemingly stable terminal velocity. This moment, defined as the first time at which  $d^2z_f/dt^2 = 0$ , is referred to as  $t = t_2$ , marked with circular markers in figure 3.6(b). While one could see this as a separate regime, it is in fact the late stage behaviour of the second regime. A more detailed explanation will be given in the next section. For experiments in which the shedding of an upwelling plume occurs,  $t = t_2$  also happens to mark the moment at which this shoot off occurs. As mentioned before, if this event occurs, the front accelerates and propagates with a higher velocity in comparison to the experiments in which axisymmetry is not broken. As

a result, curves with a second shedding event shoot off in figure 3.6 (red curves), although their scaling behaviour remains consistent with the experiments in which the shedding of the upwelling plume does not occur.

## 3.6 Numerical model

### 3.6.1 Setup and governing equations

We continue our analysis by employing Direct Numerical Simulations (DNS) to unravel the physics governing the plume dynamics observed in the experiments. The numerical set-up, shown in figure 3.1(b), is a single-phase buoyancy-driven flow confined in a cylinder with an adiabatic sidewall and free-shear surfaces at top and bottom. The system is subjected to constant saturation concentration of carbon dioxide at the upper plate and zero concentration at the bottom. The dimensionless form of the advection-diffusion equation coupled with the three dimensional Navier-Stokes equations are employed under the incompressibility condition and the Oberbeck-Boussinesq approximation (in order to account for buoyancy forces caused by the (small) density variations);

$$\frac{\partial \tilde{C}}{\partial \tilde{t}} + \tilde{\mathbf{u}} \cdot \nabla \tilde{C} = \frac{1}{\sqrt{RaSc}} \nabla^2 \tilde{C}, \quad (3.8a)$$

$$\frac{\partial \tilde{\mathbf{u}}}{\partial \tilde{t}} + \tilde{\mathbf{u}} \cdot \nabla \tilde{\mathbf{u}} = -\nabla \tilde{P} + \sqrt{\frac{Sc}{Ra}} \nabla^2 \tilde{\mathbf{u}} + \tilde{C} \hat{\mathbf{e}}_{\mathbf{g}} \cdot \hat{\mathbf{e}}_k, \quad (3.8b)$$

$$\nabla \cdot \tilde{\mathbf{u}} = 0. \quad (3.8c)$$

Here,  $\tilde{C}$ ,  $\tilde{\mathbf{u}}$  and  $\tilde{P}$  denote the dimensionless concentration, velocity, and pressure respectively. The height of the cylinder  $H$ , the carbon dioxide saturation concentration  $C_s$ , and the free fall velocity  $\sqrt{g\beta C_s H}$  have been used for normalisation of the equations, where  $g$  is the gravitational acceleration and  $\beta$  the (isobaric and isothermal) volumetric concentration expansion coefficient.  $\nabla$  is the gradient operator in cylindrical coordinates,  $\hat{\mathbf{e}}_{\mathbf{g}}$  is the unit normal vector in direction of the gravitational acceleration and  $\hat{\mathbf{e}}_k (k = z, r, \theta)$  are the unit normal vectors pointing toward the axial, radial or azimuthal directions as shown in figure 3.1(c). The control parameters of the numerical model are the Rayleigh number  $Ra_H$  and the Schmidt number  $Sc$  as defined in § 3.3.

The governing (3.8) have been solved using a second-order accurate finite-difference scheme on a staggered grid and a fractional-step time-marching approach, the detail

of which can be found in [92]. Introducing a disturbance to the system is necessary to trigger the instabilities arising from the buoyancy driven convection. Hence, three different sources of disturbance are tested in the numerical simulations in order to find the most appropriate set-up which reasonably replicates the experimental observation. These are:

- (A) a perturbed initial concentration field with a random positive noise throughout the system, whose amplitude varies between zero and 1% of the carbon dioxide saturation concentration;
- (B) a meniscus liquid-gas interface at the top rather than a flat interfacial boundary. The meniscus shape was approximated by a cosine profile with a maximum depth of  $0.01H$  at the centre of the domain. Saturation concentration and no-slip velocity conditions are enforced at the interface using an immersed boundary method based on linear interpolations as developed in [198];
- (C) a slight tilt of the container relative to the direction of gravity, see figure 3.1(c). The tilting has been performed by rotating the gravitational acceleration vector  $\mathbf{g}$  by the angle of  $\phi$  with respect to the negative axial direction in  $\theta = 0$  plane. The inclination angles of  $\phi = 0.5^\circ, 1^\circ, 1.5^\circ$  and  $2^\circ$  have been tested in the numerical simulations.

Simulations have been conducted for the aforementioned cases (A)-(C) with different sources of disturbance. The grid resolution of  $32 \times 192 \times 256$  in radial, azimuthal, and axial directions respectively, similar to that of confined-rotating Rayleigh-Bénard convection [199], have been used after a grid independence check has been performed. Time marching has been achieved with variable time steps with a maximum of  $d\tilde{t} = 2 \times 10^{-3}$  and  $CFL = 5 \times 10^{-1}$ . The input of the simulations are the aspect ratio of the setup  $\Gamma = d/H$ , the height-based Rayleigh number  $Ra_H$ , and the Schmidt number  $Sc$  which have been chosen as 0.1704,  $8.8 \times 10^6$ , and 515, in accordance with the experiments.

### 3.6.2 Numerical results

The vertical location of the front corresponding to  $\overline{C}(z)/C_{sat} = 2.5 \times 10^{-3}$ , consistent with the analysis of the experimental results, has been plotted as a function of time in figure 3.8 and compared to the experiments. The front location follows that of the pure diffusion problem in all cases up to the moment when convection sets in. Looking into the transition time, a remarkable discrepancy exists between the experiments and case (A) where the initial concentration field is perturbed. On the

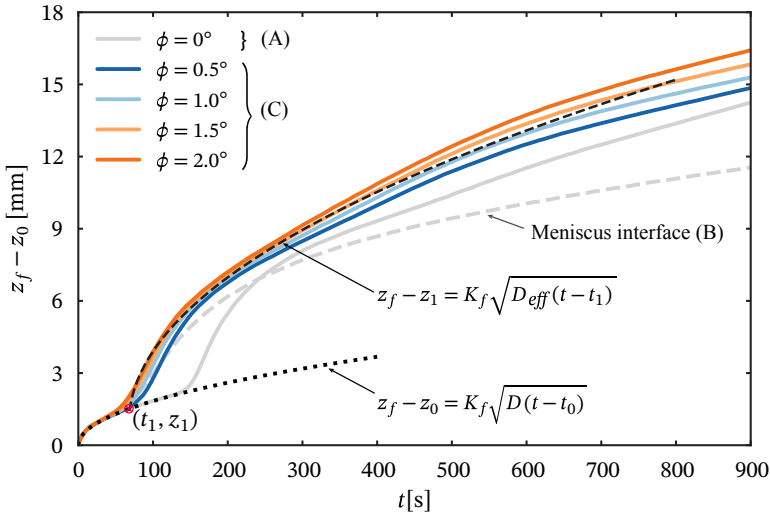


Figure 3.8: Front trajectory  $z_f(t)$  corresponding to  $\bar{C}(z)/C_{sat} = 2.5 \times 10^{-3}$  obtained via numerical simulations performed under different conditions, namely cases (A)-(C) as explained in the main text. The analytical solution of the purely diffusive problem (dotted black line) and the experimentally averaged trajectory after the onset of convection (dashed black line) have been provided for comparison.

other hand, the agreement is reasonable for cases (B) and (C). For case (B), in which the top interface is modelled as a meniscus, it can be seen that, despite an accurate prediction of the onset time, the front velocity after the onset of convection is underestimated. Only the simulations from case (C), in which the setup is tilted and the shedding of the plume is therefore asymmetric, can reproduce the transient front location obtained in the experiments reasonably well. On this basis, we conclude that the dynamics are very sensitive to small tilt angles and that likely such a small misalignment also exists in the present experiments. Accordingly, we continue by analysing the results obtained by numerical modelling for case (C), specifically with an inclination angle of  $\phi = 1.5^\circ$ , which shows the best agreement with the experiments. For reference, the carbon dioxide concentration profile for case (B) with the meniscus interface can be found in Appendix 3.8.2.

Figure 3.9 shows the simulation snapshots for the carbon dioxide concentration profile superimposed with the front isocontour corresponding to  $C_f/C_{sat} = 2.5 \times 10^{-3}$  and vectors representing the velocity field. The shown slices correspond to the inclination plane  $\theta = 0$ , the plane in which also the gravity vector is tilted. Initially, the front isocontour propagates as a horizontal line, following the analyt-

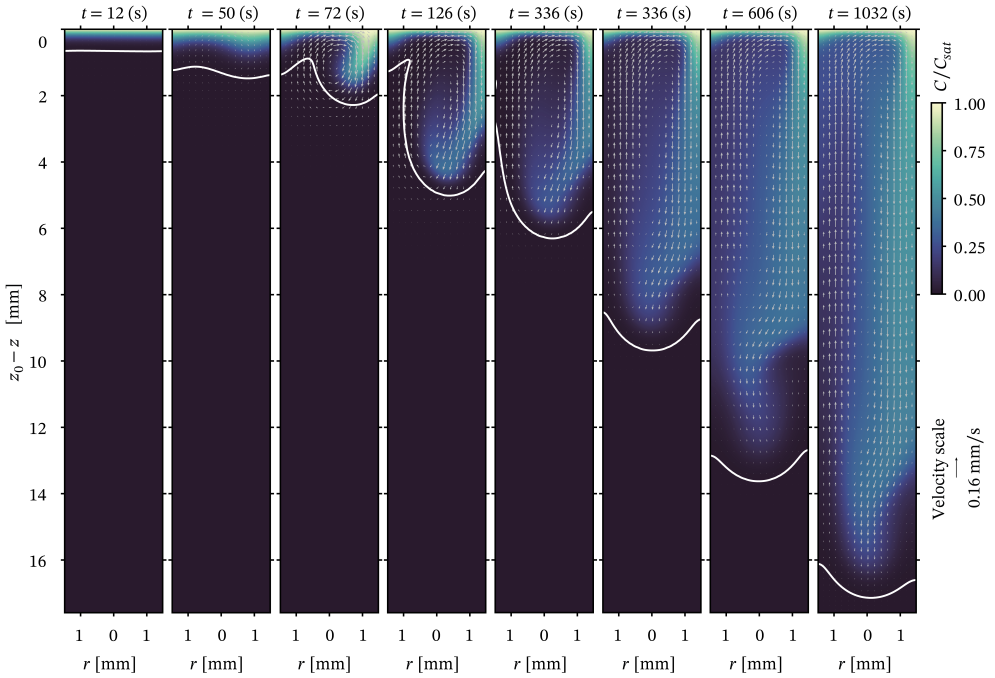


Figure 3.9: Time evolution of carbon dioxide concentration obtained by numerical simulations for case (C) with inclination angle of  $\phi = 1.5^\circ$ . The setup has been tilted in the  $\theta = 0^\circ$  plane from which the snapshots have been taken. The white contour-lines show the front profile associated with  $C_f/C_{sat} = 2.5 \times 10^{-3}$ . Vectors denote the velocity field, the scaling of which has been provided in the figure.

3

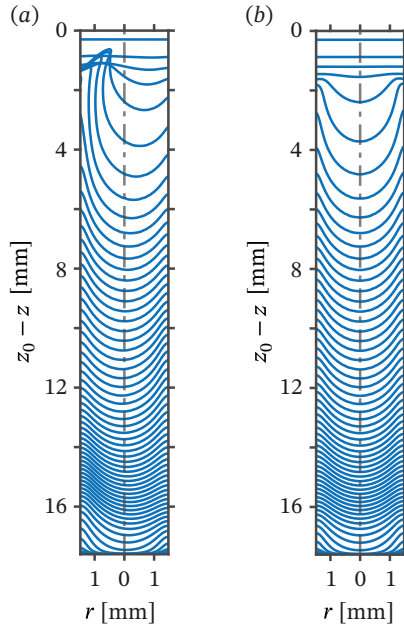


Figure 3.10: Propagation of the front isosurface obtained from numerical simulations for case (C) with inclination angle of  $\phi = 1.5^\circ$ . The front isosurfaces correspond to  $C_f/C_{sat} = 2.5 \times 10^{-3}$  and have been taken at (a)  $\theta = 0$ , i.e., the inclination plane of gravity and (b)  $\theta = 90^\circ$  plane. Note that the propagation appears to be axisymmetric in the latter.

ical solution of the pure diffusion problem as shown in figure 3.8. Around  $t \sim 1$  minute, as observed in figure 3.8, convection sets in and as a result a vortex forms above the front whose direction is clockwise and consistent with the tilting direction of the setup. Therefore, the front shape gets distorted complying with the flow structure forming behind. The generated convective flow remains active behind the front during its entire evolution from top to the lower boundary of the setup and its deformed shape at very low concentrations, suggests a complex concentration field in the solution. Remarkable asymmetry in the front profile, particularly at the transition time, is observed from the simulations result as opposed to the experimental measurements. However, this also strongly depends on the angle of the view. The shape evolution of the front isocontour, shown in figure 3.10 for two different 2-dimensional slices corresponding to  $\theta = 0^\circ$  and  $\theta = 90^\circ$ , indicates axisymmetric or asymmetric profiles depending on the frame of reference chosen. The 3D shape of the front isosurface has also been plotted in time in figure 3.12, which will be dis-

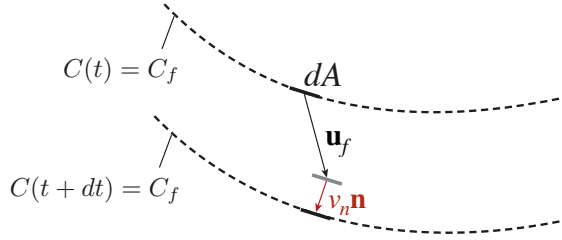


Figure 3.11: Graphical representation of the local propagation velocity of the front isosurface.

cussed in more detail in the next section in order to clarify the physical mechanisms governing the interface dynamics.

### 3.6.3 Front local propagation velocity

Next, we consider the propagation of the front in more detail. As shown schematically in figure 3.11, the velocity ( $\mathbf{u}_{iso}$ ) of an interface element  $dA$  of the front can be decomposed into a component due to the advection of the underlying fluid element and a propagation relative to the latter ( $\mathbf{V}$ ), such that  $\mathbf{u}_{iso} = \mathbf{u}_f + \mathbf{V}$ . By definition, the interface propagation is normal to the iso-surface such that  $\mathbf{V} = v_n \hat{\mathbf{n}}$ , with the surface unit normal vector  $\hat{\mathbf{n}} = \nabla C / |\nabla C|$ . Following an approach previously employed for enstrophy iso-surfaces in turbulent flows [200,201], iso-scalar surfaces in turbulent scalar mixing with chemical reactions [202] and flame propagation in combustion problems [203], we can derive an expression for the interface propagation velocity  $v_n$  by noting that in a frame of reference moving with the iso-surface element, the total rate of change of concentration is zero. This leads to

$$\frac{D^s C}{D^s t} = \frac{\partial C}{\partial t} + \mathbf{u}_{iso} \cdot \nabla C = \frac{\partial C}{\partial t} + (v_n \hat{\mathbf{n}} + \mathbf{u}_f) \cdot \nabla C = 0, \quad (3.9)$$

which can be solved for  $v_n$  to yield

$$v_n = -\frac{\frac{\partial C}{\partial t} + \mathbf{u}_f \cdot \nabla C}{|\nabla C|} = -\frac{\frac{DC}{Dt}}{|\nabla C|} = -\frac{D\nabla^2 C}{|\nabla C|}. \quad (3.10)$$

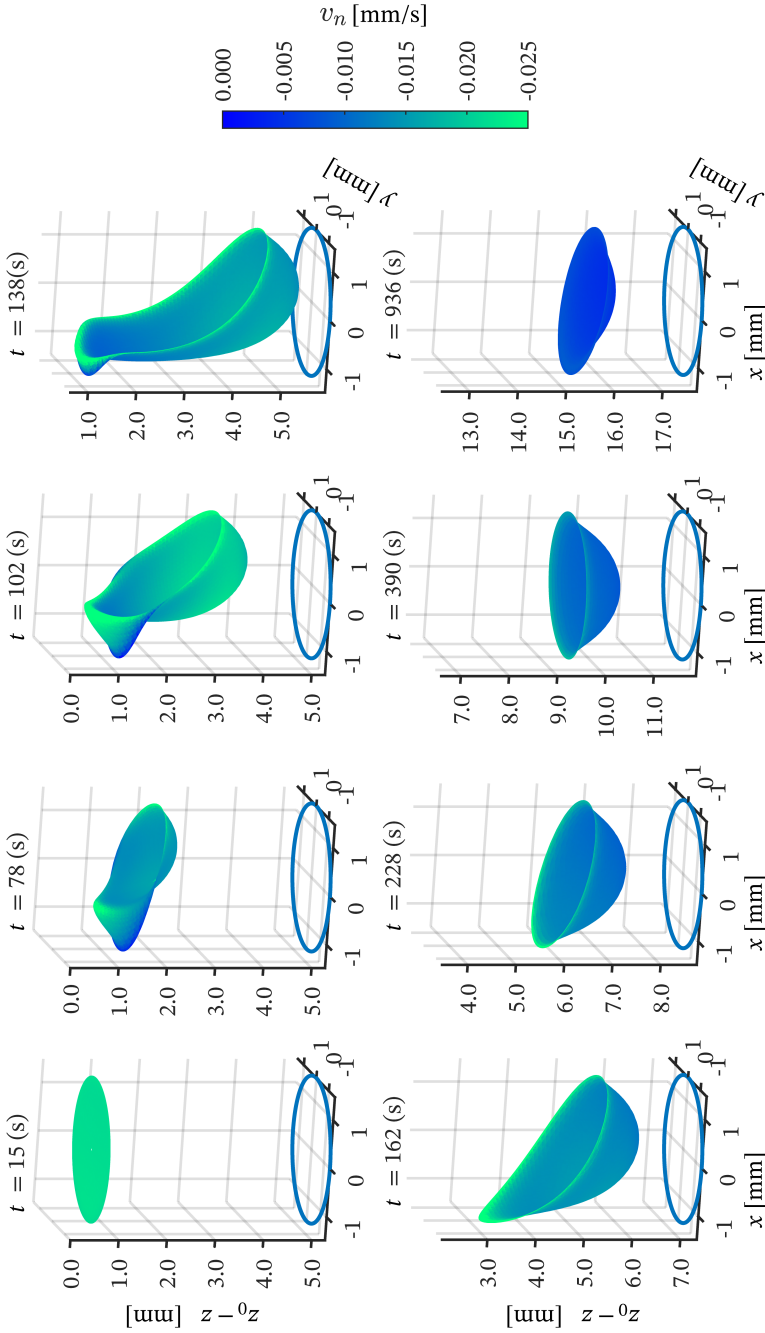


Figure 3.12: 3D plot of the front isosurface evolving in time for case (C) with inclination angle of  $\phi = 1.5^\circ$ . The isosurfaces correspond to  $C_f/C_{sat} = 2.5 \times 10^{-3}$ . The colourmap indicates the local propagation velocity of the front  $v_n$  normal to the isosurface calculated according to (3.10).



Given the incompressibility of the fluid, advection does not affect the mean interface position. The front propagation is therefore solely related to  $v_n$  and therefore diffusive in nature at all times. A quantitative relation can be obtained by equating the volume flux across the convoluted interface to that through the mean interface according to [204,205]

$$Q \equiv \int_{A_{iso}} v_n dA = A_0 \frac{dz_m}{dt}, \quad (3.11)$$

where the integration is over the surface area  $A_{iso}$  of the iso-contour. Using an average of  $v_n$  across  $A_{iso}$  denoted by the overbar, this leads to

$$\frac{dz_m}{dt} = \frac{A_{iso}}{A_0} \bar{v}_n, \quad (3.12)$$

which now expresses the mean front propagation as diffusive propagation ( $\bar{v}_n$ ) amplified by interface convolutions. Note that here we use  $z_m$  to denote the mean position of the isosurface instead of  $z_f$  in order to distinguish the volume average implied by (3.11) from the 2D average used for  $z_f$ .

Figure 3.12 shows the front corresponding to the isosurface at  $C/C_{sat} = 2.5 \times 10^{-3}$  at different moments in time and color-coded with the local magnitude of  $v_n$ . From these snapshots it becomes clear how convection significantly enhances the interfacial surface area, which is then decreased again as a result of the interface propagation. Convection is also seen to increase  $v_n$  locally, in particular around  $t = 100s$ , which is due to a steepening of the scalar gradients close to the front (see also figure 3.9). Here it should be noted that  $\hat{\mathbf{n}} = \nabla C / |\nabla C|$  always points toward the region with higher concentrations, i.e., the region above the front iso-surface, such that negative values of  $v_n$  correspond to an outward propagation of the interface.

Results for computing the volume flux across the interface from integrating  $v_n$  ( $Q$ ) and based on evaluating  $A_0 dz_m/dt$  are compared in figure 3.13(a). As can be seen the agreement is very good as expected, apart from a short period around  $t \approx 150$  s. During this time, the wall-parallel part of the iso-surface reaches the wall (see figure 3.12), leading to a sudden decrease in the front surface area as well as in its mean location, which is not captured sufficiently accurately by our method to extract the isosurface.

The panel in figure 3.13(b) presents the same data as figure 3.13(a), only this time expressed as effective mean front velocities according to (3.12). This form enables a direct comparison to the front velocity based on  $z_f$ , previously shown in figure 3.8. For most times the agreement between  $dz_f/dt$  and  $dz_m/dt$  is good, but significant difference arise for the peak following the onset of convection. This highlights that especially during this period ( $70 \lesssim t \lesssim 200$ ) it is important to account for the three-dimensionality of the flow.

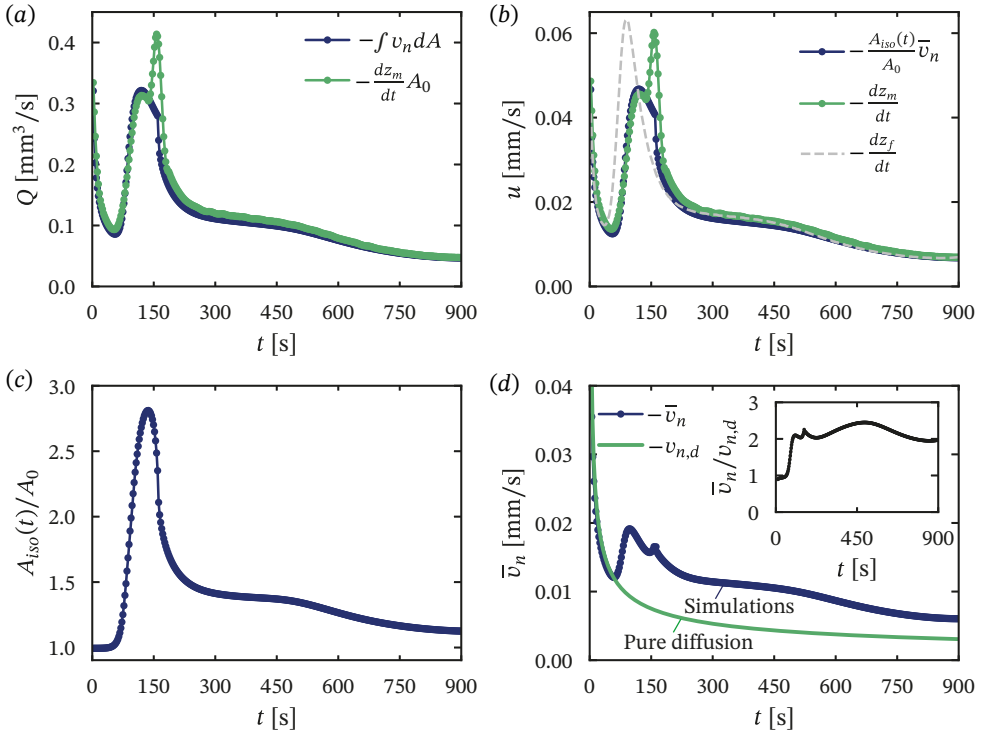


Figure 3.13: (a) Volumetric flux  $Q$  of the local propagation velocity  $v_n$  across the front iso-surface, compared to the rate of change in the mean volume above the iso-surface,  $A_0 dz_m/dt$ . (b) Front propagation velocity computed from the time evolution of the cross-sectional average of the 3D iso-surface,  $dz_m/dt$ , and from the product of the relative surface area and averaged local propagation velocity.  $dz_f/dt$  is provided where  $z_f$  is the front trajectory obtained from the horizontally-averaged concentration profile in 2D slices, in accordance with the front tracking approach in experiments. (c) Relative surface area of the iso-surface with respect to the cross sectional area of the cylinder,  $A_0$ . (d) Temporal evolution of the averaged local propagation velocity,  $\bar{v}_n$ , of the iso-surface.  $\bar{v}_n$  for the iso-surface in pure-diffusion problem, compared to the pure diffusive case,  $v_{n,d}$ , where it equals the front propagation velocity  $dz_m/dt = K_f [D(t - t_0)]^{-1/2}$ , with  $K_f$  defined in (3.5). The ratio  $\bar{v}_n/v_{n,d}$ , is shown in the inset.

The volumetric fluxes and propagation velocity of the front are similarly calculated for the simulations in case (B), where the top boundary is modelled with the meniscus interface, and have been compared in figures S8a and b in the supporting materials. The agreement at the times when the iso-surface attains its maximum surface area is better for that case, due to less interaction of the iso-surface with the wall (see figure S7 in the supporting materials).

For a closer analysis we disentangle the effects leading to diffusion enhancement, followed by faster propagation of the front after transition to convection. Equation 3.12 encompasses the two key parameters contributing to the front dynamics; the relative area of the iso-surface,  $A_{iso}/A_0$ , multiplied by the averaged local propagation velocity,  $\bar{v}_n$ , which together define the rate of diffusive transport across the front interface. Any changes in the front surface area or the concentration gradients (diffusive fluxes) in its vicinity can ultimately alter the diffusion rate across the front iso-surface and impact the propagation velocity. Therefore, we plot the time evolution of  $A_{iso}/A_0$  and  $\bar{v}_n$  in figures 3.13(c) and (d), respectively. The front velocity in the pure diffusion problem, which is solely equivalent to  $\bar{v}_n$  (the front remains always flat and thus the relative surface area is unity in equation 3.12), has analytically been obtained from equation 3.4 as  $v_{n,d} = K_f D(t - t_0)^{-1/2}$  and plotted in figure 3.13d. The relative local propagation velocity of the front with respect to that of the pure diffusion problem, i.e.,  $\bar{v}_n/v_{n,d}$ , is also shown in the inset.

Up to transition time, the front iso-surface remains flat, meaning that the relative surface area does not change in this period and thus remains equal to unity. Similarly, the local propagation velocity follows that of the pure diffusion problem as they are essentially the same before the onset of convection, which leads to a relative local propagation velocity equal to unity, as indicated in the inset. The value of  $\bar{v}_n$  decreases within this period, complying to the front dynamics governed by diffusion regime, i.e.  $dz_m/dt \sim t^{-1/2}$ .

Once convection sets in, the underlying flow field distorts the front intensely, as demonstrated in figures 3.9 and 3.12 around  $t \approx 1$  min. This leads to a significant increase in the surface area of the front, see figure 3.13(c), as well as the adjacent concentration gradients,  $\nabla C$ . The latter is reflected in local propagation velocity when it increases after  $t \approx 1$  min in figure 3.13d ( $\bar{v}_n \sim \nabla^2 C$  and  $\nabla^2 C$  is higher in the vicinity of a stretched interface since  $\nabla C$  has non-zero components in lateral directions). As a result, lateral diffusive fluxes across the interface intensify, which act against the further convolution of the front and lead to a re-flattening process, once a maximum surface area is reached. Consequently, the front surface area and local propagation velocity drop after the maximum distortion until a "steady state" is reached (figures 3.13(c) and (d)). They determine the trend of the total propaga-

tion velocity shown in figure 3.13(b). At this point, the advective fluxes causing the front distortion approximately equal the lateral diffusive fluxes across the interface which leads to much lower temporal variations afterwards.

The equilibrium state is even more evident in the simulations for case (B), with the meniscus interface at the top boundary. In these simulations, the distortion of the front is less pronounced and therefore the front interface has enough time to almost completely go through the re-flattening process, as shown in figure 3.21 at  $t=1737$  s. Moreover, the relative front surface area and local propagation velocity, depicted in figures 3.22(c) and (d), approach the values close to unity, meaning that the dynamics pertinent to the pure-diffusion regime are almost recovered and the front interface propagates with a nearly constant velocity at late times.

Therefore, although the emerged flow field after the onset of convection does not directly impact the mean location of the front, it does play a significant role in amplifying the carbon dioxide diffusion rate across the front interface through increasing the front interface surface area and local concentration gradients. The front iso-surface accelerates remarkably after the onset of convection and the front trajectory after the onset can still be described approximately with a relation similar to the analytical solution of a pure-diffusion problem as described in equation 3.4, albeit with an effective diffusion constant  $D_{\text{eff}}$ , which accounts for the enhanced diffusion observed in the convective regime. For the case specifically studied here, the post-transition front trajectory, namely the enhanced diffusive regime, can be approximated with  $D_{\text{eff}} = 8.25D$ , plotted for comparison with the data obtained via experiments and numerical simulations in figures 3.6 and 3.8, respectively.

## 3.7 Conclusions

We have investigated the dissolution and subsequent propagation dynamics of carbon dioxide gas into a liquid barrier confined to a vertical glass cylinder, both experimentally and through direct numerical simulations. Replacing the ambient air above the cylinder with a  $\text{CO}_2$  atmosphere, induces the dissolution of  $\text{CO}_2$  into the liquid barrier. Initially, the dissolution of  $\text{CO}_2$  results in the formation of a  $\text{CO}_2$ -rich water layer, which is denser in comparison to pure water, at the top gas-liquid interface. While initially stable, continued dissolution of  $\text{CO}_2$  into the water barrier results in the layer becoming gravitationally unstable, leading to the onset of buoyancy driven convection and, consequently, the shedding of a buoyant plume. By adding sodium fluorescein, a pH-sensitive fluorophore, we directly visualise the dissolution and propagation of the  $\text{CO}_2$  across the liquid barrier. Tracking the  $\text{CO}_2$  front propagation in time allows us to define two clear propagation regimes.

At first, before the onset of convection, the growth dynamics of the boundary layer are purely governed by diffusion (the diffusive regime). The Rayleigh number continues to increase until it reaches the critical value of our system of  $Ra_{z_1} = (3.30 \pm 0.6) \times 10^3$  and convection starts. After the onset of convection, the propagation dynamics of the CO<sub>2</sub> front appear to also behave diffusively, albeit with an effective diffusion coefficient 8.5 times larger than expected for CO<sub>2</sub> in water. This enhanced diffusive regime remains throughout the experiments, until the system either reaches a “steady state”, at which point the front propagates at a constant velocity until it reaches the bottom interface, or becomes unstable, leading to the shedding of an upwelling plume and accelerating towards a higher velocity.

Using direct numerical simulations, we have uncovered the roots of the observed propagation mechanics. Initially, before the onset of convection, the simulations show that the relative surface area of the CO<sub>2</sub> front does not increase and the local propagation velocity follows the expected trend for a purely diffusive problem. After the onset of convection, first the relative surface area and local concentration gradients incorporated in the averaged local propagation velocity on the front,  $\bar{v}_n$ , concurrently increase due to the emerging local fluid flow. As a result the diffusive transport rate across the front interface is remarkably amplified, leading to much faster propagation velocity of the CO<sub>2</sub> front. In the meantime, increased lateral diffusive fluxes across the distorted interface act as a competing mechanism against the advective fluxes and further convolution of the front. This triggers the re-flattening process of the CO<sub>2</sub> front as a result of which the front surface area and local propagation velocity drop and a “steady state is reached. At this point, the advective effects causing the front distortion approximately equal the diffusive flattening of the interface, resulting in the front propagating at a seemingly constant velocity. Therefore, the front trajectory after the onset can still be described with a relation similar to the analytical solution of a pure-diffusion problem, albeit with an effective diffusion 8.5 times higher than expected for CO<sub>2</sub> in water.

Our findings offer insight into the mass-transfer effects encountered in laterally confined CO<sub>2</sub> sequestration operations, as well as microfluidic or microreactor devices comprising segmented gas-liquid systems or density-changing solutes. Such a better understanding of the formation and propagation dynamics of the convective plume can uncover previously undiscovered mechanics pertaining to the dissolution and mixing of chemical species in a variety of applications. An interesting and relevant route to follow is the extension of our work to vessels with larger lateral extension (larger aspect ratio), where many plumes drive the downwards transport of the flow. Based on the results of Shishkina [206], we expect a strong increase of the transport with increasing aspect ratio. For very large aspect ratios, the unconfined

limit of CO<sub>2</sub> sequestration will be approximated [178].

## 3.8 Appendix

### 3.8.1 Intensity profile normalisation and concentration calibration

The grayvalue (green channel value) profile  $G(z, t)$  of the raw fluorescence images is first normalized by the initial profile, i.e. without significant amounts of CO<sub>2</sub> present in the liquid, to correct for the spatial inhomogeneity of the LED lighting. Thus,  $I = G(z, t)/G(z, 0)$  is the normalized apparent intensity. However,  $I$  decays exponentially in time due to photobleaching. We assume that rate of change of the  $I$  is the sum of the rate of change due to CO<sub>2</sub>-quenching (pH change) and the rate of change imposed by photobleaching:

$$\frac{dI}{dt} = \frac{d\hat{I}}{dt} - \beta\hat{I}, \quad (3.13)$$

where  $\hat{I}$  denotes the true intensity (corrected for photobleaching) and  $\beta$  is the photobleaching rate constant. It follows that  $\beta$  is in fact pH-dependent, i.e.,  $\beta = \beta(\hat{I}^*)$ . We approximate the dependence to be linear as  $\beta = a\hat{I} + b$ , where coefficients  $a$  and  $b$  are obtained experimentally, e.g. from the intensity decay rate within the CO<sub>2</sub>-free region in the water column in combination with measurements from purely diffusive experiments (where the cell is inverted). We find  $a = -5.0 \pm 0.2 \times 10^{-4} \text{ s}^{-1}$  and  $b = 6.8 \pm 0.3 \times 10^{-4} \text{ s}^{-1}$  across the 12 experiments. The corrected intensity at any location  $z$  can be solved for iteratively by linearising (3.13) as follows:

$$\hat{I}(z)_{n+1} - \hat{I}(z)_n = I_{n+1}(z) - I_n(z) + \beta_n(z)\hat{I}_n(z)\Delta t, \quad (3.14)$$

where subscript  $n$  refers to the current time step or image frame and  $\Delta t$  is the time difference between consecutive time steps. Finally, the corrected intensity is then renormalised by the maximum and minimum intensity values (within the central region far from the shadowing effect of the meniscii or solid boundaries). Thus,

$$I^*(z, t) = \frac{\hat{I}(z, t) - \min(\hat{I})}{\max(\hat{I}) - \min(\hat{I})}, \quad (3.15)$$

keeping in mind that  $\max(\hat{I}) \approx 1.0$  and  $\min(\hat{I}) \approx 0.4$  are quite close (ideally identical) for all experiments.

For the concentration calibration, we relate the intensity profile of a diffusive experiment to the self-similar profile  $C/C_{sat} = \text{erfc}(\eta)$ , with  $\eta = z/\sqrt{4Dt}$ . Consequently, the intensity profiles evolves self-similarly too:  $I^*(z, t)$  collapse into the

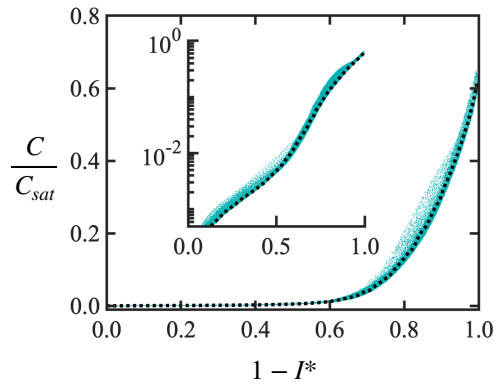


Figure 3.14: Calibration curve (dotted line), which relates the normalised intensity  $I^*$  to the dimensionless concentration,  $C/C_{sat}$  under our particular experimental conditions. The blue data points are measurements of the self-similar intensity profile  $I^*(\eta)$  of the calibration (pure diffusion) experiment, for which  $C(\eta)/C_{sat} = \text{erfc}(\eta)$ . Inset: same calibration curve plotted in semi-logarithmic axes.

same curve  $I^*(\eta)$ . Thus, the calibration function  $C/C_{sat} = F(1 - I^*)$  can be obtained by a monotonic fit on a plot of  $\text{erfc}(\eta)$  vs.  $1 - I^*(\eta)$ , which is provided in figure 3.14.

### 3.8.2 Supporting material

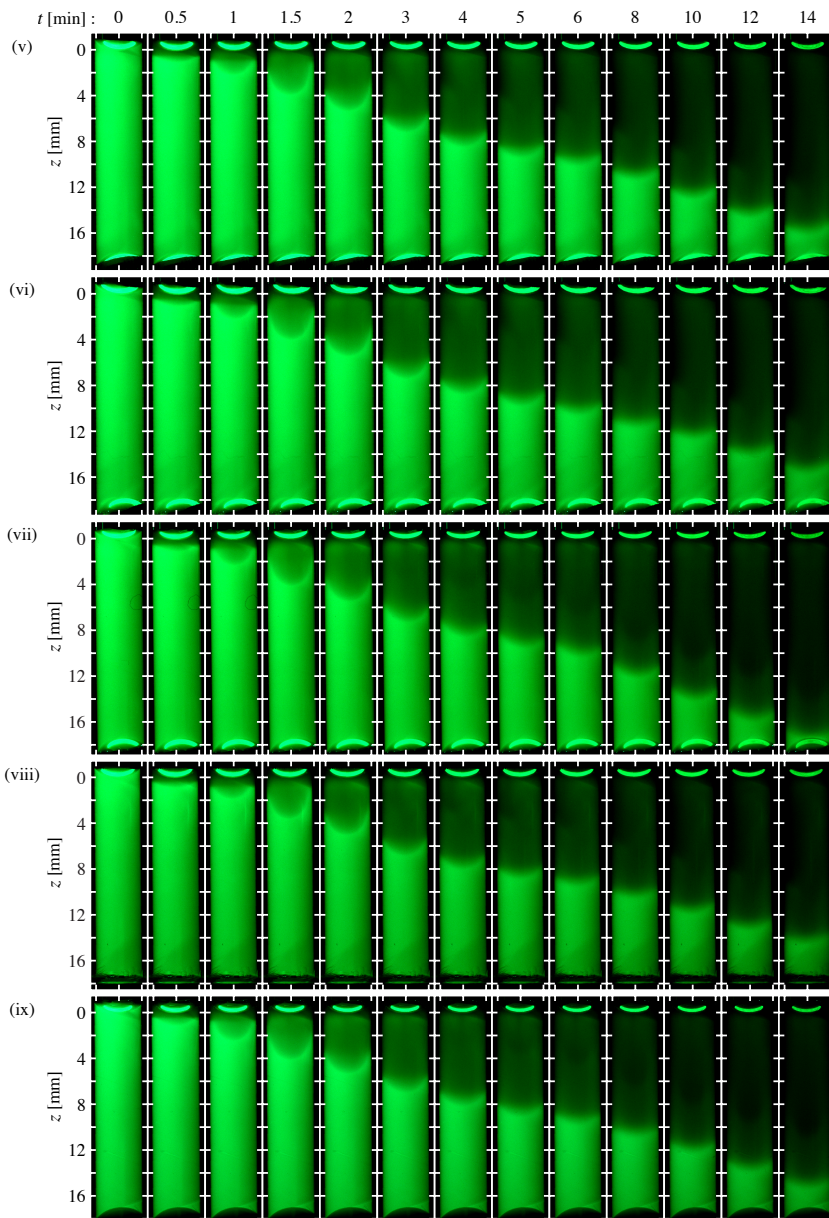


Figure 3.15: Snapshots of experiments (v–ix) where no mode transition is observed. Note that the bottom interface of experiments (v–vii) is liquid–gas, for (viii) it is liquid–solid, and for (ix) it is liquid–liquid (water–n-hexadecane). See caption of figure 3.2 for more details.

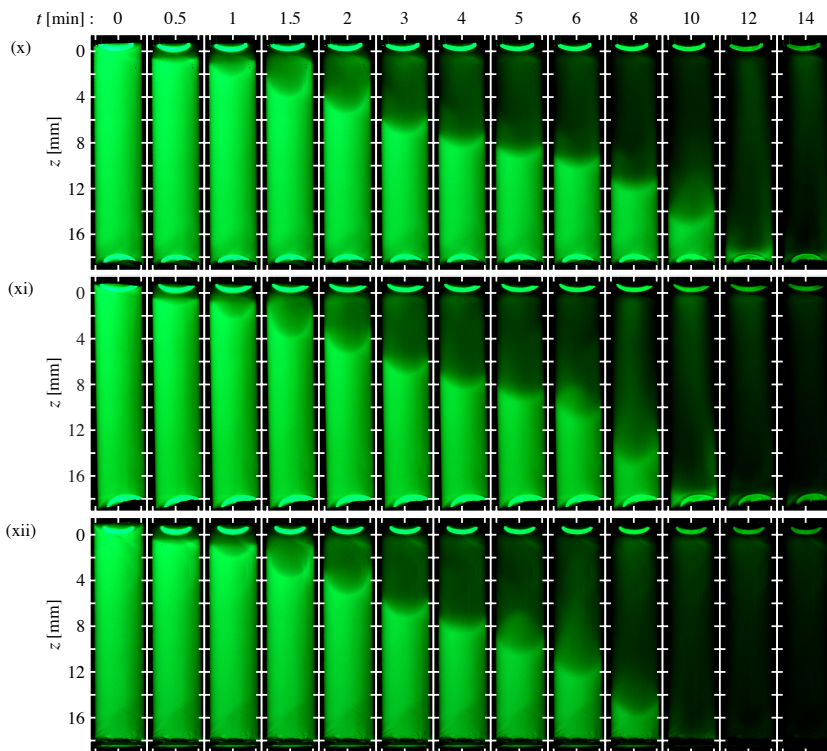


Figure 3.16: Snapshots of experiments (x-xii) where mode transition is present. Note that the bottom interface of experiments (x, xi) is liquid–gas, for (xii) it is liquid–solid. See caption of figure 3.2 for more details.

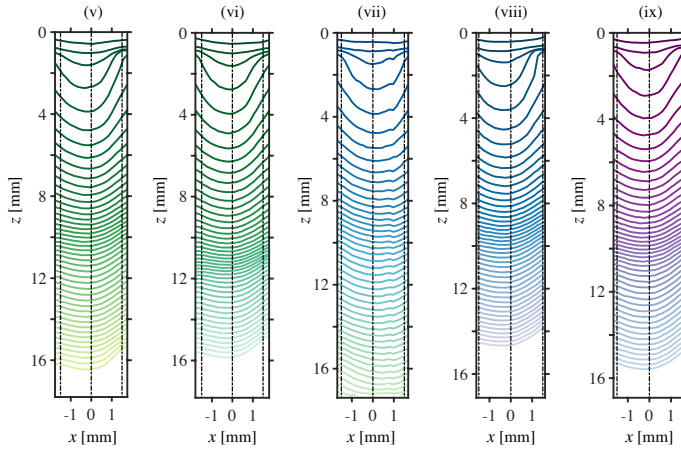


Figure 3.17: Propagation of the projected front surface corresponding for experiments (v–ix)]. See caption of figure 3.3 for details.

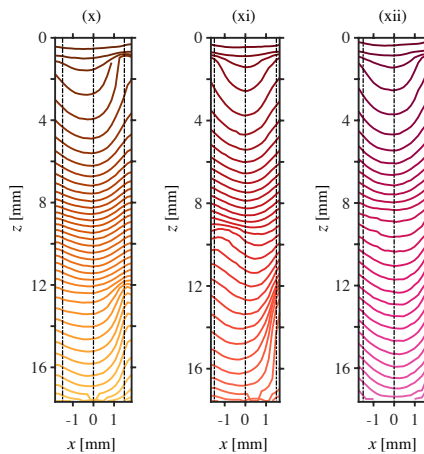


Figure 3.18: Propagation of the projected front surface of experiments (x–xii). See caption of figure 3.3 for details.

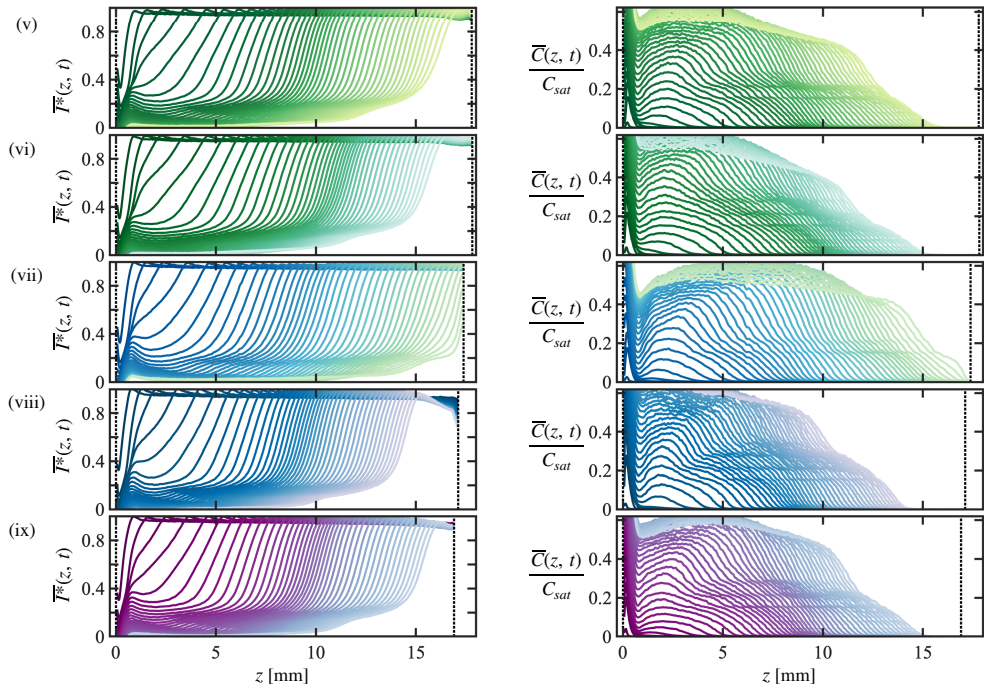


Figure 3.19: (a) Normalised intensity profiles (left panels) and corresponding tentative concentration profiles (right panels) for experiments (v–ix). See caption of figures 3.4 for details.

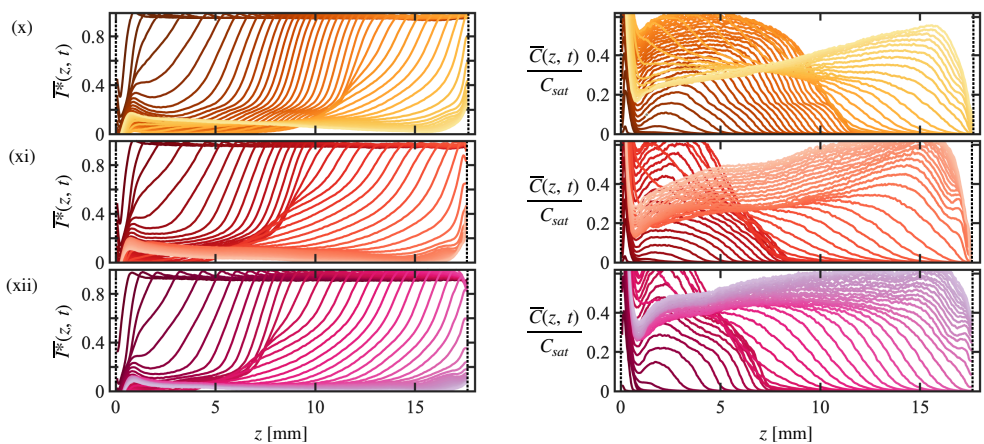


Figure 3.20: (a) Normalised intensity profiles (left panels) and corresponding tentative concentration profiles (right panels) for experiments (x–xii). See caption of figures 3.4 for details.

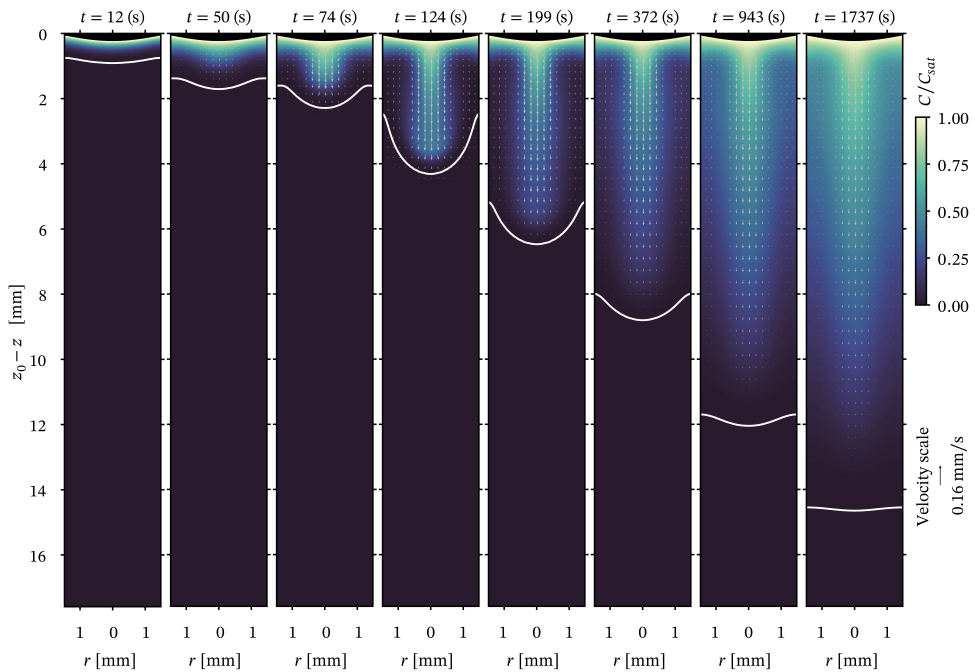


Figure 3.21: Time evolution of carbon dioxide concentration obtained from numerical simulations for case (B) where the top boundary is modelled as a meniscus interface. The white contour-lines show the front profile associated with  $C_f/C_{sat} = 0.25\%$ . Vectors denote the velocity field, the scaling of which has been provided in the figure.

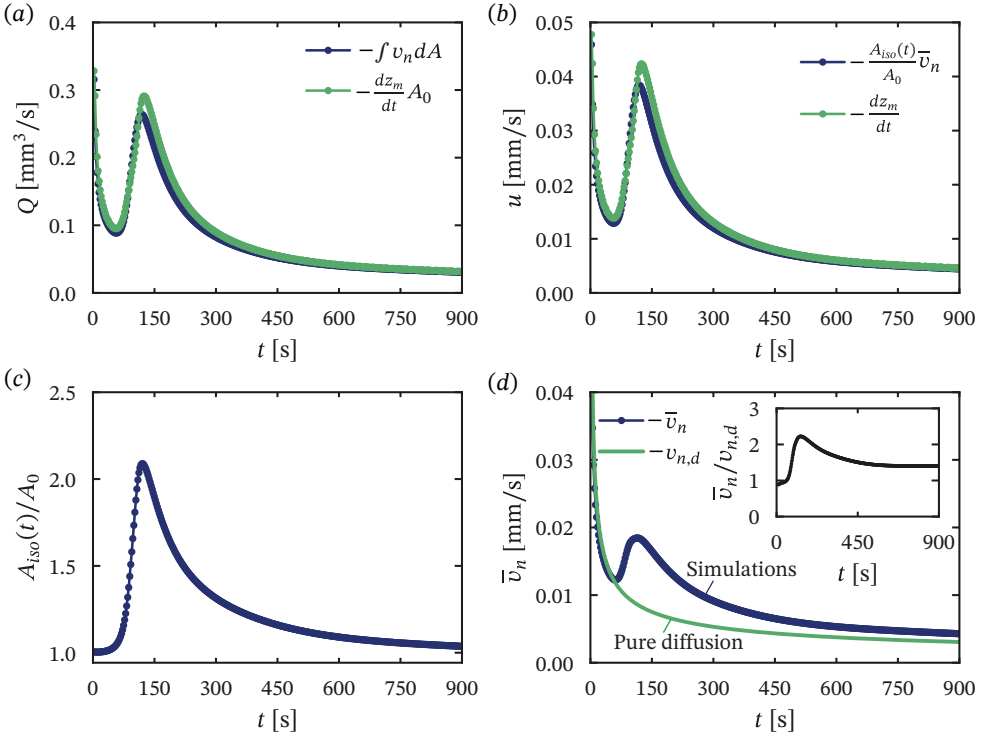


Figure 3.22: For case (B). (a) Volumetric flux  $Q$  of the local propagation velocity  $v_n$  across the front iso-surface, compared to the rate of change in the mean volume above the iso-surface,  $A_0 dz_m/dt$ . (b) Front propagation velocity computed from the time evolution of the cross-sectional average of the 3D iso-surface,  $dz_m/dt$ , and from the product of the relative surface area and averaged local propagation velocity.  $dz_f/dt$  is provided where  $z_f$  is the front trajectory obtained from the horizontally-averaged concentration profile in 2D slices, in accordance with the front tracking approach in experiments. (c) Relative surface area of the iso-surface with respect to the cross sectional area of the cylinder,  $A_0$ . (d) Temporal evolution of the averaged local propagation velocity,  $\bar{v}_n$ , of the iso-surface.  $\bar{v}_n$  for the iso-surface in pure-diffusion problem, compared to the pure diffusive case,  $v_{n,d}$ , where it equals the front propagation velocity  $dz_m/dt = K_f [D(t - t_0)]^{-1/2}$ , with  $K_f$  defined in (3.5). The ratio  $\bar{v}_n/v_{n,d}$ , is shown in the inset.

3

# Conclusions

Given the increasing urge for energy transition from carbon-intensive, non-renewable and finite fossil fuels to sustainable power resources, it is indispensable to devise reliable 'green' and yet scalable technologies to slow down the unprecedented effects of climate change. Hydrogen production through water electrolysis and Carbon Capture and Storage (CCS) in geological formations are envisioned as promising technologies to reduce anthropogenic emissions. Yet challenges remain to increase the scalability of these technologies for utilization in different energy sectors.

In this thesis we aim to understand and unravell new physics which vigorously control/limit the performance of such systems. The shortcomings of water electrolyzers highly pertains to the formation of gas bubbles which limits the reaction rate and causes cell overpotential, i.e., the required energy for continuing the electrolysis process is increased. In the other hand, secure and long-term storage of carbon dioxide in geological reservoirs is a difficult task given the complicated mass transfer processes involved in the  $\text{CO}_2$  dissolution into the brine. Therefore, our goal is to identify and quantify the controlling mass transfer mechanisms in water electrolyzers subjected to bubble formation and evolution and reveal the intricate dynamics of  $\text{CO}_2$  penetrative dissolution in water.

In **chapter 1**, our comprehensive experimental and numerical analysis definitively confirmed the significance of solutal convection in the evolution of bubbles during water electrolysis. This was corroborated by excellent agreement of bubble growth and dissolution rate obtained from experiments and numerical simulations, when the natural convection due to density gradients in the solution was considered in addition to diffusion. We further observe that the presence of the bubbles promotes the instabilities of the diffusion boundary layer. Defining a transient  $Gr$  based on the boundary layer thickness on the electrode, the critical threshold of transition to convection is lowered from  $Gr_c \approx 1$  for the cases w/o bubble to  $Gr_c \approx 0.75$  for a set-up with bubble spacing of  $S = 3$  mm. In setups with tighter

spacing between the bubbles the critical Grashof number increases again signalling the overkilling effects of bubble on natural convection emergence. We also revealed the strong dependance of flow patterns on the bubble spacing and their arrangement in clustered network on the electrode. Different flow patterns caused by the design parameters remarkably impact the growth and dissolution dynamics of the bubbles. Single-phase convection can only be the rate-controlling mechanism at low values of current density where the fractional bubble coverage of the electrode is not so high and bubble growth is very slow. This allows the density gradients in the electrode boundary layer to develop to a sufficient extent necessary for triggering the instabilities. However at high values of current density a strong flow is established in the solution as a result of microconvection induced by bubble growth as well as two-phase buoyancy-driven convection owing to the density variations of gas-in-liquid dispersion. Such flows relax the density gradients in the liquid phase close to the electrode by enhancing the mixing in the electrolyte solution and, therefore, suppress the single-phase convection. In case that all mechanism can coexist, the strong flow caused by bubble rise in the electrolyte will most likely prevail the single-phase natural convection.

In **chapter 2**, overlooking solutal or thermal natural convection we aim to identify the mass transfer mechanism which controls the transport rate at gas-evolving electrodes subjected to consecutive growth and ascent of the bubbles. Using a finite difference solver for the carrier phase and Immersed Boundary Method for the bubble we attempt to numerically mimic the relevant physics in such system and quantify the mass transfer rate at the electrode. Since the transport of hydrogen from the electrode occurs within two different mechanisms, namely the transfer of the dissolved gas to the dispersed phase and bulk electrolyte, we additionally account for this and quantify the mass transfer rate to the bubble under various operating conditions. To elucidate the main effects, we varied the current density 3 order of magnitudes for different prescribed bubble size and spacing, incorporated in fractional bubble coverage of the electrode surface,  $\Theta$ .

We quantified the cumulative hydrogen transport from the electrode surface (via solution mixture as dissolved gas and within the gas bubble) in figure 2.13 and that of electrolyte transport to the electrode in figure 2.14. Drawing an analogy to single-phase heat and mass transfer problems, the buoyancy-driven convection induced by consecutively departing bubbles from the electrode surface was identified as the governing mass transfer mechanism. This finding was corroborated by a unique power law of  $Sh_{j,e} = 1.0 (GrSc_j)^{1/3}$  found to be descriptive for both hydrogen and electrolyte transport at the electrode. For the electrolyte, a factor of  $(1 - \Theta)$  to compensate for the surface blockage effect reduces, yet does not fully

eliminate, deviations from the power law at low  $Gr$ . No such deviations occur at high  $Gr$ , at which also most of the gas transport is in the dissolved state. Furthermore, we found that the bubble growth dynamics are connected to the hydrogen transport rate from the electrode, such that it switches from diffusion-controlled,  $R = \mathcal{B}t^{1/2}$ , to reaction-controlled,  $R = \mathcal{B}t^{1/3}$ , regime as  $Gr$  ramps up with increasing current density and bubble coverage of the electrode (figure 2.15). This transition was attributed to the high transport rate of the hydrogen from electrode surface at large  $Gr$  which prevailed over the gas production rate in the reaction, forcing the Faraday's law to control the bubble growth [99]. Next, we quantified the hydrogen transport to the bubble by taking into account the driving force of the bubble growth, namely Jakob number  $Ja$  (2.28). This parameter was reformulated based on the simulation inputs and gas-evolution efficiency, resulting in a unique expression for mass transfer into the bubble given by (2.32). Eventually, performing a scaling analysis on mass transfer rates at the electrode and bubble interface we found the connection between gas-evolution efficiency,  $f_G$ , and these processes and ultimately established an asymptotic solution for  $f_G$  given by (2.35) and (2.36). Our findings can provide insight into the mass transfer rates at gas-evolving electrodes mostly prevalent in water-electrolyzers by knowing the current density and typical size and inter-spacing of the bubbles, i.e. bubble coverage of the electrode, from the in-situ measurements.

In **chapter 3**, we conducted an investigation on the dissolution and propagation dynamics of carbon dioxide gas in a liquid barrier confined to a vertical glass cylinder. This was done through experimental observations and direct numerical simulations. By replacing the ambient air above the cylinder with a  $\text{CO}_2$  atmosphere, we induced the dissolution of  $\text{CO}_2$  into the liquid barrier. Initially, the dissolution resulted in the formation of a dense  $\text{CO}_2$ -rich water layer at the top gas-liquid interface. However, as the dissolution continued, this layer became gravitationally unstable, leading to buoyancy-driven convection and the eventual shedding of a buoyant plume. To visualize the dissolution and propagation of  $\text{CO}_2$  across the liquid barrier, we added sodium fluorescein, a pH-sensitive fluorophore. Tracking the time-dependent propagation of the  $\text{CO}_2$  front allowed us to identify two distinct propagation regimes. Initially, before convection begins, the boundary layer grows diffusively. Convection starts when the Rayleigh number reaches a critical value of  $Ra_{z_1} = (3.30 \pm 0.6) \times 10^3$  for our system. After convection starts, the  $\text{CO}_2$  front propagates diffusively with an effective diffusion coefficient 8.5 times larger than expected for  $\text{CO}_2$  in water. This enhanced diffusive behavior persists until the system reaches a steady state or becomes unstable and accelerates with an upwelling plume.

Our findings from direct numerical simulations shed light on the underlying mechanics of CO<sub>2</sub> front propagation. Initially, prior to convection, the simulations reveal that the relative surface area of the front remains constant and the local propagation velocity follows a diffusive trend. However, once convection begins, the local fluid flow causes concurrent increases in the relative surface area and local concentration gradients, leading to a significant amplification of the diffusive transport rate across the front interface. As a result, the CO<sub>2</sub> front propagates at a much faster velocity. Meanwhile, increased lateral diffusive fluxes counteract the advective fluxes, further distorting the front. This triggers a re-flattening process, resulting in a drop in surface area and local propagation velocity, eventually reaching a "steady state". At this point, the advective effects causing front distortion roughly balance the diffusive flattening of the interface, resulting in the front propagating at an apparently constant velocity. Therefore, the post-onset trajectory of the front can still be described by a relation similar to the analytical solution of a pure-diffusion problem, but with an effective diffusion coefficient approximately 8.5 times higher than expected for CO<sub>2</sub> in water. Our findings provide valuable insights into the mass-transfer effects that are encountered in laterally confined CO<sub>2</sub> sequestration operations, as well as in microfluidic or microreactor devices that involve segmented gas-liquid systems or density-changing solutes.

# Bibliography

- [1] J. A. Turner, "Sustainable hydrogen production", *Science* **305**, 972–974 (2004).
- [2] J. Turner, G. Sverdrup, M. K. Mann, P.-C. Maness, B. Kroposki, M. Ghirardi, R. J. Evans, and D. Blake, "Renewable hydrogen production", *Int. J. Energy Res.* **32**, 379–407 (2008).
- [3] J. D. Holladay, J. Hu, D. L. King, and Y. Wang, "An overview of hydrogen production technologies", *Catal. today* **139**, 244–260 (2009).
- [4] I. Dincer, "Green methods for hydrogen production", *Int. J. Hydrog. Energy* **37**, 1954–1971 (2012).
- [5] P. Nikolaidis and A. Poullikkas, "A comparative overview of hydrogen production processes", *Renewable and sustainable energy reviews* **67**, 597–611 (2017).
- [6] F. Dawood, M. Anda, and G. Shafiullah, "Hydrogen production for energy: An overview", *Int. J. Hydrog. Energy* **45**, 3847–3869 (2020).
- [7] A. Ursua, L. M. Gandia, and P. Sanchis, "Hydrogen production from water electrolysis: Current status and future trends", *Proceedings of the IEEE* **100**, 410–426 (2012).
- [8] J. Chi and H. Yu, "Water electrolysis based on renewable energy for hydrogen production", *Chinese Journal of Catalysis* **39**, 390–394 (2018).
- [9] S. Grigoriev, V. Fateev, D. Bessarabov, and P. Millet, "Current status, research trends, and challenges in water electrolysis science and technology", *Int. J. Hydrog. Energy* **45**, 26036–26058 (2020), *progress in Hydrogen Production and Utilization*.

- [10] M. Yu, E. Budiyo, and H. Tüysüz, "Principles of water electrolysis and recent progress in cobalt, nickel, and iron-based oxides for the oxygen evolution reaction", *Angew. Chemie Int. Ed.* **61** (2022).
- [11] T. Burdyny, P. J. Graham, Y. Pang, C. T. Dinh, M. Liu, E. H. Sargent, and D. Sinton, "Nanomorphology-enhanced gas-evolution intensifies CO<sub>2</sub> reduction electrochemistry", *ACS Sustain. Chem. Eng.* **5**, 4031–4040 (2017).
- [12] J. R. Lake, Á. M. Soto, and K. K. Varanasi, "Impact of bubbles on electrochemically active surface area of microtextured gas-evolving electrodes", *Langmuir* **38**, 3276–3283 (2022).
- [13] A. A. Ashaju, J. A. Wood, and R. G. H. Lammertink, "Electrocatalytic reaction-driven flow", *Phys. Rev. Fluids* **6**, 044004 (2021).
- [14] O. DiazMorales, A. Lindberg, V. Smulders, A. Anil, N. Simic, M. Wildlock, G. S. Alvarez, G. Mul, B. Mei, and A. Cornell, "Catalytic effects of molybdate and chromatemolybdate films deposited on platinum for efficient hydrogen evolution", *J. Chem. Technol. Biotechnol.* **98**, 1269–1278 (2023).
- [15] M. Worsley, V. Smulders, and B. Mei, "Controlled synthesis of chromium-oxide-based protective layers on Pt: Influence of layer thickness on selectivity", *Catalysts* **12**, 1077 (2022).
- [16] J. Newman and N. P. Balsara, *Electrochemical systems* (John Wiley & Sons) (2021).
- [17] E. J. F. Dickinson, J. G. Limon-Petersen, and R. G. Compton, "The electroneutrality approximation in electrochemistry", *J. Solid State Electrochem.* **15**, 1335–1345 (2011).
- [18] F. Khalighi, N. G. Deen, Y. Tang, and A. W. Vreman, "Hydrogen bubble growth in alkaline water electrolysis: An immersed boundary simulation study", *Chem. Eng. Sci.* **267**, 118280 (2023).
- [19] P. Slooten, "Departure of vapor- and gas-bubbles in a wide pressure range", Ph.D. thesis, Applied Physics and Science Education, Eindhoven, The Netherlands (1984).
- [20] H. N. Oguz and A. Prosperetti, "Dynamics of bubble growth and detachment from a needle", *J. Fluid Mech.* **257**, 111 (1993).

- [21] S. Jones, G. Evans, and K. Galvin, "Bubble nucleation from gas cavities a review", *Adv. Colloid Interface Sci.* **80**, 27–50 (1999).
- [22] V. M. Volgin and A. D. Davydov, "Natural-convective instability of electrochemical systems: A review", *Russ. J. Electrochem.* **42**, 567–608 (2006).
- [23] V. M. Volgin, A. V. Zhukov, G. N. Zhukova, and A. D. Davydov, "Onset of natural convection in the electrochemical cell with horizontal electrodes under non-steady-state conditions: A numerical study", *Russ. J. Electrochem.* **45**, 1005–1016 (2009).
- [24] V. M. Volgin and A. D. Davydov, "Numerical simulation of natural convection of electrolyte solution with three types of ions in the electrochemical cell with vertical electrodes", *Russ. J. Electrochem.* **46**, 1360–1372 (2010).
- [25] K. Ngamchuea, S. Eloul, K. Tschulik, and R. G. Compton, "Advancing from rules of thumb: quantifying the effects of small density changes in mass transport to electrodes. Understanding natural convection", *Anal. Chem.* **87**, 7226–7234 (2015).
- [26] J. K. Novev and R. G. Compton, "Convective heat transfer in a measurement cell for scanning electrochemical microscopy", *Phys. Chem. Chem. Phys.* **18**, 29836–29846 (2016).
- [27] J. K. Novev and R. G. Compton, "Thermal convection in electrochemical cells. Boundaries with heterogeneous thermal conductivity and implications for scanning electrochemical microscopy", *Phys. Chem. Chem. Phys.* **19**, 12759–12775 (2017).
- [28] J. K. Novev and R. G. Compton, "Natural convection effects in electrochemical systems", *Curr. Opin. Electrochem.* **7**, 118–129 (2018).
- [29] J. Gibbins and H. Chalmers, "Carbon capture and storage", *Energy Policy* **36**, 4317–4322 (2008).
- [30] R. S. Haszeldine, "Carbon Capture and Storage: How green can Black be?", *Science* (80-. ). **325**, 1647–1652 (2009).
- [31] J. Pires, F. Martins, M. Alvim-Ferraz, and M. Simões, "Recent developments on carbon capture and storage: An overview", *Chem. Eng. Res. Des.* **89**, 1446–1460 (2011).

- [32] E. S. Rubin, H. Mantripragada, A. Marks, P. Versteeg, and J. Kitchin, "The outlook for improved carbon capture technology", *Prog. Energy Combust. Sci.* **38**, 630–671 (2012).
- [33] M. E. Boot-Handford, J. C. Abanades, E. J. Anthony, M. J. Blunt, S. Brandani, N. Mac Dowell, J. R. Fernández, M.-C. Ferrari, R. Gross, J. P. Hallett, R. S. Haszeldine, P. Heptonstall, A. Lyngfelt, Z. Makuch, E. Mangano, R. T. J. Porter, M. Pourkashanian, G. T. Rochelle, N. Shah, J. G. Yao, and P. S. Fennell, "Carbon capture and storage update", *Energy Environ. Sci.* **7**, 130–189 (2014).
- [34] M. Bui, C. S. Adjiman, A. Bardow, E. J. Anthony, A. Boston, S. Brown, P. S. Fennell, S. Fuss, A. Galindo, L. A. Hackett, J. P. Hallett, H. J. Herzog, G. Jackson, J. Kemper, S. Krevor, G. C. Maitland, M. Matuszewski, I. S. Metcalfe, C. Petit, G. Puxty, J. Reimer, D. M. Reiner, E. S. Rubin, S. A. Scott, N. Shah, B. Smit, J. P. M. Trusler, P. Webley, J. Wilcox, and N. Mac Dowell, "Carbon capture and storage (CCS): the way forward", *Energy Environ. Sci.* **11**, 1062–1176 (2018).
- [35] T. Wilberforce, A. Olabi, E. T. Sayed, K. Elsaid, and M. A. Abdelkareem, "Progress in carbon capture technologies", *Sci. Total Environ.* **761**, 143203 (2021).
- [36] S. Backhaus, K. Turitsyn, and R. E. Ecke, "Convective instability and mass transport of diffusion layers in a Hele-Shaw geometry", *Phys. Rev. Lett.* **106**, 104501 (2011).
- [37] V. Loodts, L. Rongy, and A. De Wit, "Impact of pressure, salt concentration, and temperature on the convective dissolution of carbon dioxide in aqueous solutions", *Chaos* **24**, 043120 (2014).
- [38] R. N. Moghaddam, B. Rostami, P. Pourafshary, and Y. Fallahzadeh, "Quantification of density-driven natural convection for dissolution mechanism in CO<sub>2</sub> sequestration", *Transp. Porous Media* **92**, 439–456 (2012).
- [39] Y. Gholami, R. Azin, R. Fatehi, S. Osfouri, and A. Bahadori, "Prediction of carbon dioxide dissolution in bulk water under isothermal pressure decay at different boundary conditions", *J. Mol. Liq.* **202**, 23–33 (2015).
- [40] Y. Tang, Z. Li, R. Wang, M. Cui, X. Wang, Z. Lun, and Y. Lu, "Experimental study on the density-driven carbon dioxide convective diffusion in formation water at reservoir conditions", *ACS Omega* **4**, 11082–11092 (2019).

- [41] D. Lohse, "Bubble puzzles: From fundamentals to applications", *Phys. Rev. Fluids* **3**, 1–42 (2018).
- [42] K. Zeng and D. Zhang, "Recent progress in alkaline water electrolysis for hydrogen production and applications", *Prog. Energy Combust. Sci.* **36**, 307–326 (2010).
- [43] A. Angulo, P. van der Linde, H. Gardeniers, M. Modestino, and D. Fernández Rivas, "Influence of bubbles on the energy conversion efficiency of electrochemical reactors", *Joule* **4**, 555–579 (2020).
- [44] A. Sacco, J. Zeng, K. Bejtka, and A. Chiodoni, "Modeling of gas bubble-induced mass transport in the electrochemical reduction of carbon dioxide on nanostructured electrodes", *J. Catal.* **372**, 39–48 (2019).
- [45] *The Future of Hydrogen* (OECD) (2019).
- [46] M. T. de Groot and A. W. Vreman, "Ohmic resistance in zero gap alkaline electrolysis with a Zirfon diaphragm", *Electrochim. Acta* **369** (2021).
- [47] X. Zhao, H. Ren, and L. Luo, "Gas bubbles in electrochemical Gas evolution reactions", *Langmuir* **35**, 5392–5408 (2019).
- [48] J. Eigeldinger and H. Vogt, "The bubble coverage of gas-evolving electrodes in a flowing electrolyte", *Electrochim. Acta* **45**, 4449–4456 (2000).
- [49] H. Vogt and R. J. Balzer, "The bubble coverage of gas-evolving electrodes in stagnant electrolytes", *Electrochim. Acta* **50**, 2073–2079 (2005).
- [50] P. J. Sides and C. W. Tobias, "Primary potential and current distribution around a bubble on an electrode", *J. Electrochem. Soc.* **127**, 288 (1980).
- [51] J. Dukovic and C. W. Tobias, "The Influence of attached bubbles on potential drop and current distribution at gas-evolving electrodes", *J. Electrochem. Soc.* **134**, 331 (1987).
- [52] T. Kadyk, D. Bruce, and M. Eikerling, "How to enhance gas removal from porous electrodes?", *Sci. Rep.* **6**, 1–14 (2016).
- [53] C. Brussieux, P. Viers, H. Roustan, and M. Rakib, "Controlled electrochemical gas bubble release from electrodes entirely and partially covered with hydrophobic materials", *Electrochim. Acta* **56**, 7194–7201 (2011).

- [54] W. Xu, Z. Lu, X. Sun, L. Jiang, and X. Duan, "Superwetting electrodes for gas-involving electrocatalysis", *Acc. Chem. Res.* **51**, 1590–1598 (2018).
- [55] P. Peñas, P. van der Linde, W. Vijselaar, D. van der Meer, D. Lohse, J. Huskens, H. Gardeniers, M. A. Modestino, and D. F. Rivas, "Decoupling gas evolution from water-splitting electrodes", *J. Electrochem. Soc.* **166**, H769–H776 (2019).
- [56] N. Pande, G. Mul, D. Lohse, and B. Mei, "Correlating the short-time current response of a hydrogen evolving nickel electrode to bubble growth", *J. Electrochem. Soc.* **166**, E280—E285 (2019).
- [57] X. Yang, F. Karnbach, M. Uhlemann, S. Odenbach, and K. Eckert, "Dynamics of single hydrogen bubbles at a platinum microelectrode", *Langmuir* **31**, 8184–8193 (2015).
- [58] P. van der Linde, Á. Moreno Soto, P. Peñas-López, J. Rodríguez-Rodríguez, D. Lohse, H. Gardeniers, D. Van Der Meer, and D. Fernández Rivas, "Electrolysis-driven and pressure-controlled diffusive growth of successive bubbles on microstructured surfaces", *Langmuir* **33**, 12873–12886 (2017).
- [59] X. Yang, D. Baczymalski, C. Cierpka, G. Mutschke, and K. Eckert, "Marangoni convection at electrogenerated hydrogen bubbles", *Phys. Chem. Chem. Phys.* **20**, 11542–11548 (2018).
- [60] J. Massing, G. Mutschke, D. Baczymalski, S. S. Hossain, X. Yang, K. Eckert, and C. Cierpka, "Thermocapillary convection during hydrogen evolution at microelectrodes", *Electrochim. Acta* **297**, 929–940 (2019).
- [61] S. S. Hossain, G. Mutschke, A. Bashkatov, and K. Eckert, "The thermocapillary effect on gas bubbles growing on electrodes of different sizes", *Electrochim. Acta* **353**, 136461 (2020).
- [62] A. M. Meulenbroek, A. W. Vreman, and N. G. Deen, "Competing Marangoni effects form a stagnant cap on the interface of a hydrogen bubble attached to a microelectrode", *Electrochim. Acta* **385**, 138298 (2021).
- [63] A. Mani and K. M. Wang, "Electroconvection near electrochemical interfaces: Experiments, modeling, and computation", *Annu. Rev. Fluid Mech.* **52**, 509–529 (2020).
- [64] N. Pande, J. A. Wood, G. Mul, D. Lohse, B. T. Mei, and D. Krug, "Electroconvective instability in water electrolysis: an evaluation of electroconvective patterns and their onset features", *Phys. Rev. Appl.* **16**, 1 (2021).

- [65] K. Obata, R. Van De Krol, M. Schwarze, R. Schomäcker, and F. F. Abdi, "In situ observation of pH change during water splitting in neutral pH conditions: Impact of natural convection driven by buoyancy effects", *Energy Environ. Sci.* **13**, 5104–5116 (2020).
- [66] R. Babu and M. K. Das, "Experimental studies of natural convective mass transfer in a water-splitting system", *Int. J. Hydrogen Energy* **44**, 14467–14480 (2019).
- [67] O. S. Heavens, *Optical properties of thin solid films*, volume 23 (Dover Publications) (1955).
- [68] Á. Moreno Soto, A. Prosperetti, D. Lohse, and D. Van Der Meer, "Gas depletion through single gas bubble diffusive growth and its effect on subsequent bubbles", *J. Fluid Mech.* **831**, 474–490 (2017).
- [69] P. Penás-López, Á. Moreno Soto, M. A. Parrales, D. Van Der Meer, D. Lohse, and J. Rodríguez-Rodríguez, "The history effect on bubble growth and dissolution. Part 2. Experiments and simulations of a spherical bubble attached to a horizontal flat plate", *J. Fluid Mech.* **820**, 479–510 (2017).
- [70] M. D. Morris and J. J. Lingane, "The effect of electrical migration on the chronopotentiometric transition time", *J. Electroanal. Chem.* **6**, 300–313 (1963).
- [71] H. Vogt, "Thermal effect on liquid-phase free convection at gas evolving electrodes", *Int. J. Heat Mass Transf.* **36**, 4115–4121 (1993).
- [72] S. Takagi and Y. Matsumoto, "Surfactant effects on bubble motion and bubbly flows", *Annu. Rev. Fluid Mech.* **43**, 615–636 (2011).
- [73] M. A. Edwards, H. S. White, and H. Ren, "Voltammetric determination of the stochastic formation rate and geometry of individual H<sub>2</sub>, N<sub>2</sub>, and O<sub>2</sub> bubble nuclei", *ACS Nano* **13**, 6330–6340 (2019).
- [74] Y. Liu, C. Jin, Y. Liu, K. H. Ruiz, H. Ren, Y. Fan, H. S. White, and Q. Chen, "Visualization and quantification of electrochemical H<sub>2</sub> bubble nucleation at Pt, Au, and MoS<sub>2</sub> substrates", *ACS Sensors* **6**, 355–363 (2021).
- [75] L. J. Janssen and J. G. Hoogland, "The effect of electrolytically evolved gas bubbles on the thickness of the diffusion layer-II", *Electrochim. Acta* **18**, 543–550 (1973).

- [76] H. Vogt, "On the gas-evolution efficiency of electrodes I - Theoretical", *Electrochim. Acta* **56**, 1409–1416 (2011).
- [77] H. Vogt and K. Stephan, "Local microprocesses at gas-evolving electrodes and their influence on mass transfer", *Electrochim. Acta* **155**, 348–356 (2015).
- [78] O. R. Enríquez, C. Sun, D. Lohse, A. Prosperetti, and D. Van Der Meer, "The quasi-static growth of CO<sub>2</sub> bubbles", *Journal of Fluid Mechanics* **741**, R1 (2014).
- [79] K. K. Tan and R. B. Thorpe, "The onset of convection caused by buoyancy during transient heat conduction in deep fluids", *Chem. Eng. Sci.* **51**, 4127–4136 (1996).
- [80] E. Karatay, M. B. Andersen, M. Wessling, and A. Mani, "Coupling between buoyancy forces and electroconvective instability near ion-selective surfaces", *Phys. Rev. Lett.* **116**, 33–37 (2016).
- [81] J. C. De Valença, A. Kurniawan, R. M. Wagterveld, J. A. Wood, and R. G. H. Lammertink, "Influence of Rayleigh-Bénard convection on electrokinetic instability in overlimiting current conditions", *Phys. Rev. Fluids* **2**, 1–13 (2017).
- [82] J. J. Van Tassel and C. A. Randall, "Ionic gradients at an electrode above the equilibrium limit current. 2. Transition to convection", *J. Phys. Chem. C* **111**, 3349–3357 (2007).
- [83] E. M. Sparrow, R. J. Goldstein, and V. K. Jonsson, "Thermal instability in a horizontal fluid layer: Effect of boundary conditions and non-linear temperature profile", *J. Fluid Mech.* **18**, 513–528 (1964).
- [84] K. K. Tan and R. B. Thorpe, "Gas diffusion into viscous and non-Newtonian liquids", *Chem. Eng. Sci.* **47**, 3565–3572 (1992).
- [85] A. Bejan, *Heat Transfer* (John Wiley & Sons, Inc.) (1993).
- [86] O. Carrier, N. Shahidzadeh-Bonn, R. Zargar, M. Aytouna, M. Habibi, J. Eggers, and D. Bonn, "Evaporation of water: Evaporation rate and collective effects", *J. Fluid Mech.* **798**, 774–786 (2016).
- [87] G. Laghezza, E. Dietrich, J. M. Yeomans, R. Ledesma-Aguilar, E. S. Kooij, H. J. Zandvliet, and D. Lohse, "Collective and convective effects compete in patterns of dissolving surface droplets", *Soft Matter* **12**, 5787–5796 (2016).

- [88] K. L. Chong, Y. Li, C. S. Ng, R. Verzicco, and D. Lohse, “Convection-dominated dissolution for single and multiple immersed sessile droplets”, *J. Fluid Mech.* **892**, A21 (2020).
- [89] P. Van Der Linde, P. Peñas-López, Á. Moreno Soto, D. Van Der Meer, D. Lohse, H. Gardeniers, and D. Fernández Rivas, “Gas bubble evolution on microstructured silicon substrates”, *Energy Environ. Sci.* **11**, 3452–3462 (2018).
- [90] D. Lohse and X. Zhang, “Physicochemical hydrodynamics of droplets out of equilibrium”, *Nat. Rev. Phys.* **2**, 426–443 (2020).
- [91] E. P. van der Poel, R. Ostilla-Mónico, J. Donners, and R. Verzicco, “A pencil distributed finite difference code for strongly turbulent wall-bounded flows”, *Comput. Fluids* **116**, 10–16 (2015).
- [92] R. Verzicco and P. Orlandi, “A Finite-Difference scheme for three-dimensional incompressible flows in cylindrical coordinates”, *J. Comput. Phys.* **123**, 402–414 (1996).
- [93] M. D. de Tullio and G. Pascazio, “A moving-least-squares immersed boundary method for simulating the fluidstructure interaction of elastic bodies with arbitrary thickness”, *J. Comput. Phys.* **325**, 201–225 (2016).
- [94] V. Spandan, D. Lohse, M. D. de Tullio, R. Ostilla-Mónico, R. Verzicco, V. Meschini, and G. Querzoli, “A parallel interaction potential approach coupled with the immersed boundary method for fully resolved simulations of deformable interfaces and membranes”, *J. Comput. Phys.* **348**, 567–590 (2017).
- [95] H. Vogt, “Prediction of the isothermal expansion coefficient of electrolyte solutions containing dissolved ases”, *Berichte der Bunsengesellschaft für Phys. Chemie* **96**, 158–162 (1992).
- [96] K. Qian, Z. D. Chen, and J. J. Chen, “Bubble coverage and bubble resistance using cells with horizontal electrode”, *J. Appl. Electrochem.* **28**, 1141–1145 (1998).
- [97] G. F. Swiegers, R. N. Terrett, G. Tsekouras, T. Tsuzuki, R. J. Pace, and R. Stranger, “The prospects of developing a highly energy-efficient water electrolyser by eliminating or mitigating bubble effects”, *Sustain. Energy Fuels* **5**, 1280–1310 (2021).

- [98] G. B. Darband, M. Aliofkhaezai, and S. Shanmugam, "Recent advances in methods and technologies for enhancing bubble detachment during electrochemical water splitting", *Renew. Sustain. Energy Rev.* **114**, 109300 (2019).
- [99] I. Roušar and V. Cezner, "Transfer of mass or heat to an electrode in the region of hydrogen evolution theory", *Electrochim. Acta* **20**, 289–293 (1975).
- [100] W. Fritz, "Berechnung des maximalvolumens von dampfblasen", *Physik. Zeitschr* **36**, 379–384 (1935).
- [101] R. Iwata, L. Zhang, Z. Lu, S. Gong, J. Du, and E. N. Wang, "How coalescing bubbles depart from a wall", *Langmuir* **38**, 4371–4377 (2022).
- [102] K. Stephan and H. Vogt, "A model for correlating mass transfer data at gas evolving electrodes", *Electrochim. Acta* **24**, 11–18 (1979).
- [103] L. Janssen and E. Barendrecht, "The effect of electrolytic gas evolution on mass transfer at electrodes", *Electrochim. Acta* **24**, 693–699 (1979).
- [104] P. Boissonneau and P. Byrne, "An experimental investigation of bubble-induced free convection in a small electrochemical cell", *J. Appl. Electrochem.* **30**, 767–775 (2000).
- [105] H. Vogt, "On the gas-evolution efficiency of electrodes. II - Numerical analysis", *Electrochim. Acta* **56**, 2404–2410 (2011).
- [106] A. Taqieddin, R. Nazari, L. Rajic, and A. Alshwabkeh, "Review physicochemical hydrodynamics of gas bubbles in two phase electrochemical systems", *J. Electrochem. Soc.* **164**, E448–E459 (2017).
- [107] T. Iida, H. Matsushima, and Y. Fukunaka, "Water electrolysis under a magnetic field", *J. Electrochem. Soc.* **154**, E112 (2007).
- [108] J. A. Koza, S. Mühlenhoff, P. Żabiński, P. A. Nikrityuk, K. Eckert, M. Uhlemann, A. Gebert, T. Weier, L. Schultz, and S. Odenbach, "Hydrogen evolution under the influence of a magnetic field", *Electrochim. Acta* **56**, 2665–2675 (2011).
- [109] H. Matsushima, T. Iida, and Y. Fukunaka, "Gas bubble evolution on transparent electrode during water electrolysis in a magnetic field", *Electrochim. Acta* **100**, 261–264 (2013).

- [110] D. Baczymalski, F. Karnbach, X. Yang, G. Mutschke, M. Uhlemann, K. Eckert, and C. Cierpka, "On the electrolyte convection around a hydrogen bubble evolving at a microelectrode under the influence of a magnetic field", *J. Electrochem. Soc.* **163**, E248–E257 (2016).
- [111] D. Baczymalski, F. Karnbach, G. Mutschke, X. Yang, K. Eckert, M. Uhlemann, and C. Cierpka, "Growth and detachment of single hydrogen bubbles in a magnetohydrodynamic shear flow", *Phys. Rev. Fluids* **2**, 1–19 (2017).
- [112] N. Zuber, "Nucleate boiling. The region of isolated bubbles and the similarity with natural convection", *Int. J. Heat Mass Transf.* **6**, 53–78 (1963).
- [113] A. Iwasaki, H. Kaneko, Y. Abe, and M. Kamimoto, "Investigation of electrochemical hydrogen evolution under microgravity condition", *Electrochim. Acta* **43**, 509–514 (1997).
- [114] H. Matsushima, T. Nishida, Y. Konishi, Y. Fukunaka, Y. Ito, and K. Kuribayashi, "Water electrolysis under microgravity", *Electrochim. Acta* **48**, 4119–4125 (2003).
- [115] H. Matsushima, D. Kiuchi, Y. Fukunaka, and K. Kuribayashi, "Single bubble growth during water electrolysis under microgravity", *Electrochem. commun.* **11**, 1721–1723 (2009).
- [116] P. Mandin, Z. Derhoumi, H. Roustan, and W. Rolf, "Bubble over-potential during two-phase alkaline water electrolysis", *Electrochim. Acta* **128**, 248–258 (2014).
- [117] G. Sakuma, Y. Fukunaka, and H. Matsushima, "Nucleation and growth of electrolytic gas bubbles under microgravity", *Int. J. Hydrogen Energy* **39**, 7638–7645 (2014).
- [118] A. Bashkatov, X. Yang, G. Mutschke, B. Fritzsche, S. S. Hossain, and K. Eckert, "Dynamics of single hydrogen bubbles at Pt microelectrodes in microgravity.", *Phys. Chem. Chem. Phys.* **23**, 11818–11830 (2021).
- [119] N. Ibl, E. Adam, J. Venczel, and E. Schalch, *Chem. Ing. Technik* **403**, 202–215 (1971).
- [120] P. Yang, H. Guo, Z. Wang, and Q. Zhou, "Density and volumetric properties of binary mixtures of CO<sub>2</sub>+ hexadecane from (303.2 to 473.2) K and pressures up to 50.0 MPa", *J. Chem. Eng. Data* **64**, 2568–2577 (2019).

- [121] L. Janssen and J. Hoogland, "The effect of electrolytically evolved gas bubbles on the thickness of the diffusion layer", *Electrochim. Acta* **15**, 1013–1023 (1970).
- [122] L. Janssen, "Mass transfer at gas evolving electrodes", *Electrochim. Acta* **23**, 81–86 (1978).
- [123] S. W. Churchill and H. H. Chu, "Correlating equations for laminar and turbulent free convection from a vertical plate", *Int. J. Heat Mass Transf.* **18**, 1323–1329 (1975).
- [124] A. Wragg, "Free convection mass transfer at horizontal electrodes", *Electrochim. Acta* **13**, 2159–2165 (1968).
- [125] R. Hreiz, L. Abdelouahed, D. Fünfschilling, and F. Lopicque, "Electrogenerated bubbles induced convection in narrow vertical cells: A review", *Chem. Eng. Res. Des.* **100**, 268–281 (2015).
- [126] J. Schillings, O. Doche, and J. Deseure, "Modeling of electrochemically generated bubbly flow under buoyancy-driven and forced convection", *Int. J. Heat Mass Transf.* **85**, 292–299 (2015).
- [127] L. Abdelouahed, G. Valentin, S. Poncin, and F. Lopicque, "Current density distribution and gas volume fraction in the gap of lantern blade electrodes", *Chem. Eng. Res. Des.* **92**, 559–570 (2014).
- [128] L. Abdelouahed, R. Hreiz, S. Poncin, G. Valentin, and F. Lopicque, "Hydrodynamics of gas bubbles in the gap of lantern blade electrodes without forced flow of electrolyte: Experiments and CFD modelling", *Chem. Eng. Sci.* **111**, 255–265 (2014).
- [129] A. Zarghami, N. Deen, and A. Vreman, "CFD modeling of multiphase flow in an alkaline water electrolyzer", *Chem. Eng. Sci.* **227**, 115926 (2020).
- [130] K. Obata and F. F. Abdi, "Bubble-induced convection stabilizes the local pH during solar water splitting in neutral pH electrolytes", *Sustain. Energy Fuels* **5**, 3791–3801 (2021).
- [131] P. Mandin, J. Hamburger, S. Bessou, and G. Picard, "Modelling and calculation of the current density distribution evolution at vertical gas-evolving electrodes", *Electrochim. Acta* **51**, 1140–1156 (2005).

- [132] R. Hreiz, L. Abdelouahed, D. Fünfschilling, and F. Lopicque, “Electrogenerated bubbles induced convection in narrow vertical cells: PIV measurements and EulerLagrange CFD simulation”, *Chem. Eng. Sci.* **134**, 138–152 (2015).
- [133] A. Battistella, S. Aelen, I. Roghair, and M. van Sint Annaland, “EulerLagrange modeling of bubbles formation in supersaturated water”, *ChemEngineering* **2**, 39 (2018).
- [134] F. Higuera, “A model of the growth of hydrogen bubbles in the electrolysis of water”, *J. Fluid Mech.* **927**, A33 (2021).
- [135] F. J. Higuera, “Evolution of hydrogen bubbles at the surface of a porous horizontal cathode”, *Phys. Rev. Fluids* **7**, 113602 (2022).
- [136] Z. Zhang, W. Liu, and M. L. Free, “Phase-Field modeling and simulation of gas bubble Coalescence and detachment in a gas-liquid two-phase electrochemical system”, *J. Electrochem. Soc.* **167**, 013532 (2020).
- [137] K. Torii, M. Kodama, and S. Hirai, “Three-dimensional coupling numerical simulation of two-phase flow and electrochemical phenomena in alkaline water electrolysis”, *Int. J. Hydrogen Energy* **46**, 35088–35101 (2021).
- [138] A. Raman, P. Peñas, D. van der Meer, D. Lohse, H. Gardeniers, and D. Fernández Rivas, “Potential response of single successive constant-current-driven electrolytic hydrogen bubbles spatially separated from the electrode”, *Electrochim. Acta* **425**, 140691 (2022).
- [139] J. C. J. H. S. Carslaw, *Conduction of Heat in Solids*, 2 edition (Oxford University Press, USA) (1959).
- [140] J. Kim and P. Moin, “Application of a fractional-step method to incompressible Navier-Stokes equations”, *J. Comput. Phys.* **59**, 308–323 (1985).
- [141] R. Ostilla-Monico, Y. Yang, E. van der Poel, D. Lohse, and R. Verzicco, “A multiple-resolution strategy for Direct Numerical Simulation of scalar turbulence”, *J. Comput. Phys.* **301**, 308–321 (2015).
- [142] S. Schwarz, T. Kempe, and J. Fröhlich, “A temporal discretization scheme to compute the motion of light particles in viscous flows by an immersed boundary method”, *J. Comput. Phys.* **281**, 591–613 (2015).
- [143] I. Borazjani, L. Ge, and F. Sotiropoulos, “Curvilinear immersed boundary method for simulating fluid structure interaction with complex 3D rigid bodies”, *J. Comput. Phys.* **227**, 7587–7620 (2008).

- [144] U. Lcis, K. Taira, and S. Bagheri, "A stable fluidstructure-interaction solver for low-density rigid bodies using the immersed boundary projection method", *J. Comput. Phys.* **305**, 300–318 (2016).
- [145] M. P. Assen, J. B. Will, C. Ng, D. Lohse, R. Verzicco, and D. Krug, "Rising and settling 2D cylinders with centre of mass offset", In preparation. (2023).
- [146] M. Uhlmann, "An immersed boundary method with direct forcing for the simulation of particulate flows", *J. Comput. Phys.* **209**, 448–476 (2005).
- [147] T. Kempe and J. Fröhlich, "An improved immersed boundary method with direct forcing for the simulation of particle laden flows", *J. Comput. Phys.* **231**, 3663–3684 (2012).
- [148] W.-P. Breugem, "A second-order accurate immersed boundary method for fully resolved simulations of particle-laden flows", *J. Comput. Phys.* **231**, 4469–4498 (2012).
- [149] G. Lupo, M. Niazi Ardekani, L. Brandt, and C. Duwig, "An Immersed Boundary Method for flows with evaporating droplets", *Int. J. Heat Mass Transf.* **143**, 118563 (2019).
- [150] G. Lupo, A. Gruber, L. Brandt, and C. Duwig, "Direct numerical simulation of spray droplet evaporation in hot turbulent channel flow", *Int. J. Heat Mass Transf.* **160**, 120184 (2020).
- [151] Y. G. G.R. Liu, *An introduction to meshfree methods and their programming*, 1 edition (Springer) (2005).
- [152] M. Vanella and E. Balaras, "A moving-least-squares reconstruction for embedded-boundary formulations", *J. Comput. Phys.* **228**, 6617–6628 (2009).
- [153] J. Lu, S. Das, E. Peters, and J. Kuipers, "Direct numerical simulation of fluid flow and mass transfer in dense fluid-particle systems with surface reactions", *Chem. Eng. Sci.* **176**, 1–18 (2018).
- [154] H. Vogt, "The rate of gas evolution of electrodesI. An estimate of the efficiency of gas evolution from the supersaturation of electrolyte adjacent to a gas-evolving electrode", *Electrochim. Acta* **29**, 167–173 (1984).
- [155] H. Vogt, "The rate of gas evolution at electrodesII. An estimate of the efficiency of gas evolution on the basis of bubble growth data", *Electrochim. Acta* **29**, 175–180 (1984).

- [156] P. S. Epstein and M. S. Plesset, "On the Stability of Gas Bubbles in Liquid Gas Solutions", *J. Chem. Phys.* **18**, 1505–1509 (1950).
- [157] L. Scriven, "On the dynamics of phase growth", *Chem. Eng. Sci.* **10**, 1–13 (1959).
- [158] H. Vogt, "On the various types of uncontrolled potential increase in electrochemical reactors The anode effect", *Electrochim. Acta* **87**, 611–618 (2013).
- [159] H. Vogt, "The quantities affecting the bubble coverage of gas-evolving electrodes", *Electrochim. Acta* **235**, 495–499 (2017).
- [160] G. M. Whitney and C. W. Tobias, "Mass-transfer effects of bubble streams rising near vertical electrodes", *AIChE J.* **34**, 1981–1995 (1988).
- [161] H. Vogt, "Mechanisms of mass transfer of dissolved gas from a gas-evolving electrode and their effect on mass transfer coefficient and concentration overpotential", *J. Appl. Electrochem.* **19**, 713–719 (1989).
- [162] H. Vogt, "The actual current density of gas-evolving electrodes Notes on the bubble coverage", *Electrochim. Acta* **78**, 183–187 (2012).
- [163] D. E. Westerheide and J. W. Westwater, "Isothermal growth of hydrogen bubbles during electrolysis", *AIChE J.* **7**, 357–362 (1961).
- [164] J. Glas and J. Westwater, "Measurements of the growth of electrolytic bubbles", *Int. J. Heat Mass Transf.* **7**, 1427–1443 (1964).
- [165] N. P. Brandon and G. H. Kelsall, "Growth kinetics of bubbles electrogenerated at microelectrodes", *J. Appl. Electrochem.* **15**, 475–484 (1985).
- [166] A. Bashkatov, S. S. Hossain, G. Mutschke, X. Yang, H. Rox, I. M. Weidinger, and K. Eckert, "On the growth regimes of hydrogen bubbles at microelectrodes", *Phys. Chem. Chem. Phys.* **24**, 26738–26752 (2022).
- [167] R. Darby and M. Haque, "The dynamics of electrolytic hydrogen bubble evolution", *Chem. Eng. Sci.* **28**, 1129–1138 (1973).
- [168] H. Verhaart, R. de Jonge, and S. van Stralen, "Growth rate of a gas bubble during electrolysis in supersaturated liquid", *Int. J. Heat Mass Transf.* **23**, 293–299 (1980).
- [169] F. Sepahi, N. Pande, K. L. Chong, G. Mul, R. Verzicco, D. Lohse, B. T. Mei, and D. Krug, "The effect of buoyancy driven convection on the growth and dissolution of bubbles on electrodes", *Electrochim. Acta* **403**, 139616 (2022).

- [170] S. S. Hossain, A. Bashkatov, X. Yang, G. Mutschke, and K. Eckert, "Force balance of hydrogen bubbles growing and oscillating on a microelectrode", *Phys. Rev. E* **106**, 035105 (2022).
- [171] A. Bashkatov, A. Babich, S. Hossain, X. Yang, G. Mutschke, and K. Eckert, "H<sub>2</sub> bubble motion reversals during water electrolysis", *J. Fluid Mech.* **958**, A43 (2023).
- [172] S. Park, L. Liu, C. Demirkir, O. van der Heijden, D. Lohse, D. Krug, , and M. T. M. Koper, "Solutal marangoni effect determines bubble dynamics during electrocatalytic hydrogen evolution", In review (2023).
- [173] Y. Cao, C. Soares, N. Padoin, and T. Noël, "Gas bubbles have controversial effects on Taylor flow electrochemistry", *Chem. Eng. J.* **406**, 126811 (2021).
- [174] I. Bagemihl, C. Bhatraju, J. R. Van Ommen, and V. Van Steijn, "Electrochemical reduction of CO<sub>2</sub> in tubular flow cells under gas-liquid taylor flow", *ACS Sustain. Chem. Eng.* **10**, 12580–12587 (2022).
- [175] M. Abolhasani, A. Günther, and E. Kumacheva, "Microfluidic studies of carbon dioxide", *Angew. Chem. Int. Edit.* **53**, 7992–8002 (2014).
- [176] H. Hassanzadeh, M. Pooladi-Darvish, and D. W. Keith, "Scaling behavior of convective mixing, with application to geological storage of CO<sub>2</sub>", *AIChE journal* **53**, 1121–1131 (2007).
- [177] H. Emami-Meybodi, H. Hassanzadeh, C. P. Green, and J. Ennis-King, "Convective dissolution of CO<sub>2</sub> in saline aquifers: Progress in modeling and experiments", *Int. J. Greenh. Gas Control* **40**, 238–266 (2015).
- [178] M. De Paoli, "Influence of reservoir properties on the dynamics of a migrating current of carbon dioxide", *Phys. Fluids* **33**, 016602 (2021).
- [179] M. C. Rogers and S. W. Morris, "Buoyant plumes and vortex rings in an autocatalytic chemical reaction", *Phys. Rev. Lett.* **95**, 024505 (2005).
- [180] V. Loodts, H. Saghrou, B. Knaepen, L. Rongy, and A. De Wit, "Differential diffusivity effects in reactive convective dissolution", *Fluids* **3**, 83 (2018).
- [181] Y. Gu, V. Hegde, and K. J. Bishop, "Measurement and mitigation of free convection in microfluidic gradient generators", *Lab Chip* **18**, 3371–3378 (2018).

- [182] E. Dietrich, S. Wildeman, C. W. Visser, K. Hofhuis, E. S. Kooij, H. J. W. Zandvliet, and D. Lohse, "Role of natural convection in the dissolution of sessile droplets", *J. Fluid Mech.* **794**, 45–67 (2016).
- [183] Á. Moreno Soto, O. R. Enríquez, A. Prosperetti, D. Lohse, and D. van der Meer, "Transition to convection in single bubble diffusive growth", *J. Fluid Mech.* **871**, 332–349 (2019).
- [184] F. Du, H. Ma, and Y. Gu, "Three different periods of CO<sub>2</sub> dissolution into a light crude oil", *Can. J. Chem. Eng.* **97**, 330–343 (2019).
- [185] H. Karimaie and E. Lindeberg, "Experimental verification of CO<sub>2</sub> dissolution rate due to diffusion induced convection", *Energy Procedia* **114**, 4917–4925 (2017).
- [186] R. Farajzadeh, P. L. Zitha, and J. Bruining, "Enhanced mass transfer of CO<sub>2</sub> into water: experiment and modeling", *Ind. Eng. Chem. Res.* **48**, 6423–6431 (2009).
- [187] R. Zhao, M. Xu, J. Yang, J. Y. Fu, M. Heng, and X.-a. Yue, "Non-constant diffusion behavior for CO<sub>2</sub> diffusion into brine: Influence of density-driven convection", *J. Solution Chem.* **47**, 1926–1941 (2018).
- [188] M. J. Doughty, "ph dependent spectral properties of sodium fluorescein ophthalmic solutions revisited", *Ophthalmic and Physiological Optics* **30**, 167–174 (2010).
- [189] T. A. Robertson, F. Bunel, and M. S. Roberts, "Fluorescein derivatives in intravital fluorescence imaging", *Cells* **2**, 591–606 (2013).
- [190] S. Yewalkar, T. Wu, D. Kuan, H. Wang, D. Li, A. Johnson, D. Posarac, S. Duff, and X. T. Bi, "Applicability of differential fluorescein diacetate and propidium iodide fluorescence staining for monitoring algal growth and viability", *Waste Dispos. Sustain. Energy* **1**, 199–206 (2019).
- [191] O. R. Enríquez, C. Hummelink, G.-W. Bruggert, D. Lohse, A. Prosperetti, D. van der Meer, and C. Sun, "Growing bubbles in a slightly supersaturated liquid solution", *Rev. Sci. Instrum.* **84**, 065111 (2013).
- [192] B.-S. Chun and G. T. Wilkinson, "Interfacial tension in high-pressure carbon dioxide mixtures", *Industrial & engineering chemistry research* **34**, 4371–4377 (1995).

- [193] R. Sander, "Compilation of Henry's law constants (version 4.0) for water as solvent", *Atmos. Chem. Phys.* **15**, 4399–4981 (2015).
- [194] A. Tamimi, E. B. Rinker, and O. C. Sandall, "Diffusion coefficients for hydrogen sulfide, carbon dioxide, and nitrous oxide in water over the temperature range 293–368 K", *J. Chem. Eng. Data* **39**, 330–332 (1994).
- [195] G. Ahlers, E. Bodenschatz, R. Hartmann, X. He, D. Lohse, P. Reiter, R. J. Stevens, R. Verzicco, M. Wedi, S. Weiss, *et al.*, "Aspect ratio dependence of heat transfer in a cylindrical rayleigh-bénard cell", *Phys. Rev. Lett.* **128**, 084501 (2022).
- [196] N. Pande, S. K. Chandrasekar, D. Lohse, G. Mul, J. A. Wood, B. T. Mei, and D. Krug, "Electrochemically induced pH change: Time-resolved confocal fluorescence microscopy measurements and comparison with numerical model", *J. Phys. Chem. Lett.* **11**, 7042–7048 (2020), PMID: 32787336.
- [197] K.-K. Tan and R. B. Thorpe, "The onset of convection induced by buoyancy during gas diffusion in deep fluids", *Chem. Eng. Sci.* **54**, 4179–4187 (1999).
- [198] E. A. Fadlun, R. Verzicco, P. Orlandi, and J. Mohd-Yusof, "Combined immersed-boundary finite-difference methods for three-dimensional complex flow simulations", *J. Comput. Phys.* **161**, 35–60 (2000).
- [199] R. Hartmann, R. Verzicco, L. Klein Kranenbarg, D. Lohse, and R. J. Stevens, "Multiple heat transport maxima in confined-rotating Rayleigh-Bénard convection", *J. Fluid Mech.* **939**, A1 (2022).
- [200] M. Holzner and B. Lüthi, "Laminar superlayer at the turbulence boundary", *Phys. Rev. Lett.* **106**, 134503 (2011).
- [201] M. Wolf, B. Lüthi, M. Holzner, D. Krug, W. Kinzelbach, and A. Tsinober, "Investigations on the local entrainment velocity in a turbulent jet", *Phys. Fluids* **24**, 105110 (2012).
- [202] C. Dopazo, J. Martín, and J. Hierro, "Iso-scalar surfaces, mixing and reaction in turbulent flows", *Comptes Rendus - Mec.* **334**, 483–492 (2006).
- [203] N. Chakraborty and R. S. Cant, "A priori analysis of the curvature and propagation terms of the flame surface density transport equation for large eddy simulation", *Phys. Fluids* **19**, 105101 (2007).

- 
- [204] D. Krug, M. Holzner, B. Lüthi, M. Wolf, W. Kinzelbach, and A. Tsinober, “The turbulent/non-turbulent interface in an inclined dense gravity current”, *J. Fluid Mech.* **765**, 303–324 (2015).
- [205] M. van Reeuwijk and M. Holzner, “The turbulence boundary of a temporal jet”, *J. Fluid Mech.* **739**, 254–275 (2014).
- [206] O. Shishkina, “Rayleigh-Bénard convection: The container shape matters”, *Phys. Rev. Fluids* **6**, 090502 (2021).



# Summary

**B**ubbles in electrolysis exhibit significant complexities that greatly affect mass transport at gas-evolving electrodes. They directly impact different mass transfer mechanisms including diffusion, convection and migration. This renders disentangling the relevant effects through experiments an extremely tedious, if not impossible, task. Therefore, we take advantage of highly-accurate three-dimensional numerical simulations to unravel the controlling mechanisms of mass transfer at gas-evolving electrodes. We simplify the system to a certain extent such that the influence of undesirable parameters is suppressed and yet the main effects are outstandingly revealed.

In particular, we combine the in-situ experiments with numerical simulations to study the effect of single-phase convection on the growth and dissolution dynamics of bubbles adhering to the electrode in chapter 1. Such flows originate from density gradients in the solution mixture caused by concentration variations in the electrode boundary layer. Untangling the effect of diffusion and natural convection, we observe that the experimentally measured bubble evolution can only be accurately described once the flow induced by buoyancy forces is taken into account in addition to the diffusive transport. Furthermore, we study the transition time to the convection in the course of ongoing reaction on the electrode surface and observe that bubbles promote the instabilities in the system before overkilling it in a tightly-spaced configuration of the bubbles. Such effects are carefully examined and a criterion for transition to convection is established. We also investigate the bubble clustering in a regular network on the electrode surface and succeed to accurately reproduce the experimental measurements after adjusting for the inter-spacing of the bubbles in the cluster in accordance with the experiments.

Single-phase convection can only be the rate-controlling mechanism at low values of current density where the fractional bubble coverage of the electrode is not so high and bubble growth is very slow. This allows the density gradients in the electrode boundary layer to develop to a sufficient extent necessary for triggering

the instabilities. However at high values of current density a strong flow is established in the solution as a result of microconvection induced by bubble growth as well as two-phase buoyancy-driven convection owing to the density variations of gas-in-liquid dispersion. Such flows relax the density gradients in the liquid phase close to the electrode by enhancing the mixing in the electrolyte solution and, therefore, suppress the single-phase convection. In case that all mechanism can coexist, the strong flow caused by bubble rise in the electrolyte will most likely prevail the single-phase natural convection.

Hence, in chapter 2, we solely investigate bubble-induced convection by bubble growth and ascent in the cathodic part of a water electrolyzer. We establish a unique expression for hydrogen transport at the electrode by defining an effective Grashof number,  $Gr$ , which accounts for buoyancy forces of gas-in-liquid dispersion. The expression is analogous to those developed for single-phase buoyancy-driven convection in heat and mass transfer problems highlighting the analogy between these systems. Additionally compensating for surface blockage effects of bubbles, same expression can quantify the electrolyte transport from the electrode. These findings corroborate the predominance of two-phase buoyancy-driven convection over other mass transfer mechanisms including microconvection caused by bubble growth, which is known as the prevailing mechanism in the literature. Next, we quantify the mass transfer to the bubble by taking into account the driving force of the bubble growth incorporated in an effective Jakob number,  $Ja$ . Finally an expression based on input parameters for gas-evolution efficiency (the fraction of total gas desorbed into the bubbles) is established which is key in determining the bubbles evolution and hence the following mass transfer processes in such systems.

Finally, in chapter 3 we look into the downward dissolution dynamics of  $\text{CO}_2$  in a cylindrical water barrier employing experiments and simulations. We see that although the penetration rate of the  $\text{CO}_2$  front is enhanced after the transition to convection, it still follows the dynamics of diffusion regime with a higher effective diffusivity. Performing an analysis on transient local fluxes across the front iso-surface, it is revealed that convection causes front convolutions and steepens the gradients nearby. As a result the diffusive flux across the interface intensifies leading to faster propagation of the front. Yet the propagation dynamics concerning the diffusion regime, i.e.  $z \propto t^{1/2}$ , maintains. Our findings offer broader insight into the stable dissolution dynamics of  $\text{CO}_2$  which is of crucial importance in devising carbon capture and storage technologies.

# Samenvatting

**B**ellen in elektrolyse zijn van aanzienlijke complexiteit, zodanig dat ze de massatransport bij gas-evoluerende elektroden enorm beïnvloeden. Ze hebben rechtstreeks invloed op verschillende massatransportmechanismen, waaronder diffusie, convectie en migratie. Dit maakt het ontrafelen van de relevante effecten door middel van experimenten een uiterst tijdrovende, zo niet onmogelijke taak. Daarom maken we gebruik van zeer nauwkeurige driedimensionale numerieke simulaties om de mechanismen die de massatransport bij gas-evoluerende elektroden beheersen te onthullen. We vereenvoudigen het systeem tot op zekere hoogte zodat de invloed van ongewenste parameters wordt onderdrukt en de belangrijkste effecten duidelijk naar voren komen.

In het bijzonder combineren we in-situ experimenten met numerieke simulaties om het effect van enkelfasige convectie op de groei- en oplossingsdynamiek van bellen die zich hechten aan de elektrode te bestuderen in hoofdstuk 1. Dergelijke stromingen ontstaan door dichtheidsgradiënten in de mengoplossing veroorzaakt door concentratievariaties in de grenslaag van de elektrode. Door het effect van diffusie en natuurlijke convectie te ontwarren, observeren we dat de experimenteel gemeten evolutie van de bellen alleen nauwkeurig kan worden beschreven wanneer de stroming veroorzaakt door drijfkrachten in rekening wordt gebracht samen met de diffusieve transport. Bovendien bestuderen we de overgangstijd naar convectie tijdens de voortgaande reactie op het elektrodeoppervlak en observeren we dat bellen de instabiliteiten in het systeem bevorderen voordat ze het systeem overbelasten in een dicht opeengepakte configuratie van de bellen. Dergelijke effecten worden zorgvuldig onderzocht en er wordt een criterium voor de overgang naar convectie vastgesteld. We onderzoeken ook de clustering van bellen in een regelmatig netwerk op het elektrodeoppervlak en slagen erin om de experimentele metingen nauwkeurig te reproduceren na aanpassing van de onderlinge afstand tussen de bellen in de cluster in overeenstemming met de experimenten.

Enkelfasige convectie overheerst bij lage stroomdichtheid, waarbij de bellenbe-

dekking van de elektrode laag is en de groei van bellen traag verloopt. Bij hoge stroomdichtheid ontstaat er een sterke stroming door microconvectie door bellen-groei en tweefasige convectie gedreven door dichtheidsvariatiën van gas-in-vloeistof dispersie. De stromingen verminderen de dichtheidsgradiënten dichtbij de elektrode en onderdrukken enkelfasige convectie. Sterke stroming door bel-opstijging zal waarschijnlijk de enkelfasige convectie overheersen als alle mechanismen samenkomen.

Daarom onderzoeken we in hoofdstuk 2 uitsluitend de door bellen veroorzaakte convectie door groei en stijging van bellen in het kathodische deel van een water elektrolyseapparaat. We stellen een unieke uitdrukking op voor waterstoftransport aan de elektrode door een effectief Grashof-getal,  $Gr$ , te definiëren, dat rekening houdt met de drijfkrachten van gas-in-vloeistof dispersie. De uitdrukking is analoog aan die ontwikkeld voor enkelfasige opwaartse convectie gedreven door dichtheidsvariatiën in warmte- en massatransportproblemen, waarbij de analogie tussen deze systemen wordt benadrukt. Door ook compensatie toe te passen voor oppervlakteblokkerings-effecten van bellen, kan dezelfde uitdrukking het elektrolyttransport vanaf de elektrode kwantificeren. Deze bevindingen bevestigen de overheersing van tweefasige opwaartse convectie gedreven door dichtheidsvariatiën van gas-in-vloeistof dispersie boven andere massatransportmechanismen, inclusief microconvectie veroorzaakt door de groei van bellen, wat bekend staat als het overheersende mechanisme in de literatuur. Vervolgens kwantificeren we het massatransport naar de bel door rekening te houden met de drijvende kracht van de belgroei, opgenomen in een effectief Jakob-getal,  $Ja$ . Tot slot wordt een uitdrukking op basis van invoerparameters voor de efficiëntie van gasvorming (de fractie van totaal gas dat in de bellen wordt drijfkrachten) vastgesteld, wat essentieel is voor het bepalen van de evolutie van de bellen en daarmee de daaropvolgende massatransportprocessen in dergelijke systemen.

In hoofdstuk 3 onderzoeken we de neerwaartse oplossingsdynamiek van  $\text{CO}_2$  in een cilindrische waterbarrière aan de hand van experimenten en simulaties. We constateren dat hoewel de penetratiesnelheid het de  $\text{CO}_2$ -front wordt versterkt na de overgang naar convectie, het nog steeds de dynamiek van het diffusieregime volgt, zij het met een hogere effectieve diffusiviteit. Door een analyse uit te voeren van de tijdsafhankelijke lokale fluxen over het front-iso-oppervlak, wordt onthuld dat convectie leidt tot frontconvoluties en steilere gradiënten in de nabije omgeving. Als gevolg daarvan neemt de diffusieve flux over het raakvlak toe, wat leidt tot een snellere verspreiding van het front. Toch blijft de voortplantingsdynamiek met betrekking tot het diffusieregime, d.w.z.  $z \propto t^{1/2}$ , behouden. Onze bevindingen bieden breder inzicht in de stabiele oplossingsdynamiek van  $\text{CO}_2$ , wat van cruciaal belang is bij het ontwikkelen van technologieën voor koolstofafvang en -opslag.

# Acknowledgments

It wasn't easy; in fact, it was much more difficult than I had anticipated. If I knew the extent of the challenges involved in pursuing a Ph.D., I'm not sure if I would ever have the courage to start. The journey is filled with countless stressful days, hard work, sleepless nights, and months without a single day off. Being far away from your homeland and family adds to the difficulties. However, in the end, it all pays off with a tremendous achievement - perhaps the greatest one a person can ever achieve in their lifetime: earning a Ph.D. It washes away all the bitterness of the hardships and leaves behind only sweetness and unforgettable memories that will be cherished for a lifetime. I am certain that one day I will deeply miss my time at PoF. But along with that longing, I will also feel immense joy as I recall the good days at PoF. I will be grateful that I landed in the Netherlands, where my life took a turn, and where I had the privilege of meeting so many remarkable people who made this challenging journey much more bearable and made me feel at home. Therefore, I would like to express my gratitude to as many of these people as possible, to thank them, even if it's just a small gesture, for the incredible experiences they created for me at PoF.

Dear **Detlef**, I am really struggling to find the proper words which can express my feelings in how grateful I am to you. You entirely changed my life by trusting in me and giving me this chance to start my PhD here. In the days that I was totally desperate to get my visa to join **Rodolfo's** group in US, you invited me for an interview. The Skype interview got serious faster than I expected and you immediately asked me how the boundary layer thickness of a laminar flow over a horizontal book, that you had in front of the camera, would scale with  $Re$ . I was so nervous and answered 0.5 instead of  $-0.5$ , but you trusted me in the end and decided to offer me this position. Although it was not going so great initially, I am happy that the things turned around ultimately and you found me qualified to defend my PhD. Finalizing my PhD was the only thing that I could do in return of a tiny bit of the favor you did to me. I hope you accept this as a sincere 'thank you'.

Dear **Roberto**, I remember our interview very clearly as you were in a beach talking with me on Skype. You asked me some nice questions about the  $k - \epsilon$  turbulence model that I had used in my master thesis, but that was much less stressful than my interview with Detlef. Doing this PhD was not possible without your help and thoughtful ideas. Whenever I had a numerical issue you were always to the point dragging out the main issue that I had to overcome. Our weekly group meetings were really joyous moments as you always were keeping the balance of scientific and non-scientific stuff. I will also never forget the epic moment you joined the group meeting while driving and in the meantime I also tried to show some slides to you. You are one of the kindest and most knowledgeable person I have ever met in my life and thank you very much for all the times you discussed with me and helped me finish my thesis.

Now I come to the part that I've been waiting for for a long time. I have always been thinking to find the most proper word to describe you, but unfortunately I could not find a better phrase than what *Martin Assen* used for you; you are the real 'tough guy'. Now you know that I am talking about you **Dominik**. You are literally tough in all aspects. From handling your work and personal life challenges simultaneously to your extreme dedication to work and science. We are always amazed and inspired by you, that how you can be a great father and in the meantime a great scientist with many PhD students and postdocs, and yet never satisfied with the achievements in your career. The passion that you have in doing the high-quality research is really unique and this together with your very high IQ make you a very successful researcher. While you are probably one of the coolest supervisors and all of your students can really have fun working with you, you are also one of the most strict, impatient and sometimes intimidating supervisors that has ever lived. All of these features are always a thrust for your students and I also have to confess that without you it was certainly impossible to finish this PhD. You became my savior in my second year and I could only bring the things to fruition by having your strong support and help. Thanks for tolerating me in all the long-lasting never-ending discussions, for calling me in the late nights to have informal discussions, for reading and rewriting my papers very carefully at late nights when your kids were asleep, and upgrading them to another level. I was so lucky to have you as my supervisor (although not officially until last month) and will never forget the sweet memories of working with you. I wish you good luck for the rest of your career and I am sure you will be the future 'Detlef'.

### *My paronyms*

**Çayan**, my Turkish Kurdish comrade. You made my life at PoF way more fun by adding some middle-eastern spice to the atmosphere. However, I was getting in-

creasingly jealous for your long hair while I was losing mine. Thanks for pushing me so hard to get a hair transplant in Turkey and showing me many head samples of your friends and family. Keep pushing me please, I might change my opinion one day. It was a great fun sharing many common words in Turkish, Kurdish and Persian and teaching you the origin of many words. I have learned a few Turkish words from you but not satisfied at all since it is a pity that our language is so close but we still have to communicate in English. I am so eager to learn much more until I can properly talk with you. Thank you for all the fun time you brought to me through conversations about politics, culture, sports and many lunch/coffee time gossips. We have a huge disagreement in our political view which made our discussion always intense. I am sure you will realize one day that I've been always true (kidding). You still have more than a year left in your PhD, and I wish all the best for you and your cute bubbles, and also in battling with *Dominik*.

**Aleksandr** 🐱 my Russian friend. Although you joined PoF when I was in the final stages of my PhD, still we shared many great moments together. You changed the vibe of ME114C entirely and added joy and cat style to it. I will always keep 'Brujka' sticker and also the mousepad you gifted to me although I wasn't sure initially that I would use it. Thank you for all the 'Hello Fresh' dishes from which I learned many new recipes. You made me laugh every morning by entering the office with so many foods and sharing a chocolate croissant with me. You probably also hold a Guinness world record for the fastest mouse scroll. I am kidding, but I am always impressed by how efficient and fast you work, and this has already brought you many success. Thanks for showing me your experimental set-up and teaching me a few tricky experimental techniques such as how to force a bubble to detach from the electrode, e.g. by kicking the desk. Keep going *Aleks*, I am sure you will be a decent professor one day and you truly deserve it.

### *AFiD group*

Doing all the numerical simulations were made possible by working and interacting with brilliant minds in AFiD numerical group. First of all I would like to thank **Steven Chong** for tutoring me with the code when I started my PhD and helped me get started with my research by supervising me. **Richard** thanks for your help in initial stage of my PhD although I did not find the opportunity to collaborate further with you. **CS** whose advanced developments in the code made the work for other people much easier. **Martin Assen** thank you for picking me as your paranymp and all of your help debug my code and explaining the most in-detailed information in every single routine. Your customized VIM color scheme was fantastic and I still use it. **Vanshu**, you were also my neighbor and I enjoyed a lot playing table tennis

with you in our apartment although I was losing most of the times. We shared a lot of fun times by talking about general stuff and also code issues and numerical details. I wish you good luck for the rest of your PhD. **Giulia** thanks for saving my data from Irene when they revoked my access to the system. I am always amazed by how you deal with your extremely ugly particles in turbulence, so I wish you good luck handling them. **Chris** thank you for always being there and find a solution for the code with different compilers on the HPCs, and also for helping people with your practical knowledge in python, latex, etc. **Rui** and **Naoki**, your effort in writing the grant proposals together with *Chris, Robert* and *Giulia* is always appreciated, without which finishing this thesis was not possible. I also would like to express my gratitude to former AFiD members, **Pieter, Alex, Qi, Hao-ran**, with whom I shared great moments.

### *ME114C*

**Robert** my officemate, colleague and friend. I probably shared the most time of my PoF era with you seating and working in the office and discussing wide-ranging topics in our free time, particularly about football. I was always so impressed about how much passion you had with your hometown team, Hanover 96. We could see Hanover 96 logo all over the place in your office and home. You are a true example of a loyal team supporter and I hope they can make it to the Bundesliga soon and we never see you sad again when someone asking about it. I would like to also thank you for all the CPU time managements you did for the group. You were also a great PoF united captain and I hope you can leave it in good hands once you leave PoF soon. **Martin Essink**, thank you for your patience to tolerate my slow dutch and practicing it nicely with me. We also shared a lot of cultural information and also technical stuff including python, linux, etc. Your PhD defence was also one of the best I attended during my PhD and I hope I have learned enough from it to handle mine properly. **Aleksandr** I have already talked so much about you, then what are you looking for here?

### *Neighbor offices*

**Yibo**, you are the coolest Chinese guy I've ever met. I've always enjoyed chatting with you in the office about politics and economics in our homeland and we shared a lot together. You definitely kept the vibe of our office higher by knocking our door randomly, coming in and chatting about different things. Working with you was also a great pleasure and I thank you for helping me simulate the Marangoni flows around the bubbles. You are my only Chinese friend who will stay in Netherlands and we probably can still see each other in future. **Yoan**, the funniest memory that I have with you is our Bata2022 race together in the midnight session. You were supposed to cycle with me, but you lost me and I was left alone in absolute

---

darkness in the middle of nowhere. When I was about to give up you found me again in the last kilometers and luckily I didn't get lost there. We defend in the same day and I hope it turns out well in the end for both of us. Thank you for guiding me in the job searching process lately. You already have found a job at ASML and I hope you best of luck for your future career. **Saeed** it was fun spending time with you during the conferences and arguing about the religious stuff that we had many disagreements, and thanks **Nathan** for occasionally practicing dutch with me.

**Daniel**, it was very nice to have you as a friend and also as a colleague. Whenever the science at PoF was running out of fuel, you were keeping it alive by organizing the good drinking Fridays with *Robert* and *Pim W.*, bringing the tired people together and force them to drink. I was always amazed by your experimental tricks of adding ethanol, methanol, salt and pepper to your CO<sub>2</sub> rich barrier to tame that green plume. However you were underestimating the importance of that 1 degree tilt in your setup which took me 6 months to realize what was going on in your experiments. Good luck with your new high pressure chamber and I hope you don't blow up that lab. **Pim W.**, thanks for supplying the drug (coffee) to the scientists at PoF and not letting them get exhausted. You were also very kind by editing my samenvatting when Daniel refused to do it. Good luck with your turbulent bubbly flow in the rest of your PhD.

**Bernardo**, it was so unfair playing basketball with you. Maybe I should have tried to play much dirtier to defend you, but it probably wouldn't matter as you were so tough and tall enough to reach the hoop easily. Thank you for bringing us together at your place for delicious tacos and barbecues and more importantly teaching me how to properly drink tequila. You also have the coolest mom and dad and I am looking forward to meeting them again. Good luck with finishing up your research.

**Jessica**, you are a great friend and definitely one of those people who made my life in Netherlands more fun. Every year I enjoyed so much at your parties for Oktoberfest and Halloween and I hope you still keep doing it even if you move out of Enschede. Thanks for practically teaching me how to make a cheesecake, and that time probably was the first and last time I made a cake. I hope you stay in Netherlands longer so we still can have fun and I can probably make you terrible cheesecake.

**Vatsal** I am always inspired by your passion for science and the dedication you have for your work. Soon you will be a well-known scientist. I always enjoyed discussing with you and it was my great pleasure to meet you at PoF. **Marco**, thanks for trying to push the boundaries of my tennis skills. I learned a lot from you during

the couple of times we played together, but could never beat you as my tennis knowledge is not fundamental as yours. **Utkarsh**, we indeed started playing and learning tennis together by trying different rackets. I enjoyed competing with you in the countless hours that we played, and looking forward to doing it again.

#### *Krug crew*

First, I would like to thank the TA'ing squad of heat and mass transfer, **Lijun, Simon, Minkush, Duco** and **Çayan** without whom managing that course and satisfying *Dominik* for exam questions were not possible. **Timothy**, thanks for being a very nice roommate during the EFMC conference at Greece, and also offering us a ride whenever we were going around in Netherlands, good luck with the rest of you time in PoF.

#### *Persian PoF members*

**Ali, Hadi** and **Ashkan**, thank you guys for keeping the Persian culture alive at PoF. I had so much fun discussing with you about different stuff, particularly political situation in Iran. I also consider it as a failure that we could not bring *Ali* to the right path and cure his destructive political view. *Ali*, I wish you all the best especially for your Youtube channel and I really hope you don't hurt yourself with your motorbike.

#### *PoF United*

I would like to thank the PoF United players who kept the competition spirit at the highest level and playing with them was so much fun; **Alexander Blass., Pieter, Robert, Youssef, Çayan, Alex O., Jens, Jochem, Vincent, Bernardo, Pim W., Anja, Maaïke, Davide, Ahmed** and ... . I hope you bring more championships to PoF.

#### *Outside PoF*

I owe big to my old friends, who were always beside me and never let me alone in the old days before I move to Netherlands and also during my PhD, with whom I share countless sweet memories and I am really looking forward to meeting them soon again; **Behrooz, Essi, Rahim, Farzad, Mamali, Meisam, Hossein, Reza, Hamid, Mehdi** and **Bahamin** thank you guys for all the great times we had together.

And my foremost gratitude goes to my family who always supported me, loved me and had faith on me on what I could achieve. I wouldn't be at this point in my life without your continuous dedication, sacrifice and encouragement. I love you so much and the only thing that I wish in my life is a reunion with you. I hope the situation turns around one day so that we can live near each other again.

Farzan Sepahi

July, 2023

# About the author

*Farzan Sepahi* was born on May 16<sup>th</sup>, 1990 in *Fasa*, a small town located in southeast of *Shiraz, Iran*. During his studies in school he showed a great passion to physics and mathematics and he obtained his high school diploma in this field in 2008. The same year, he participated in the nationwide entrance exam for public universities in *Iran* and he was admitted to *Shiraz University* for a B.Sc. program in Mechanical Engineering. He obtained his B.Sc. in 2013 and the same year he participated in the national exam for master's program in which he ranked 27<sup>th</sup> out of more than twenty thousand participants.



Therefore, he was admitted to *Sharif University of Technology*, the most prestigious technical university in *Iran*, to pursue a M.Sc. in Fluid Mechanics. During his master's studies he developed a finite volume solver to solve the Reynolds-Averaged-Navier-Stokes and heat equations using which he modelled wall-bounded turbulent natural convection with interior objects. After obtaining his M.Sc. degree in 2016, he prepared and participated in the entrance exam for doctorate program and he was admitted to the same department at *Sharif University of Technology* in 2017 to pursue a Ph.D. in Fluid Mechanics. However, given the hard political and economic conditions in *Iran*, he discontinued his Ph.D. studies there and moved all the way to the Netherlands to pursue his dreams in *Physics of Fluids* group at the *University of Twente* in 2019. During his Ph.D. journey he mostly studied mass transport and electrohydrodynamics at gas-evolving electrodes using high-fidelity numerical simulations. His research efforts culminated in the publication of this thesis and the attainment of a valuable Ph.D. degree.

